

Transition Metal Oxide Based Nanocomposites for High Performance Electrochemical Supercapacitor Applications



Doctor of Philosophy
In
Physical Chemistry
By
Muhammad Nasir Hussain

Department of Chemistry,
Quaid-i-Azam University
Islamabad, Pakistan

2024

Transition Metal Oxide Based Nanocomposites for High Performance Electrochemical Supercapacitor Applications



A dissertation submitted to the Department of Chemistry, Quaid-i-Azam University, Islamabad, in partial fulfilments of the requirements for the

degree of

Doctor of Philosophy

in

Physical Chemistry

By

Muhammad Nasir Hussain

Department of Chemistry,

Quaid-i-Azam University

Islamabad 45320, Pakistan.

2024



In The Name Of Allah the Most Merciful the Most Beneficent

**“Whoever travels a path in search of knowledge,
Allah will make easy for him a path to paradise.”**

Prophet Muhammad (PCBUH)

Source: Sahih Muslim 2699

DECLARATION

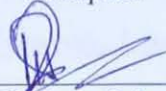
This is to certify that this dissertation entitled "*Transition Metal Oxide Based Nanocomposites for High Performance Electrochemical Supercapacitor Applications*" submitted by *Mr. M. Nasir Hussain*, is accepted in its present form by the Department of Chemistry, Quaid-i-Azam University, Islamabad, Pakistan, as satisfying the partial requirement for the award of degree of *Doctor of Philosophy in Physical Chemistry*.

External Examiner (I):



Dr. Riaz Ahmed Ch.
House # 1298, Road H,
Phase-III, Bahria Town,
Rawalpindi

External Examiner (II):



Dr. Hafiz-ur-Rehman
Chief Scientific Officer
Dr. A. Q. Khan Research Laboratories
P.O. Box No. 502, Rawalpindi

Supervisor :



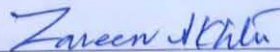
Prof. Dr. Syed Mujtaba Shah
Department of Chemistry
Quaid-i-Azam University
Islamabad.

Head of Section:



Prof. Dr. Hazrat Hussain
Department of Chemistry
Quaid-i-Azam University
Islamabad.

Chairman:



Prof. Dr. Mrs. Zareen Akhter
Department of Chemistry
Quaid-i-Azam University
Islamabad.

Certificate of Approval

This is to certify that the research work presented in this thesis, entitled "Transition Metal Oxide Based Nanocomposites for High Performance Electrochemical Supercapacitor Applications" was conducted by Mr. M. Nasir Hussain under the supervision of Prof. Dr. Sved Mujtaba Shah

No part of this thesis has been submitted any where else for any other degree. This thesis, is submitted to the Department of Chemistry Quaid-i-Azam University Islamabad in partial fulfillment of the requirements for the Doctor of Philosophy in Field of Physical Chemistry, Department of Chemistry, Quaid-i-Azam University, Islamabad.

Student Name

Mr. M. Nasir Hussain

Signature:



Examination Committee:

1. External Examiner:

Dr. Riaz Ahmed Ch.

H. No. 1298, Road H
Phase-3, Bahria Town
Rawalpindi

Signature:



2. External Examiner:

Dr. Hafiz-ur-Rehman

Chief Scientific Officer
Dr. A. Q. Khan Research Laboratories
P.O Box No. 502, Rawalpindi

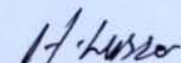
Signature:



3. Internal Examiner:

Prof. Dr. Hazrat Hussain
Department of Chemistry
Quaid-i-Azam University
Islamabad.

Signature:



Supervisor

Prof. Dr. Syed Mujtaba Shah

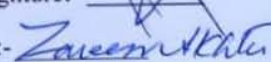
Signature:-



Head of Department:

Prof. Dr. Zareen Akhter

Signature:-



AUTHOR'S DECLARATION

I, **Mr. M. Nasir Hussain** hereby state that my Ph.D. thesis titled "**Transition Metal Oxide Based Nanocomposites for High Performance Electrochemical Supercapacitor Applications**" is my own work and has not been submitted previously by me for taking any degree from this University (Quaid-i-Azam University Islamabad) or anywhere else in the country/world.

At anytime if my statement is found to be incorrect even after my Graduation the University has the right to withdraw my Ph.D. degree.



Name of student: **Mr. M. Nasir Hussain**

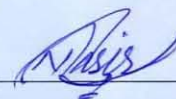
PLAGIARISM UNDERTAKING

I solemnly declare that, the research work presented in the thesis titled "Transition Metal Oxide Based Nanocomposites for High Performance Electrochemical Supercapacitor Applications" is solely my research work with no significant contribution from any other person. Small contribution/help wherever taken has been duly acknowledged and that complete thesis has been written by me.

I understand the zero tolerance policy of the HEC and Quaid-i-Azam University Islamabad towards plagiarism. Therefore, I as an Author of the above titled thesis declare that no portion of my thesis has been plagiarized and any material used as reference is properly referred/cited.

I undertake that if I am found guilty of any formal plagiarism in the above titled thesis even after award of Ph.D. degree, the university reserves the rights to withdraw/revoke my Ph.D. degree and that HEC and the University has the right to publish my name on the HEC/University website on which names of students are placed who submitted plagiarized thesis.

Student/Author Signature: _____



Name: Mr. M. Nasir Hussain

Dedicated

To

My loving parents

*siblings and to those whom prayers enabled me to
complete my studies.*

Table of Contents

ACKNOWLEDGEMENTS	i
ABSTRACT	iii
List of Figures	v
List of Tables.....	xii
List of Abbreviations	xiii
1. Introduction	Chapter # 1..... 1
1.1. Energy Storage	1
1.2. Batteries for Energy Storage	2
1.2.1 Lithium-Ion Batteries (LIBs)	2
1.2.2 Lead-Acid Batteries.....	3
1.2.3 Nickel-Based Batteries	3
1.3. Hybrid Energy Storage Systems.....	4
1.4. Supercapacitors for Energy Storage	4
1.5. Brief History of Supercapacitors	5
1.6. Differences of Supercapacitors from Batteries.....	7
1.7. Electric Double Layer Capacitors (EDLCs).....	9
1.7.1. Helmholtz Model.....	10
1.7.2. Gouy-Chapman Double-Layer Model.....	10
1.7.3. Stern Model.....	11
1.8. Pseudocapacitors	12
1.9. Electrolytes.....	16
1.10. Probing of Thermodynamic and Kinetic for Pseudocapacitive Materials	18
1.11. Transition Metal Oxides for Supercapacitors.....	19
1.11.1. RuO ₂ -Based Supercapacitors	20
1.11.2. MnO ₂ -Based Supercapacitors	23

1.11.3. NiO-Based Supercapacitors	25
1.11.4. V ₂ O ₅ -Based Supercapacitors.....	26
1.11.5. Ni(OH) ₂ -Based Supercapacitors	27
1.12. Carbon-Based Materials for Supercapacitors.....	28
1.12.1. Graphene-Based Supercapacitors.....	29
1.12.2. Graphene Nanosheets Based Supercapacitors	29
1.13. Techniques Used for the Analysis of Supercapacitors	32
1.13.1. Cyclic Voltammetry (CV)	32
1.13.2. Galvanostatic Charge-discharge (GCD).....	33
1.13.3. Electrochemical Impedance Spectroscopy (EIS)	34
1.14. Parameters of Supercapacitors.....	35
1.14.1. Coulombic Efficiency.....	35
1.14.2. Power density (P) and Energy density (E).....	36
1.15. Important Synthetic Methods of Nanomaterials.....	36
1.15.1. Hydrothermal or Solvothermal Method.....	37
1.15.2. Hot-Injection Method	38
1.16. Aims and Objectives	39
1.16.1. Aims.....	39
1.16.2. Objectives	39
2. Experimental	Chapter # 2..... 40
2.1. Chemicals	40
2.2. Material Synthesis	40
2.2.1. Synthesis of Ni(OH) ₂ and NiO Nanoparticles Supported on rGO.....	40
2.2.2. Synthesis of Ag/N,S co-doped TiO ₂ Nanocomposite	41
2.2.3. Synthesis of α-Ni(OH) ₂ and NiO Nanoparticles	41
2.2.4. Synthesis of MnO ₂ Nanoparticles	42
2.2.5. Synthesis of α-Ni(OH) ₂ -MnO ₂ Hybrid Nanocomposite	43

2.2.6. Synthesis of V ₂ O ₅ Nanoparticles, V ₂ O ₅ /GO, and V ₂ O ₅ /rGO Nanocomposites	43
2.2.7. Synthesis of Graphene Oxide (GO) and Reduced Graphene Oxide (rGO) ...	44
2.3. Electrode Fabrication	45
2.4. Physical Characterization with Sample Preparation Method	45
2.4.1. Powder X-ray Diffraction (P-XRD)	45
2.4.2. Raman and FTIR Spectroscopy	45
2.4.3. X-ray Photoelectron Spectroscopy (XPS)	45
2.4.4. Scanning Electron Microscopy (SEM), Elemental Mapping, and Energy-dispersive X-ray (EDX) Spectroscopy	46
2.4.5. Transmission Electron Microscopy (TEM)	46
2.4.6. Thermogravimetric Analysis (TGA) and Differential Scanning Calorimetry (DSC)	46
3. Results and Discussion	Chapter # 3
3.1. Probing the Synergy of Ni(OH)₂/NiO Nanoparticles Supported on rGO for Battery-Type Supercapacitors.....	47
3.1.1. PXRD Analysis	47
3.1.2. XPS Analysis	48
3.1.3. SEM Analysis	49
3.1.4. Elemental Mapping Analysis	50
3.1.5. TEM Analysis	50
3.1.1. Electrochemical Investigation of Nanocomposites for Three-Electrode Configuration.....	51
3.1.1.1. CV Analysis.....	51
3.1.1.2. GCD Analysis.....	53
3.1.1.3. Quantitative Calculation of Surface and Diffusion Capacitance by Dunn's Method.....	54
3.1.1.4. EIS Analysis	55

3.1.2. Electrochemical Investigation of Nanocomposites for Symmetric Devices .	56
3.1.2.1. CV Analysis.....	56
3.1.2.2. GCD Analysis, Cyclic Stability, EIS, Ragone Plots, and Device Architecture.....	57
3.2. Investigating the Impact of Ag Nanoparticles on N and S Co-Doped TiO ₂ for Battery-Type Supercapacitor Application	60
3.2.1. PXRD Studies	60
3.2.2. Raman Studies.....	60
3.2.3. UV-Visible Studies.....	60
3.2.4. Band Gap Studies	61
3.2.5. SEM Studies.....	62
3.2.6. TEM Studies	62
3.2.1. Electrochemical Investigation of Nanomaterials for Three Electrode Configuration.....	63
3.2.1.1. CV Analysis.....	63
3.2.1.2. GCD Analysis, Cyclic Stability, EIS, and Bode Phase Angle Plots.....	65
3.2.1.3. Quantitative Calculation of Surface and Diffusion Capacitance by Dunn's Method.....	66
3.2.2. Electrochemical Investigation of Ag/N, S co-doped TiO ₂ for Symmetric Devices	68
3.2.2.1. CV, GCD, EIS, and Cyclic Stability Analyses.....	68
3.3. Versatile Synthesis of Metal Oxide Nanoparticles to Fabricate High-Performance Electrode Materials for Advanced Supercapacitors	69
3.3.1. PXRD Analysis	69
3.3.2. Raman Analysis	70
3.3.3. XPS Analysis	71
3.3.4. SEM Analysis	72
3.3.5. TEM and FE-SEM Analyses	73

3.3.6. TGA Studies.....	74
3.3.7. DSC Analysis.....	75
3.3.1. Electrochemical Investigation of Nanomaterials for Three Electrode Configuration.....	76
3.3.1.1. CV Investigation.....	76
3.3.1.2. GCD, EIS, and Bode Phase Angle Studies	78
3.3.1.3. Quantitative Calculation of Surface and Diffusion Capacitance by Dunn’s Method.....	80
3.3.2. Electrochemical Investigation of Nanomaterials for Symmetric Devices.....	81
3.3.2.1. CV Investigation.....	81
3.3.2.2. GCD, Cyclic Stability, and Self-Discharge Studies.....	82
3.4. Colloidally Synthesized V ₂ O ₅ Based Nanocomposites Electrode Materials for High-Performance Electrochemical Supercapacitors.....	84
3.4.1. PXRD Studies	84
3.4.2. Raman Analysis	85
3.4.3. SEM Studies.....	86
3.4.4. Elemental Mapping Analysis	86
3.4.5. TEM Studies	87
3.4.1. Electrochemical Investigation of Nanocomposites for Three Electrode Configuration.....	88
3.4.1.1. CV and GCD Investigations.....	88
Conclusions	91
Future Perspectives.....	93
List of Publications Added from this Thesis.....	94
References	93

ACKNOWLEDGEMENTS

First and foremost, I praise Almighty Allah who bestowed me with wellbeing, endurance, capability to think, and strength to execute this project successfully. All respects to Holy Prophet Hazrat Muhammad (Peace be upon him) who urged his followers to pursue knowledge from cradle to grave and who enable us to recognize our creator.

Many exceptional people supported and guided me directly or indirectly throughout this research journey. Though it is hard to mention all of them, I owe them my appreciation and gratitude. I am highly thankful to my supervisor **Prof. Dr. Syed Mujtaba Shah** for his kind cooperation, useful suggestions, thought-provoking guidance, encouraging attitude, pleasant behaviour, and taking a keen interest in this project. Besides, I am grateful to **Prof. Dr. Zareen Akhter** (Chairperson Department of Chemistry), **Prof. Dr. Hazrat Hussain** (Head of Physical Chemistry Section), and the whole staff of the department of chemistry, Quaid-i- Azam University, Islamabad, for their assistance and granted me a fruitful and productive climate for my project.

Above all, I would like to show my thankfulness to the Commonwealth Scholarship Commission (CSC) UK, and University of Bradford, for offering me the precious opportunity to perform a part of my Ph.D. work in this amazing country and institute. I am highly grateful to my host supervisor **Dr. Stephen G. Hickey** (School of Chemistry and Bioscience, UK) for his continuous support, encouragement, constructive input, and guidance. Thank you for everything. It was a great privilege working with you. To be honest, this study would not have been accomplished without your assistance and instruction. Also, my earnest appreciation goes to **Dr. Ali Haider** (Department of Chemistry, Quaid-i-Azam University) for providing me laboratory facilities. Especially for electrochemical investigations and always be on hand for scientific discussions.

I also offer a special thanks to my teachers, **Prof. Dr. Syed Afzal Shah, Prof. Dr. Safeer Ahmad, Prof. Dr. Naveed Kausar Janjua, Prof. Dr. Zia-ur-Rehman, Prof. Dr. Azhar Iqbal**, at Department of Chemistry Quaid-i-Azam University.

I am also grateful for the support and to work with **Mr. Abid Inayat and Mr. Abdul Naveed**. You people have opened for me a different window on chemistry.

I want to express my thankfulness to every one of photovoltaic and materials chemistry lab-01 members for their supportive attitude, valuable suggestions, and work discussion during my studies. Especially **Dr. Naimat Ullah** and **Dr. Rotaba Ansir**, you guys are amazing.

I would like to express my heartfelt gratitude to all of my friends at Quaid-i-Azam University and beyond: to convey my special thanks to all my friends in and outside Quaid-i-Azam University: **Dr. Raja Azadar Hussain, Dr. Malik Dilshad Khan, Dr. Umair Shamraiz, Dr. Abrar Ahmad, Dr. Zahid Nawaz, Dr. Wajid Hussain, Dr. Jamal Abdul Nasir, Dr. Mubeen Butt, Dr. Haseeb Ullah, Dr. Adnan khalid, Dr. Aftab Aziz, Dr. Jahangir Ali, Dr. Haseen Ahmad Khan, Dr. Muhammad Ihsun Nadal(UoB), Mr. Nauman Sadiq, Mr. Zeeshan Ahmad, Mr. Muhammad Zulqarnain, Mr. Sohaib Sarwar, Mr. Sajid Ullah, Mr. Hafiz Muhammad Tufail, Mr. Mohsin Javed**, for their continuous support, insightful guidance, and co-operation they extended throughout this long journey. May Almighty ALLAH provide them with good health and a long and successful life, and may they be a source of prayer for me.

Muhammad Nasir Hussain

nasirhussain@chem.qau.edu.pk

ABSTRACT

The rising energy demand, as well as growing concerns regarding rising levels of environmental pollution and global warming from the usage of fossil fuels, has sparked intense research efforts into exploring the potential of energy generation from alternative renewable and sustainable energy sources and its subsequent storage. Supercapacitor devices have been explored due to their high-power performance, long life cycle and low maintenance costs. In the first part of this thesis, we present a direct hydrothermal synthesis of hydroxide/oxide nanocomposites of nickel grown on reduced graphene oxide (rGO). The materials were employed as a high-performance active layer for advanced supercapacitors. Ni(OH)₂/rGO and NiO/rGO nanocomposites demonstrated a high specific capacitance of 1255.12 and 636.84 F g⁻¹ at 10 mV s⁻¹ obtained from CV curves while 1092.5 and 1070 F g⁻¹ estimated from GCD at 1 A g⁻¹, respectively. Subsequently, symmetric devices with a broad potential window of 1.4 V for both materials were also fabricated. Symmetric devices delivered the maximum specific capacitance of 115.71 and 80.28 F g⁻¹ at 1 A g⁻¹ with an energy density of 31.5 Wh Kg⁻¹ and 22 Wh kg⁻¹ at a power density of 1.4 kW kg⁻¹ which indicates the high-rate capability of the devices. The devices have maximum capacity retention of 81% and 93%, when tested for 1000 discharge cycles at 3 A g⁻¹ showing high cycle stability. The superlative performance of nanocomposites can be of the synergistic effects they exhibit, demonstrating that they are appealing electrode materials for supercapacitor applications.

In the second part of this thesis, we demonstrate a successful synthesis of heteroatom (N,S) co-doped TiO₂ decorated with Ag nanoparticles using a direct combustion approach. These materials serve as a high-performance active layer for advanced battery-type supercapacitors. Among all the investigated materials, N,S co-doped TiO₂ nanoparticles and Ag/N,S co-doped TiO₂ nanocomposite exhibited impressive specific capacitances of 360 and 480 F g⁻¹ at a current density of 1 A g⁻¹. Moreover, we employed Ag/N,S co-doped TiO₂ nanocomposite as a symmetric supercapacitor from -1 to +1 V. The symmetric electrode demonstrated a capacitance of 183 F g⁻¹ at 3 A g⁻¹ with an energy density of 105 Wh kg⁻¹ at a power density of 6 kW kg⁻¹. One of the most promising aspects of this study was the high cyclic stability of the device, with capacity retention of 80% when tested for 3000 discharge cycles at 3 A g⁻¹. The improved electrochemical performance of the Ag decorated N,S co-doped TiO₂

structure confirms the synergistic behaviour of each component in the nanocomposite. These results indicate the remarkable durability of the device. Additionally, the materials used in this work are environmentally friendly, making them attractive candidates for battery-type supercapacitors.

The third part of this thesis reports a newly developed, surfactant-free and scalable methodology for the synthesis of spherical nanoparticles of Ni(OH)₂ and NiO, employing the polar, aprotic solvent, Dimethylformamide (DMF). The methodology was extended to the synthesis of the hybrid nanomaterial Ni(OH)₂-MnO₂ and, with the addition of SDBS, MnO₂ nanoparticles. The nanostructures obtained were evaluated for their ability to be used as electrochemical battery-type supercapacitors. Of all electrode materials investigated in three-electrode configuration, surfactant-free NiO and α -Ni(OH)₂-MnO₂ exhibit the highest values of 1450 F g⁻¹ and 1604.75 F g⁻¹ at 1 A g⁻¹, respectively. Subsequently, symmetric devices were fabricated and tested from 0 to 1 V for all synthesized materials, and their electrochemical performance was investigated. In symmetric devices where surfactant-free NiO and α -Ni(OH)₂-MnO₂ were employed as the active layers and showed specific capacitance of 340 F g⁻¹ and 502 F g⁻¹ at a current density of 1 A g⁻¹ and energy densities of 47.21 Wh kg⁻¹ and 69.72 Wh kg⁻¹ at a power density of 1 kW kg⁻¹ respectively, clearly demonstrating the high capabilities of the symmetric devices. The devices have a maximum capacity retention of 65% and 72% after 5000 cycles at 3 A g⁻¹ demonstrating their high cycle stability.

In the final part of this research dissertation, we present the successful synthesis of V₂O₅ nanoparticles, V₂O₅/GO, and V₂O₅/rGO using a newly developed colloidal method. The reaction parameters were carefully controlled using a single molecular precursor. The as-prepared V₂O₅ and its composites were evaluated for their potential in battery-type supercapacitors. All the materials exhibited excellent specific capacitance performance in three-electrode configurations, with V₂O₅/rGO demonstrating the highest value of 1190 F g⁻¹ at 1 A g⁻¹. These results highlight the high-rate capability of the fabricated device. This impressive performance of the device opens up new possibilities for the use of the above-mentioned materials for state-of-the-art storage systems. Additionally, the materials used in this work are environmentally friendly, making them attractive candidates for battery-type supercapacitors.

List of Figures

Figure 1.1.	Ragone plot. ³⁴	5
Figure 1.2.	Historical background of supercapacitors. The images illustrate the various models. ²⁸	6
Figure 1.3.	A comparative demonstration of conventional supercapacitor and Battery-type: (a, b) CV profiles and (c, d) GCD profiles. ESR, equivalent series resistance. ³⁴	8
Figure 1.4.	Mechanistic illustration of (a) EDLC, (b-d) Various pseudocapacitance. ⁴⁴	9
Figure 1.5.	Graphical illustration of electrical double layer models.	11
Figure 1.6.	Electrochemical energy storage system dependence on materials sizes. (a) The b is evaluated for TiO ₂ nanoparticles from CV at various potentials, (b) Plots of $(i/v^{1/2})$ vs $(v^{1/2})$, (c) CV profiles of different electrodes at constant scan rate, (d) Diffusion and surface contribution of different size TiO ₂ nanoparticles-based electrodes. ¹⁰⁶	16
Figure 1.7.	(a, b) SEM and TEM micrographs of LSG/RuO ₂ system, (c) Graphical illustration of LSG/RuO ₂ showing the diffusion phenomenon, (d) Asymmetric electrode fabrication of supercapacitor, (e) CV profiles of both electrodes, (f) CV profiles of device in wide potential window 1.0 to 2.0 V. ¹⁴⁵	23
Figure 1.8.	(a) Graphical demonstration of graphene hydrogel/MnO ₂ based electrode, (b) Comparative CV profiles of graphene hydrogel and MnO ₂ in three-electrode configuration, (c) CV profiles of graphene hydrogel/MnO ₂ asymmetric device. ¹⁶⁹	25
Figure 1.9.	(a, b) As synthesized Au-V ₂ O ₅ -MnO ₂ nanoflower composites, (c, d) CV profiles of Au-V ₂ O ₅ -MnO ₂ and V ₂ O ₅ with respect to potential at various current per gram, (e, f) GCD profiles Au-V ₂ O ₅ -MnO ₂ and V ₂ O ₅ .	27
Figure 1.10.	(a, b) CV profiles of 3D carbon network, (c) GCD profile at a current density of 1 A g ⁻¹ .	29
Figure 1.11.	Schematic illustration for the exfoliation of the graphene. ²⁰¹	30
Figure 1.12.	Graphical representation for the synthesis of chemically produced graphene. ¹⁹⁵	31
Figure 1.13.		33

(a) CV profiles, (b-e) CV profiles of GN1, GN2, GN5, and GN10 at various scan rates, (f) CV profiles of rGO at various scan rates.²¹⁸

Figure 1.14.	(a) GCD profiles of potential candidate GN2, (b) GCD analysis of GN1, GN2, GN5, and GN10 at 2 A g ⁻¹ . ^[218]	34
Figure 1.15.	Nyquist plots with corresponding fitting data of given samples at open circuit voltage. ²¹⁸	35
Figure 1.16.	Capacitance retention and coulombic efficiency of 1D β-MnO ₂ nanowires in aqueous electrolyte. ²¹⁹	36
Figure 2.1.	Schematic Illustration of Ni(OH) ₂ and NiO nanoparticles grown on rGO by direct hydrothermal approach.	41
Figure 2.2.	Illustration of Ag/N,S co-doped TiO ₂ nanocomposite synthesis.	41
Figure 2.3.	Schematic illustration for the synthesis of α-Ni(OH) ₂ and NiO nanoparticles.	42
Figure 2.4.	Schematic illustration for the synthesis of MnO ₂ nanoparticles.	42
Figure 2.5.	Schematic illustration for the synthesis of α-Ni(OH) ₂ -MnO ₂ nanocomposite.	43
Figure 2.6.	Schematic illustration for the synthesis of V ₂ O ₅ nanoparticles, V ₂ O ₅ /GO, and V ₂ O ₅ /rGO nanocomposites.	44
Figure 2.7.	Schematic illustration for the synthesis GO and rGO.	44
Figure 3.1.	PXRD patterns of (a) Ni(OH) ₂ nanoparticles, (b) NiO nanoparticles, (c) Ni(OH) ₂ /rGO nanocomposite, (d) NiO/rGO nanocomposite.	48
Figure 3.2.	XPS spectra of Ni(OH) ₂ /rGO nanocomposite, (a) Ni-2p, (b) C-1s, (c) O-1s, and NiO/rGO nanocomposite, (d) Ni-2p, (e) C-1s, (f) O-1s.	49

Figure 3.3.	SEM images a) Ni(OH) ₂ nanoparticles, b) NiO nanoparticles, c) Ni(OH) ₂ /rGO nanocomposite, d) NiO/rGO nanocomposite.	49
Figure 3.4.	Elemental mapping images of Ni(OH) ₂ /rGO nanocomposite.	50
Figure 3.5.	TEM images a) Ni(OH) ₂ nanoparticles, b) NiO nanoparticles, c) Ni(OH) ₂ /rGO nanocomposite, d) NiO/rGO nanocomposite.	51
Figure 3.6.	Cyclic voltammogram for the fabricated electrodes a) Ni(OH) ₂ nanoparticles, b) Ni(OH) ₂ /rGO nanocomposite, c) NiO nanoparticles, d) NiO/rGO nanocomposite.	52
Figure 3.7.	GCD profiles of a) Ni(OH) ₂ nanoparticles, b) Ni(OH) ₂ /rGO nanocomposite, c) NiO nanoparticles, d) NiO/rGO nanocomposite.	54
Figure 3.8.	Percentage analysis of surface and diffusion capacitance for Ni(OH) ₂ /rGO and NiO/rGO nanocomposites using Dunn's method (a, c) Plots of (i/v ^{1/2}) vs (v ^{1/2}), (b, d) Contribution from both the capacitance at various scan rates.	55
Figure 3.9.	Nyquist plots.	56
Figure 3.10.	(a, c) Optimisation of voltage window for Ni(OH) ₂ /rGO and NiO/rGO, (b, d) CV profiles of Ni(OH) ₂ /rGO and NiO/rGO at various scan rates.	57
Figure 3.11.	GCD profiles of a) Ni(OH) ₂ /rGO nanocomposite, b) NiO/rGO nanocomposite, c) Cyclic stability, d) Nyquist plots, e) Ragone plots, f) Schematic representation of symmetric device.	59
Figure 3.12.	(a) XRD patterns, (b) Raman spectra, (c) UV-Vis profiles, and (d) Tauc's plots of pristine TiO ₂ nanoparticles, N,S co-doped TiO ₂ nanoparticles, and Ag/N,S co-doped TiO ₂ nanocomposite.	61

- Figure 3.13.** Presents SEM images of various materials: a) pristine TiO₂ nanoparticles, b) N,S co-doped TiO₂ nanoparticles, c) Ag/N,S co-doped TiO₂ nanocomposite, and d) EDS mapping of the Ag/N,S co-doped TiO₂ nanocomposite with images of each element. 62
- Figure 3.14.** TEM images a) pristine TiO₂ nanoparticles, b) N,S co-doped TiO₂ nanoparticles, c) Ag/N,S co-doped TiO₂ nanocomposite, and (d, e, f) SEM images of all materials after stability test. 63
- Figure 3.15.** Shows the following: a) CV curves at different electrolytes, b) Comparative CV profiles of the Ag/N,S co-doped TiO₂ nanocomposite in KOH, NaOH, and LiOH, b) CV curves in different concentrations of KOH, d) pristine TiO₂ nanoparticles, e) N,S co-doped TiO₂ nanoparticles, f) Ag/N,S co-doped TiO₂ nanocomposite. 64
- Figure 3.16.** GCD profiles of a) pristine TiO₂ nanoparticles, b) N,S co-doped TiO₂ nanoparticles, c) Ag/N,S co-doped TiO₂ nanocomposite, d) cyclic stability, e) Nyquist plots, f) Bode phase angle plots. 66
- Figure 3.17.** A quantitative analysis of surface and diffusion capacitance is presented for N,S co-doped TiO₂ nanoparticles and Ag/N,S co-doped TiO₂ nanocomposite. Panels (a) and (c) Plots of $(i/v^{1/2})$ vs $(v^{1/2})$, (b, d) illustrate the contribution from surface and diffusion capacitances at different scan rates. 67
- Figure 3.18.** (a, b) CV and GCD profiles of fabricated symmetric device of Ag/N,S co-doped TiO₂ nanocomposite, c) EIS profile, d) cyclic stability. 69

- Figure 3.19.** PXRD of (a) of α -Ni(OH)₂ nanoparticles, (b) NiO nanoparticles, (c) MnO₂ nanoparticles, (d) α -Ni(OH)₂-MnO₂ hybrid nanomaterial. 70
- Figure 3.20.** Raman spectra of (a) of α -Ni(OH)₂ nanoparticles, (b) NiO nanoparticles, (c) MnO₂ nanoparticles, (d) α -Ni(OH)₂-MnO₂ hybrid nanomaterial. 71
- Figure 3.21.** XPS profiles of α -Ni(OH)₂-MnO₂ hybrid before, a) Ni-2p, (b) Mn-1p, (c) O-1s, and after stability tests, d) Ni-2p, e) Mn-1p, f) O-1s. 72
- Figure 3.22.** (a, b, c, d) on the top row are SEM of α -Ni(OH)₂, NiO, MnO₂, and α -Ni(OH)₂-MnO₂ hybrid, while on the bottom row are elemental mapping images of (e) α -Ni(OH)₂-MnO₂ nanostructures followed by images of the Mn, Ni and O distributions. 73
- Figure 3.23.** (a, b, c, d) TEM of α -Ni(OH)₂, NiO, MnO₂, and α -Ni(OH)₂-MnO₂ hybrid nanomaterials, (e, f, g, h) FE-SEM of α -Ni(OH)₂, NiO, MnO₂, and α -Ni(OH)₂-MnO₂ hybrid films after cyclic stability tests. 74
- Figure 3.24.** TGA spectra of the nanomaterials. 75
- Figure 3.25.** DSC spectra of the nanomaterials. 76
- Figure 3.26.** CV profiles of α -Ni(OH)₂, NiO, MnO₂, and α -Ni(OH)₂-MnO₂ hybrid in (a) KOH, (b) NaOH, and (c) LiOH. CV profiles recorded at different scan rates in 2 M KOH of (d) α -Ni(OH)₂, (e) NiO, (f) MnO₂, and (g) α -Ni(OH)₂-MnO₂ hybrid. 78
- Figure 3.27.** GCD profiles of (a) α -Ni(OH)₂ nanoparticles, (b) NiO nanoparticles, (c) MnO₂ nanoparticles and (d) α -Ni(OH)₂- 80

- MnO₂ hybrid. Nyquist plots (e) and Bode plots (f) for all four materials.
- Figure 3.28.** Quantitative capacitive analysis of NiO nanoparticles and α -Ni(OH)₂-MnO₂, (a, c) Plots of $(i/v^{1/2})$ vs $(v^{1/2})$, (b, d) Contribution of surface and diffusion capacitances. 81
- Figure 3.29.** CV profiles of symmetric devices of a) α -Ni(OH)₂ nanoparticles, b) NiO nanoparticles, c) MnO₂ nanoparticles and d) α -Ni(OH)₂-MnO₂ hybrid. 82
- Figure 3.30.** GCD analysis of symmetric devices a) α -Ni(OH)₂ nanoparticles, b) NiO nanoparticles, c) MnO₂ nanoparticles, d) α -Ni(OH)₂-MnO₂ hybrid, (e) Cyclic stability and coulombic efficiency and (f) self-discharge curves. 83
- Figure 3.31.** (a) Nyquist plots after cyclic stability test, (b) Ragone plots of fabricated symmetric devices. 84
- Figure 3.32.** (a) PXRD patterns of V₂O₅ nanoparticles (black), V₂O₅/GO nanocomposite (red), V₂O₅/rGO nanocomposite (blue), (b) Raman spectra of nanostructures V₂O₅ nanoparticles (black), V₂O₅/GO nanocomposite (red), V₂O₅/rGO nanocomposite (blue). 85
- Figure 3.33.** SEM micrographs of nanostructures (a) V₂O₅ nanoparticles, (b) V₂O₅/GO composite, (c, d) V₂O₅/rGO composite. 86
- Figure 3.34.** Elemental mapping images and EDX spectrum of V₂O₅/GO composite. 87
- Figure 3.35.** TEM images of nanostructures (a, b) V₂O₅ nanoparticles, (c) V₂O₅/GO composite, (d) V₂O₅/rGO composite. 88

Figure 3.36. a) CV profiles a) V_2O_5 nanoparticles, b) V_2O_5/GO nanocomposite, c) V_2O_5/rGO nanocomposite, and GCD profiles of d) V_2O_5 nanoparticles, e) V_2O_5/GO nanocomposite, f) V_2O_5/rGO nanocomposite.

90

List of Tables

Table 3.1	Specific Capacitance ($F g^{-1}$) Calculated from CV.	53
Table 3.2	Specific Capacitance ($F g^{-1}$) Calculated from GCD.	54
Table 3.3	Comparison of $Ni(OH)_2/rGO$ and NiO/rGO Performance with Literature Reports.	59
Table 3.4	Specific Capacitance ($F g^{-1}$) Calculated from GCD.	66
Table 3.5	Specific Capacitance Values of Nanomaterials Calculated from GCD in $F g^{-1}$.	80
Table 3.6	Specific Capacitance Values of Nanomaterials Calculated from GCD in $F g^{-1}$.	90

List of Abbreviations

rGO	Reduced Graphene Oxide
GO	Graphene Oxide
CV	Cyclic Voltammetry
GCD	Galvanostatic Charge Discharge
EIS	Electrochemical Impedance Spectroscopy
E	Energy Density
P	Power Density
Z _{im}	Imaginary Impedance
Z _{re}	Real Impedance
ESR	Effective Series Resistance
LIBs	Lithium-Ion Batteries
HESS	Hybrid Energy Storage Systems
DOE	Department of Energy
EDLC	Electrochemical Double Layer Capacitor
IHP	Inner Helmholtz Plane
OHP	Outer Helmholtz Plane
CAN	Acetonitrile
PC	Propylene Carbonate
CVD	Chemical Vapor Deposition
CQDs	Colloidal Quantum Dots
DMF	Dimethylformamide
CTAB	Cetyl Trimethyl Ammonium Bromide
P-XRD	Powder X-ray Diffraction
XPS	X-ray Photoelectron Spectroscopy
SEM	Scanning Electron Microscopy
EDX	Energy-dispersive X-ray Spectroscopy
TEM	Transmission Electron Microscopy
TGA	Thermogravimetric Analysis
DSC	Differential Scanning Calorimetry
PVDF	Polyvinylidene Fluoride
NMP	N-Methyl-2-Pyrrolidone

1.1. Energy Storage

In the modern world, the demand for more energy looks to be rising steadily. Massive amounts of power are required by both industry and households. Meanwhile, the current energy production sources are simultaneously facing new problems.¹⁻² Global efforts are aimed at regulating pollution levels, addressing the challenges of global warming by implementing strategies to decrease carbon dioxide emissions, and several nations have decided to dismantle current nuclear power plants instead of building new ones.³ Furthermore, there has been a substantial increase in the cost of traditional energy resources, need for a steady and unaltered supply of these sources, given the significant worldwide increase in energy usage. Therefore, development of new energy production methods is required. Many recent techniques are already in use in the commercial sector, while most of are now being developed, such as the intriguing nuclear fission power. On a global scale, the significance of alternative energy sources and other viable reservoirs is rising. These energy alternatives are wind and solar energy which rely on weather conditions or climate for their effective operation.⁴ There are certain obvious benefits of using these new energy sources over more traditional ones. However, they are presenting some new challenges. The output of conventional techniques is simple to modify in accordance with power requirements. On the other hand, the peak power outputs of the new energy sources may not match the necessary power levels since they are more directly capture the energy from the nature. Their power output may vary significantly over the periods of months or even yearly cycles. Additionally, the requirements may fluctuate on a weekly or annual basis. Therefore, the energy must be stored from these new sources to become dependable as main energy sources. Typically, energy from these sources needs to be stored during periods of high output and released during periods of low demand. Energy storage technologies are therefore a vital and necessary components of distributed generation units. Large amounts of energy must also be stored for other reasons. The distribution of storage may also assist the network withstand peaks in demand, depending on how it is distributed. Energy storage enables distribution and transmission to run at maximum efficiency, reducing the need for newer or better lines and raising plant productivity.

There is obviously energy storage is required, especially on a higher level than ever before. Conventional energy storage techniques, such the electrochemical cell, may not be suitable for industrial-scale systems, and their effectiveness may not be at its highest potential. In the meantime, numerous innovative and promising techniques are being developed. Some of them are brand-new concepts, while others are conventional ideas updated for use in contemporary energy storage. Some are more developed than others, but most can yet be improved.

Here, the most significant energy storage technologies currently in use or development are discussed in detailed. It is obvious that the technology and underlying concepts for each storage method can differ greatly, thus the range of available energy storage products can be diversified significantly. This means that each approach can vary according to its own application for environment and energy storage scale. More precisely, one method of storing energy might be perfect for smooth out the yearly fluctuation while another might be appropriate to meet the short power requirements. Eventually, the comparison between the various methods is undertaken, in order to understand the fundamental difference of each methodology, where applicable.

1.2. Batteries for Energy Storage

Electric energy-based motors and generators first entered into human life during the second industrial revolution, and they have since dominated the secondary energy sources that keep human civilization alive. It is extremely difficult to store electric energy than production and consumption because does not have the similar properties as of fuel or coal and can only be achieved through efficient energy conversion. The invention of the batteries was prompted by the development and use of the power equipment's. Batteries are stored energy because of faradaic reactions that takes place at anode and cathode.⁵ There is a variety of batteries available in the market depending on their chemical structure. Currently, three most common types of rechargeable batteries are being used in vehicles including lithium-ion, lead acid and nickel-metal hydride batteries.

1.2.1 Lithium-Ion Batteries (LIBs)

LIBs have been discovered in 1970s and got popularity in 1990s. LIBs demonstrated energy density of ($>180 \text{ Wh kg}^{-1}$) because of redox reactions. LIBs show

very long charge/discharge time due to the ion diffusion kinetic process occurring at the electrode. Therefore, LIBs are frequently used in domestic gadgets such as laptops, smartphones, and many others that need more capacity as to resist the faster charge/discharge rate. LIBs are the state of the art technology utilized in the automobiles because of their features e.g., low mass, high specific power and energy densities.⁶⁻⁹ Moreover, LIBs are memory free with absence of any toxic materials like lead, mercury, and cadmium etc. LIBs are fabricated by many electrochemical cells which relate to each other into a module before making the battery pack. When compared to other battery types, biggest disadvantage of LIBs is their higher cost. According to the manufacturer, LIBs are fabricated of interconnected cells that have different lengths, widths, and heights as well as shapes e.g., pouch, prismatic, and cylindrical. The structure of the battery packs needs to be improved including the engineering and chemical components. The shape of the cell, module, and pack must be maintained in way that the overall weight and volume should be low with highest efficacy. To increase the current storage capacity of the LIBs, significant modification is required in the chemistry of the electrolyte and electrode.¹⁰ In the recent years, development in the durability of the electrolyte is a big challenge for the researchers. Modifications are necessary to the chemistries of batteries like Li-S, and metal-air for the bright future of the electric vehicles (EVs). Since the battery's performance limit is anticipated to be reached in 2030, advances in cell chemistry and technology are crucial. However, there has been a significant advancement seen in the energy density of the batteries.

1.2.2 Lead-Acid Batteries

Lead-acid batteries have been extensively employed in the household and commercial purposes due to their rechargeable electrochemical nature. The demands of the lead-acid batteries are increasing immensely because of many features including low cost, high energy efficiency (>80%).⁶ rapid response time, and extremely low discharge rates (up to 2% per month). On the other hand, the low energy density of 30–50 Wh/kg,⁶ and low cycle life cycle life of up to 1500 cycles [18] are the disadvantages. Moreover, in the parallel fashion, the use of lead also has negative effects on the environment and human health.^{7, 11}

1.2.3 Nickel-Based Batteries

There are four types of nickel-based batteries such as nickel-iron, nickel-cadmium, nickel-metal hydride, and nickel-zinc.¹² The positive electrode is nickel hydroxide, while the electrolyte is predominantly lithium hydroxide combined with an

aqueous potassium hydroxide solution. On contrary, cadmium hydroxide is used as negative electrolyte in nickel-cadmium type while an alloy of metal is being used in nickel-metal hydride type, and zinc hydroxide in the nickel-zinc.⁸ The energy densities for alkaline batteries from 50 Wh/kg to 95 Wh/kg, which higher than those of lead-acid batteries. nickel-cadmium batteries demonstrated very high operating and life cycle up to 10,000 cycles.^{6, 8, 12}

1.3. Hybrid Energy Storage Systems

To overcome the problems associated with the single energy source in the electric vehicles, a dual-source hybrid energy storage systems (HESS) has been developed by combining the two energy sources. There are numerous advantages of HESS over single storage system, including the long life, storage capacity, low cost and volume etc.¹³ The basic motivation for the fabrication of these hybrid systems is to improve the overall power and energy density. Furthermore, a variety of dual source systems are discussed in the literature. Massive research focused on combining the battery and supercapacitors to improve the storage capacity of the HESS,¹⁴ although the other configurations have many advantages over it. As a result, combination of various storage technologies can benefit from each other's complementary properties. This combination has gained a massive attention because of its comparable operational concept, broad availability, and low starting cost.¹⁵

1.4. Supercapacitors for Energy Storage

The demands of energy on global scale have immensely increased while the resources of fossil fuels are depleting by the consistent emission of the greenhouse gases.¹⁶⁻¹⁸ These issues can be resolved by using renewable energy sources such as solar, wind and hydropower.¹⁹⁻²³ It is necessary to store electricity generated from the various sources effectively to meet the world energy demands.²⁴⁻²⁶ As a result, numerous storage technologies are being carefully examined in order to create cutting-edge devices, as seen in the Ragone plot **Figure 1.1**.^{25, 27-33}

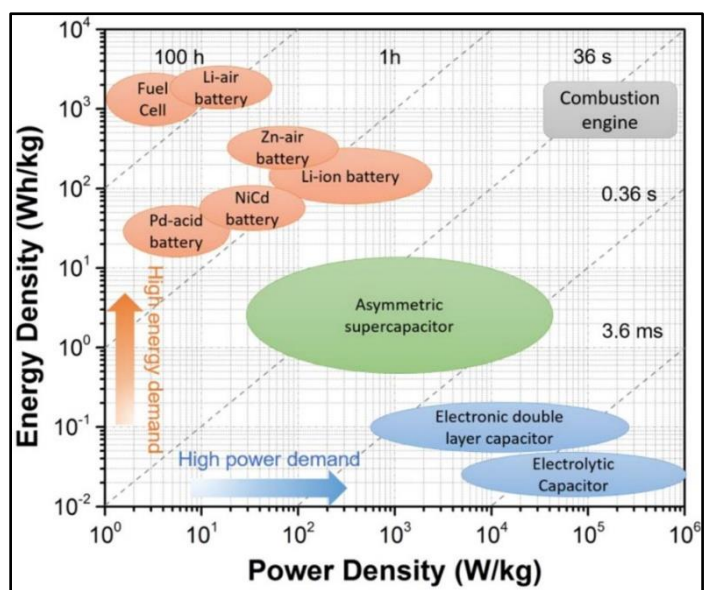


Figure 1.1. Ragone plot.³⁴

These days, consumer electronics typically use lithium-ion batteries.^{30, 35} There are several health and safety issues associated with batteries because of a number of resistive losses brought on by delayed charge transportation, such as significant heat generation and dendrite formation.³⁶ Some well-publicized faults have been noticed in Tesla's electric automobiles and Boeing's Dreamliner jets. Supercapacitors may easily replace batteries since they can provide high power and fast charging while also having a long cycle life (>100000 cycles).³⁷⁻⁴⁰ Supercapacitors are gaining a huge interest in applications that need fast charging, very high cyclic stability, and power density. For instance, heavy-duty vehicles, hybrid truck and bus platforms, are all use supercapacitors.²⁵ Supercapacitors, on the other hand, are still much less powerful than batteries and fuel cells but energy density (5 Wh kg^{-1}) comparative to capacitors with solid phase electrolyte. Due to the limited global use of supercapacitors, significant research is underway to obtain high energy-storage capabilities in batteries. Therefore, a rational design is required to resolve the issues associated with the low energy densities in the supercapacitor devices.

1.5. Brief History of Supercapacitors

Historically, the development of the supercapacitor is based on the discovery of the storage mechanism. The first supercapacitor was invented in 1745 and 1746 by Ewald Georg von Kleist, a German priest, and Pieter van Musschenbroek, a Dutch scientist. The simplest "Leyden jar" design, as depicted in **Figure 1.2**, composed of two metal plates, water and conductive a chain. The static electricity was generated by the

rotation of the glass jar and energy stored at interface. This was first idea of the EDLCs until discovery of the battery in 1980.

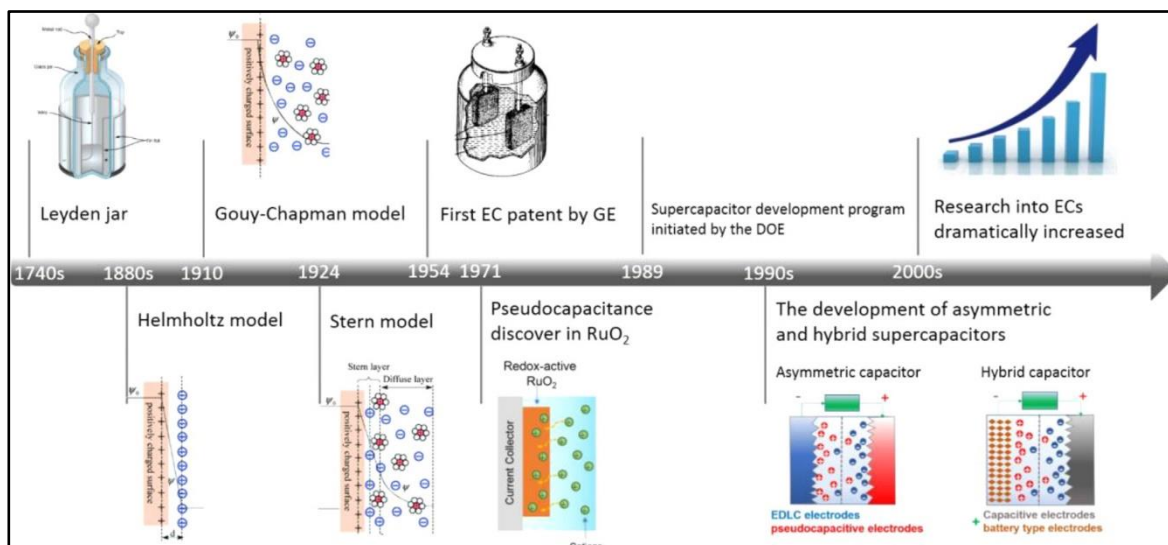


Figure 1.2. Historical background of supercapacitors. The images illustrate the various models.²⁸

In 1853, Von Helmholtz has fabricated the first electrical double-layer using colloidal suspensions and fully described the mechanism that how much a capacitor can store energy. Gouy,⁶² Chapman, Stern, and Grahame were earlier electrochemists who proposed the contemporary concept of EDLC capacitance of electrode and electrolyte by end of 19th and start of the 20th century. In 1971, the Faradic process was used to produce a novel electrochemical capacitor based on RuO₂ called pseudocapacitor.⁴¹ The charge-storage mechanism of RuO₂ based electrode's is Faradaic in nature, and cyclic voltammogram (CV) profile is rectangular, demonstrating its characteristic capacitive behaviour. On the other hand, the development of the pseudocapacitor opened up new methodologies to bring advancement in the electrochemical capacitors. The Peninsula Research Institute (PRI) began work on the PRI Ultracapacitor project in the 1980s to produce RuO₂ and tantalum oxide based pseudocapacitors.

In order to provide high performance supercapacitors for electric and hybrid vehicles, the US Department of Energy (DOE) started funding supercapacitor research..⁴² As a result, Maxwell Technologies, Inc., and DOE signed a world-leading contract to develop high energy density supercapacitors. The aim of project was to assemble a state-of-the-art power system for hybrid vehicles. Until now, there are many different

types of supercapacitors that are currently available in the market. Each has unique properties and uses, such as providing backup energy storage for portable devices and heavy vehicles. The biggest producers of supercapacitors worldwide are CAP-XX (Australia), ELTON (Russia), Nippon Chemicon (Japan), and Nesscap (Korea).

Since the beginning of this century, supercapacitor research has been a promising topic of interest for scientists due to the increasing demand of energy. Despite this, based on major developments in nanoscience and characteristic techniques, researchers have discovered many new physical and electrochemical processes for all kind of supercapacitive systems. However, the charge storage mechanism of supercapacitors has remained unclear as of yet.

1.6. Differences of Supercapacitors from Batteries

The devices that use extremely quick Faradaic reactions to store energy are called supercapacitors. The faradaic processes occurred at the interface of electrode due to the metal oxides, conductive polymers and extremely porous carbon are used. The charge storage mechanism in supercapacitors is identical to traditional capacitors, but the energy and power densities have been enhanced by a factor of 100000 even more than a typical capacitor. The performance of the device can be achieved by materials with thousand times greater areas, dielectric distances, and quick Faradaic reactions which can add extra pseudocapacitance. A single supercapacitor device may store thousands of Farads, far higher than micro and milli-Farads by a conventional capacitor. Supercapacitors also have the advantage of being able to discharge energy at a faster rate than current generation of the batteries. Despite their increased power density, supercapacitors have few other benefits over batteries i.e., high safety and long cycle stability. The most fundamental features that distinguishes supercapacitors from batteries is the linear voltage increase when charged or discharged at constant current,⁴³ as seen in **Figure 1.3**.

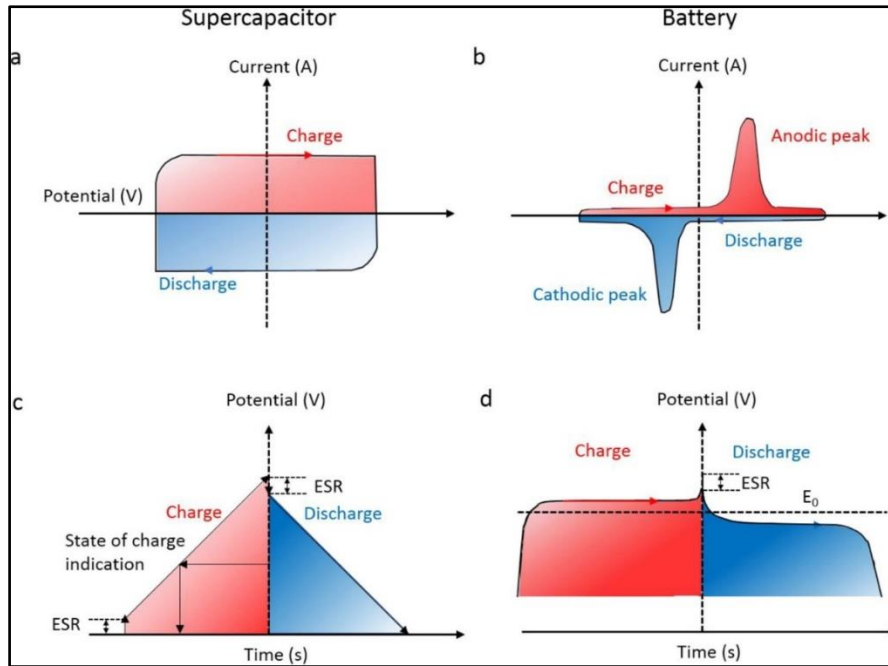


Figure 1.3. A comparative demonstration of conventional supercapacitor and Battery-type: (a, b) CV profiles and (c, d) GCD profiles. ESR, equivalent series resistance.³⁴

In the case of an applied potential scan, the capacitance is independent of potential. Therefore, voltammogram behaviour of the supercapacitor remains rectangular shape. The batteries exhibit their own peaks with substantial Faradic current. When studying galvanostatic charge/discharge curves (GCD) batteries typically shows a flat plateau at a fixed voltage, but supercapacitors have a tilted form with a constant slope. Meanwhile, supercapacitors must be connected with the DC-DC convertor to control the out-put voltage, where a constant voltage required. The energy stored in the electrodes has a different definition and unit due to the difference in charge-storage mechanisms. The capacitance of a capacitive electrode calculated using equation (1).

$$C = \frac{\Delta Q}{\Delta U} \quad (1)$$

ΔQ is stored charge and ΔU applied voltage. C is capacitance in Farad (F). Recently, a massive publication demonstrating the difference of electrochemical behaviour between both the energy storage devices (supercapacitors, batteries).⁴⁴⁻⁴⁵ However, EDLCs and pseudocapacitors storage systems are represented in the **Figure 1.4**.

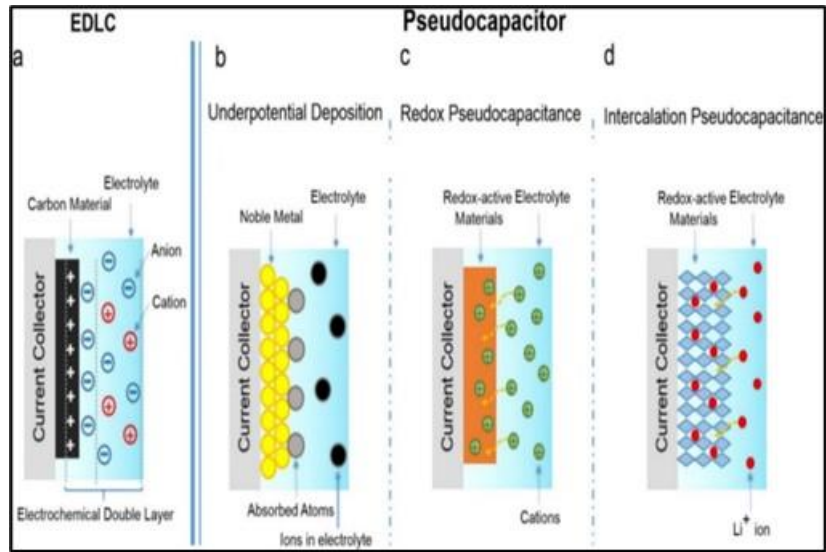


Figure 1.4. Mechanistic illustration of (a) EDLC, (b-d) Various pseudocapacitance.⁴⁴

1.7. Electric Double Layer Capacitors (EDLCs)

Generally, a double layer is often forms when an electrolyte is applied to a conductive electrode because charges accumulate at the electrode-electrolyte contact. The simplest commercially available supercapacitor is the EDLCs in which charge store due to the accumulation of the ions at electrode interface.^{28, 38, 46-50} EDLCs performance is significantly influenced by the unique surface properties of carbon materials being used for the fabrication of device. The capacitance of EDLCs determined by equation (2).

$$C = \frac{\epsilon_r \epsilon_0}{d} A \quad (2)$$

where A is the area of the materials, ϵ_r stands for the electrolyte permittivity, ϵ_0 , and d for separation between electrical double layers.

EDLCs storage capacity can be increase by enhancing the surface area and the charge separation length of than a conventional capacitor. Numerous carbon base materials, among them are activated carbon,⁵¹⁻⁵³ carbon aerogels, to carbon nanomaterials,⁵⁴ including carbon nanotubes,⁵⁵⁻⁶² and graphene,^{58, 63-75} have all been used as electrode materials. The thickness of the device can be found by the size and concentration of ions, as well as solvent sphere, which ranges from 5-10 Å. Carbon-base devices shows capacitance is in the range between 10 and 21 $\mu\text{F cm}^{-2}$ depending on the effectiveness of double-layer and permittivity of the medium. Thus, devices having high carbon surface area can have performance of 300-550 F g^{-1} . However, inaccessibility of active

sites has reduced the capacitance of pure carbon based EDLCs up to 100-250 F g⁻¹.²⁸ Therefore, commercially available EDLC electrode materials have an energy storage capacity of 3–10 Wh kg⁻¹. However, D.C. Graham has labelled the double layers into three parts and given them the name, (1) inner Helmholtz plane (IHP), (2) outer Helmholtz (OHP), and (3) diffused layer, respectively. In some cases, the inner Helmholtz plane exist due to some specific ions at the electrode surface. While for outer Helmholtz plane, an ion should be surrounded by solvent through which the plane pass.⁷⁶ The Helmholtz model, Gouy-Chapman model, and Stern model are three models that support the idea of double layer. The all models are described below.

1.7.1. Helmholtz Model

The distribution of opposing charge at the interface of the colloid particles was first represented by Helmholtz model in 1879, displayed in **Figure 1.5(a)**. In this model, counter ions are neutralized by a separation ‘d’ which is known as the charge’s approximation. As a result, electrostatic forces of interactions have been developed within the surface and opposing ions present in the solution. On the other hand, the main disadvantage is that ions in the double layer are not stable and fluctuate due to thermal behaviour. Additionally, this model does not take into consideration the solvent/surface interaction, ion diffusion, and surface adsorption. Also, the surface charge potential is the rate at which counter-ions linearly dissipate to the surface of the electrode.⁷⁷⁻⁷⁸

1.7.2. Gouy-Chapman Double-Layer Model

In 1910, Gouy-Chapman model has been developed, which investigates the kinetic energy of ions based on the thickness of the diffuse layer. An essential factor in this theory is the concentration of ions, which follows the statistical principles of Maxwell distribution. However, Boltzmann law anticipates that the probability of a subsystem is always in equilibrium with a specific energy.

The relation of number density and kinetic energy of the ions which used to bring them at a distance ‘r’ from the infinity at a given temperature can be expressed by equation (3).

$$n(r) = N \exp\left(-\frac{V(r)}{TK_b}\right) \quad (3)$$

The notation used here, n(r) for ion distribution, N represents the number density of the ions, V(r) for potential, K_b, and T are being used for Boltzmann constant and temperature, respectively. It is assumed that the ions are particular point charges that

exhibit forces of interactions but do not show polarizability, adsorption, and absence of IHP or OHP. **Figure 1.5(b)** illustrates the Gouy-Chapman model, which addresses the limitations of the Helmholtz model that involves the influence of thermal fluctuations. According to this model, the interface potential is established at double layer of electrode surface, which is a result of the existence of charged ions. These ions are surrounded by the same number of opposite charge ions that permeate through the electrolyte. However, the Gouy-Chapman model also has its own disadvantages, such as the assumption of point charges and inappropriate location of potential close to the electrode surface are incorrect.⁷⁹

1.7.3. Stern Model

The Stern model was introduced in 1924 with some modification to explain the limitations of the Gouy-Chapman model, as shown in **Figure 1.5(c)**. This modified new model integrates the aspects of both the models which clearly differentiate the two regions of the ion distribution. The first region, referred to as the Stern layer, and the second region, known as the diffuse layer, are identified in this model. Within the Stern layer, the electrode exhibits a strong adsorption of ions in a hydrated form. These adsorbed ions are categorized as particular adsorbed ions and non-particular adsorbed counter ions. Furthermore, these ions can be identified as IHP and OHP. The subsequent region, which is diffuse layer, follows the Gouy-Chapman model.²⁸

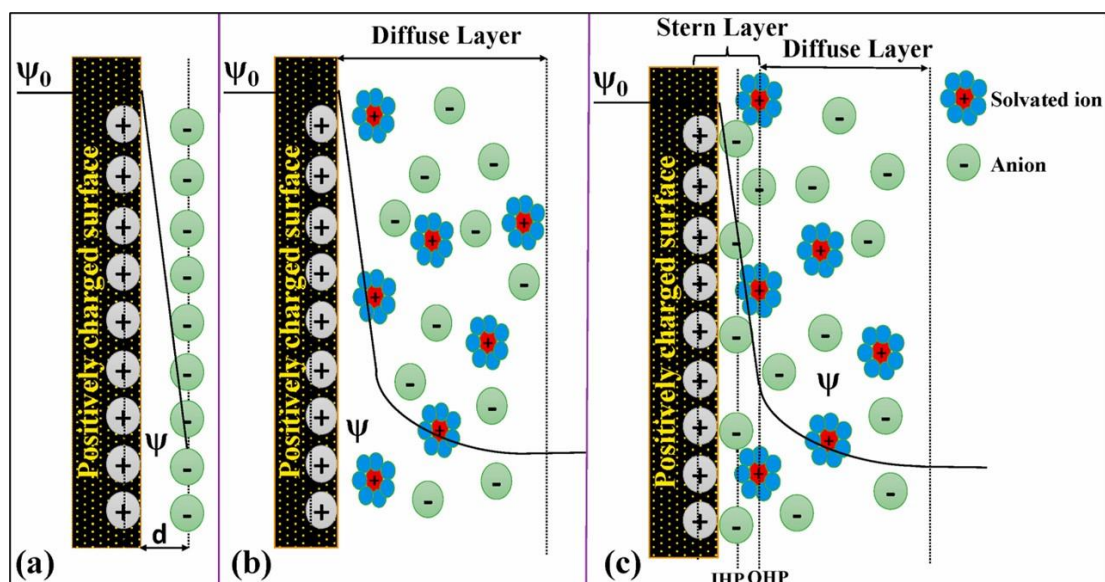


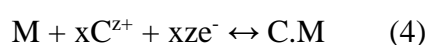
Figure 1.5. Graphical illustration of electrical double layer models.

1.8. Pseudocapacitors

Pseudocapacitors store charge through Faradaic processes, which caused by the redox materials. The mechanism of the redox reactions is related to transportation of electrons in the valence state of the electrode materials.^{44, 80-81} The first metal oxide substance to be investigated and show pseudocapacitive behaviour was ruthenium dioxide (RuO₂). However, the charge transfer phenomena happened in RuO₂ demonstrated the Faradaic reactions while the CV shapes are rectangular, which represents the capacitive nature of the material.⁴⁴ Generally, the materials store charge through Faradaic reactions across the double layer are referred to as pseudocapacitive materials.^{44, 82} The capacitance is calculated through the relationship between the charge extent (Q) and potential change (ΔU), caused by the Faradaic reactions. One of the main factors that affects the pseudo capacitance is the active sites, which are located at a distance of $\ll(2Dt)^{1/2}$ the metal oxide surface, The D represents the diffusion coefficient ($\text{cm}^2 \text{s}^{-1}$) while t is being used for diffusion time (s). Pseudocapacitive based systems displays an electrochemical behaviour that exhibits in between the double-layers as well as in solid-state which controlled by redox process in battery-type materials. However, various redox reactions are appeared due to the electrochemical capacitive phenomena as displayed in the **Figure 1.4(b-d)**.^{44, 83}

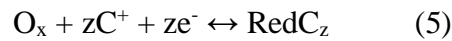
1) underpotential deposition, where ions are deposited at the interface of the metal-electrolyte and potential is positive with respect to reversible potential such as H⁺ on Pt or Pd²⁺ on Au metal. 2) redox potential, the reduced materials are electrochemically absorbed on the surface of oxidized materials in the faradaic processes such as RuO₂⁸⁴⁻⁸⁷ or MnO₂⁸⁸⁻⁹⁰ and conducting polymers etc).^{54, 91-93} 3) intercalation pseudocapacitance, in which ions diffusion or intercalation occurred into the redox-active species without phase change in the materials and very close to EDLs e.g., Nb₂O₅.⁹⁴⁻⁹⁸

Typically, hydrogen is deposited onto the surface of Pt, Rh, and Ir metals and carried out by underpotential deposition while in a parallel way metal cation are electrodeposited at less negative potential rather than the reduction potential of the cations. The phenomenon is explained by equation (4).

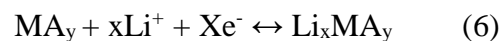


The C represents the H or Pd which are absorbed atoms while M are the catalytic metals, x is for adsorbed atoms, and z for electrons transferred during the reaction.⁹⁹ However,

the applied potential must be lower than the redox potential of the cation. For instance, during the underpotential deposition, potential must be positive with respect to reversible electrode potential. Therefore, an extremely high value specific capacitance is possible. The ability to reverse the kinetics of charging and discharging is crucial in achieving an optimal power density for electrode materials. While, in underpotential deposition technique, the typical working potential window range is 0.3-0.6 V, and capacitive parameters are extremely dependent on the potential window. But the energy density values are very low comparative to few other pseudocapacitive configuration. In pseudocapacitive materials, the electron transfer during a redox reaction As seen in equation 4, these reactions can be explained as electrochemical cation adsorption on the surface of the oxidised species in conjunction with rapid and reversible electron transfer at interface by equation (5).



The C stands for electrolyte cations and z transferred electron. The maximum capacitance that can be achieve by these redox pseudocapacitive devices is approx. $\sim 5000 \text{ F cm}^{-3}$, which is completely depends upon the reactant ions and active site available for reactions. This value of the capacitance is substantially much greater than the 825 F cm^{-3} that is highest theoretical value of capacitance achieved by a EDLC from a surface area of 1 cm^3 carbon.¹⁰⁰ The diffusion of the ions into the crystalline layers the materials also cause pseudocapacitance as displayed by equation (6).



The MA_y is the material e.g., Nb_2O_5 ^{97, 100} with layered structure and intercalation of the ions takes place in the layers. Where, x is the number of the electrons. However, to keep the electric neutrality into the structure of the host material, the intercalation occurs to the valence of the metal. When a cation is intercalated in pseudocapacitor, a particular term is being used to describe the electrochemical behaviour "translational" between supercapacitors and Li-ion batteries.⁹⁷ The main differentiation between these processes lies in the fact that pseudocapacitive intercalation exhibits certain capacitor-like characteristics. Conversely, battery-type materials display restricted ion diffusion, leading to their low power density.

The charge-storage phenomena in intrinsic pseudocapacitance did not depend on morphology and particle sizes. On contrary, when the particle sizes are reduced to

nanosized, battery-type materials showed the pseudocapacitive behaviour due to ion diffusion-controlled properties.⁴⁴ These materials are regarded as extrinsic pseudocapacitive substances. The total charge store by ion intercalation process can be divided into three components: (1) contribution from the Faradaic reaction because of solid-state diffusion of ions, (2) from the surface ion diffusion dynamics known as pseudocapacitance, (3) contribution from the electrostatic charges which can be due to the adsorption and desorption of ions.¹⁰¹ As a result, it is essential to differentiate between the charges that are stored due to capacitive and intercalation of Li-ions. Despite the fact that the mechanism is Faradaic in behaviour in pseudocapacitor while capacitive properties are directly related to working potential window in charge-storage are crucial kinetic features that separate the pseudocapacitive materials from the battery-type. The charge-storage mechanism in pseudocapacitive can be differentiated from the battery-type materials, by investigating the CV at low scan rate depends on the current response which ultimately gave comprehensive understanding of the charge-storage process as can be seen from equation (7).¹⁰²

$$i = av^b \quad (7)$$

The i is the current response at scan rate v , while a and b are constants.

The ion intercalation mechanism has been strictly constrained in battery-type materials. As a result, it is anticipated that the relation between voltametric current, i , and scan rate can be described as equation (8).¹⁰²⁻¹⁰³

$$i = nFAC \cdot D^{1/2} v^{1/2} \left[\frac{\alpha n_a F}{RT} \right]^{1/2} \pi^{1/2} \chi^{(bt)} \quad (8)$$

On comparing the equation 7 and 8, when $b = 1/2$, Cottrell's equation will be confirmed as equation (9).

$$i = av^{1/2} \quad (9)$$

Thus, current response anticipated that the charge-storage in bulk battery-type materials is diffusion-controlled. On the other hand, capacitive current is linearly related to the scan rate, when $b = 1.0$, with the following equation (10).⁶⁷

$$i = vD_d A \quad (10)$$

Where D_d represents the capacitance and charge-storage can be recognised as capacitor like. Wang et al. has used this approach to explain the capacitive contribution from the TiO₂.¹⁰¹ **Figure 1.6(a)** displayed the estimated b values from the CV profiles of the

TiO₂ thin film. Also, the equation 7 is being used to derive the $\log(i) = \log(a) + b \log(v)$, so that the b values at various potential can calculated from the slope of $\log(i)$ vs $\log(v)$, as can be seen from the inset of the **Figure 1.6(a)**. The b obtained is approx. 0.55 at 1.70 V, denotes that the primary source of current will be driven from the intercalation of ions. However, the b values fluctuate between 0.8 and 1.0, demonstrating that ion intercalation pseudocapacitive processes are primarily responsible for charge storage. According to earlier research and CV analysis, it was found that current at fixed potential, is the combination of surface and diffusion-controlled or intercalation.¹⁰⁴ Therefore, it is possible to divide the voltametric current, i , into two halves according to the equation (11).

$$i(V) = k_1v + k_2v^{\frac{1}{2}} \quad (11)$$

On rearranging the equation (12).

$$\frac{i(V)}{v^{1/2}} = k_1v^{1/2} + k_2 \quad (12)$$

k_1v and $k_2v^{1/2}$, refer to current contribution from capacitive and diffusion phenomenon, that is the intercalation/de-intercalation of the ions. K_1 and k_2 calculated from slope and intercept line that results from a plot of $i(V)/v^{1/2}$ vs $v^{1/2}$ at various potentials and various scan rates from CV curves **Figure 1.6(b)**. Moreover, potential range in this situation is from 1.6 and 2.0 V, where the redox reactions can be completely covers.

The area under CV curve shown by gray colour demonstrates the contribution from the capacitive current as seen from **Figure 1.6(c)**. On the other hand, Figure 6d represents the contribution from the capacitive current are 55%, 35%, and 15% for 7, 10, and 30 nm fabricated TiO₂ devices. It is evident that decrease in size contribute more to the capacitive charge than having larger particle sizes. The all pseudocapacitive process presented in the (**Figure 1.4b-d**) are purely due to the different electrochemical mechanisms. Although, the electrochemical features are identical between voltage and fractional coverage (X) of the ions which reacted at electrode surface during the charge-discharge phenomenon.⁴⁴ Pseudocapacitive mechanism could arises only on the surfaces which are 10-100 times bigger than the EDLC processes. Consequently, huge research efforts have been devoted by using pseudocapacitive materials to assemble asymmetric supercapacitor devices that may be redox or pseudocapacitive in nature. It is important to remember that these descriptions are only appropriate for a single

electrode. It is difficult to differentiate whether a Faradaic electrode is a part of a battery-type or a pseudocapacitive process when integrated with a capacitive material. When a battery-type and capacitive electrodes are coupled with each other, the shape of the CV profiles may still be rectangular.

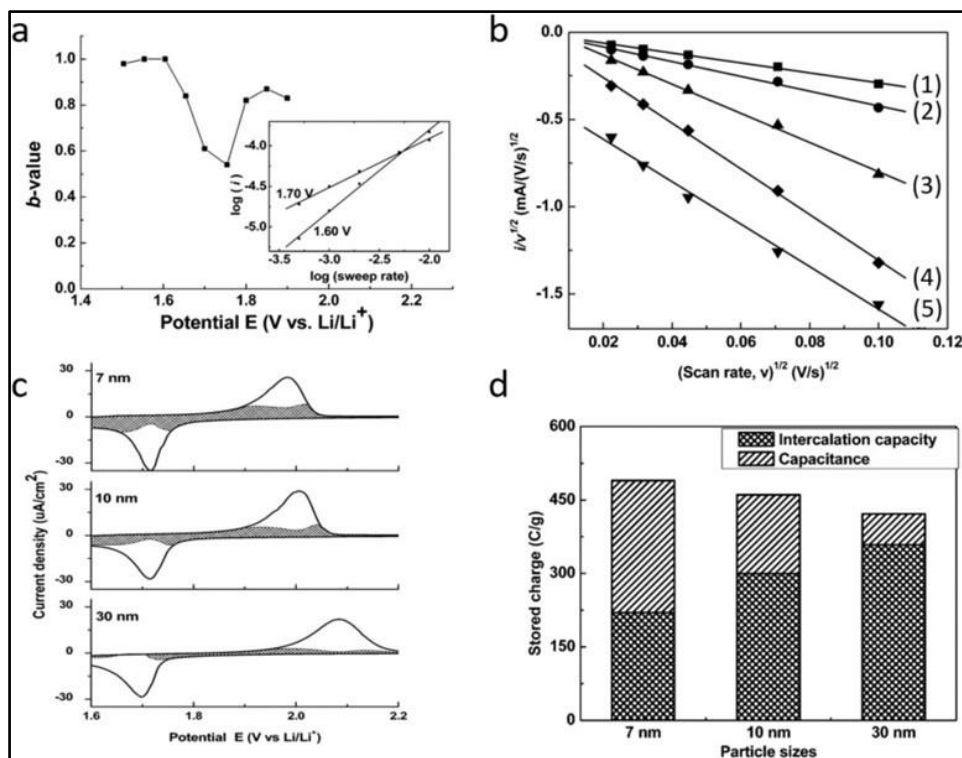


Figure 1.6. Electrochemical energy storage system dependence on materials sizes. (a) The b is evaluated for TiO₂ nanoparticles from CV at various potentials, (b) Plots of $(i/v^{1/2})$ vs $(v^{1/2})$, (c) CV profiles of different electrodes at constant scan rate, (d) Diffusion and surface contribution of different size TiO₂ nanoparticles-based electrodes.¹⁰⁵

1.9. Electrolytes

Three common categories of electrolytes employed in supercapacitors are aqueous, organic, and ionic liquids (ILs). The potential window within which supercapacitors function effectively has been determined based on electrolyte. The electrolyte conductivity and stability are significantly impacted the rate capability and cyclic stability of electrode. Moreover, aqueous electrolyte is categorised into acidic (H₂SO₄), alkaline (NaOH), and neutrals (Na₂SO₄). The main advantages of the aqueous electrolyte compared to others is their high conductivity, inexpensive, easy availability, and non-flammable. The aqueous electrolytic ions are superiors place in the electrochemical devices. Supercapacitors show a higher specific capacitance when an aqueous electrolyte is used. However, there are still some limitations with the voltage

range of water because of the thermodynamic stability window and durability throughout the long-term cell operation. Therefore, additional measures must be required for the selection of the current collector to keep away from corrosion during the choice of the alkali or acidic electrolyte.

Aqueous electrolyte is suitable for high power and large-scale energy-storage devices due to low voltage windows which can offer limited capability to get higher energy densities. The current research has shown that the neutral electrolyte can demonstrate a broad working window range from 1.6 to 1.9 V, which is almost higher than the decomposition voltage of water, 1.23 V.¹⁰⁶⁻¹¹¹ This high voltage results from the OH⁻ ion production potential and hydrogen evolution overpotential that occur when an aqueous electrolyte is used. When the pH is increased, the potential obviously shifts towards lower values clearly be seen by the Nernst equation ($E_{\text{red}} = -0.059 \text{ pH}$). ILs-based supercapacitors have recently been widely available in the market due to their wide working potential windows compared to aqueous electrolytes (often in the range 2.5-2.8).¹¹²⁻¹¹⁵ The wide potential window has a substantial impact on the enhancement of the energy density. Nonaqueous supercapacitors also have the advantage of having a high output voltage in energy storage applications. Moreover, a very high intrinsic cell voltage causes the reduction of the devices required to be aligned in the series. On the other hand, the stable operating potential window of nonaqueous electrolytes is influenced by a variety of factors, including e.g., solvents, conducting salts and impurities, especially the presence of trace water being the most important.

In organic electrolytes, the two most commonly used solvents are acetonitrile (ACN) as well as propylene carbonate (PC). ACN is preferred organic solvent for the researchers because it has a better ability to dissolve the electrolyte salts and has a higher conductivity than other solvents. Unfortunately, the usage of ACN is constrained due to the fact that it is not environmentally friendly and has proved to be hazardous during the battery manufacturing. However, the PC has a number of advantages over ACN including being considerably friendlier and having a larger stable potential window. As a result, strict requirements are made for the selection of organic electrolytes to maintain the level of moisture below 3-5 ppm to avoid the serious performance damages and health issues.¹¹⁶ However, an ionic liquid is salt that has specific melting point at a given temperature. ILs have a low ionic conductivity than that of other electrolytes but still it can be obtained an acceptable value of $\sim 10 \text{ mScm}^{-1}$ and potential window of from 2 to 6 V, particularly 4.5 V. The above-mentioned

characteristics of the ILs make them an ideal choice for electrolyte in supercapacitors. The absence of a solvation shell in IL anticipated that it's a solvent free electrolyte system. Hence, ILs can provide a homogeneous ion size for ion dynamic analyses and EDLCs storage mechanism studies.

Researchers continue to have various inquiries that need to be considered into account using organic or ILs electrolytes for supercapacitors. Organic electrolytes and ILs can be distinguished from the aqueous electrolytes that they have a lower conductivity and a higher viscosity, which resists the diffusion of the ions. The nonaqueous electrolyte shows lower ionic conductivity than aqueous one order of the magnitudes, which results higher internal resistance in supercapacitors. Therefore, specific capacitance of the supercapacitors cannot surpass 200 F g^{-1} and lead to extremely low power density. These supercapacitors are commonly deteriorated due to the high cost and toxicity of the ILs.¹¹⁶ The stability of the electrolyte and electrode is significantly influenced by the applied voltage. Electrode material oxidation and electrolyte decomposition are possible if the applied voltage exceeds the stable potential window. This phenomenon may cause the aging of the electrode components such as electrolyte and active material. In order to avoid such issues, an organic electrolyte extra purification and inert atmosphere to control the contamination from oxygen and moisture so that supercapacitor device can function normally.

1.10. Probing of Thermodynamic and Kinetic for Pseudocapacitive Materials

It is important to investigate the correlation between potential and charge generated because of adsorption/desorption mechanisms by equation (13).^{44, 117}

$$E \approx E^\circ - \frac{RT}{nF} \ln \left[\frac{X}{1-X} \right] \quad (13)$$

All parameters and constants are in accordance with their conventional definitions. Consequently, the potential of electrodes based on pseudocapacitive materials fluctuates during charge-discharge process.

The capacitance can be evaluated at different potential, when E and X are linear with each other, given by the equation (14).⁴⁴

$$C = \left[\frac{nF}{m} \right] \frac{X}{E} \quad (14)$$

In this, m is mass and C can be evaluated from this relation when X is taken to be 1.

The kinetic and thermodynamics of the electrode are equally crucial for the comprehensive study of potential window and electrochemical performance of the pseudocapacitor. As the pseudocapacitance and battery type materials show similar redox reactions, various kinetic processes must be accounted for that cause polarization in battery-type materials as well as in pseudocapacitive materials. During the investigation of supercapacitor electrodes, distinct polarization mechanisms have been observed:¹¹⁷ These polarization phenomena certainly lead to the development of a passivation layer at the interface. Therefore, this passivation layer significantly impacted the specific capacitance and potential window.

Moreover, it's important to note that the crystal structure of materials utilized in electrochemical investigations and the properties of the electrolyte (such as pH or ion composition) exert a significant influence on the working potential window. Particularly, porous materials with substantial surface area, despite being capable of Faradaic processes, may not exhibit the maximum theoretical capacitance. It is widely acknowledged that carbon-based materials display an approximate 1-5% pseudocapacitance, often attributed to the Faradaic reactivity of oxygen functional groups. Similarly, pseudocapacitors display characteristics of both electrical double-layer capacitors (EDLCs) and pseudocapacitance, with about 5-10% of their active interfacial area demonstrating EDLC-like behaviour. As a result, the overall capacitance of supercapacitor materials arises from the combined contribution of both components, EDLCs and pseudocapacitance.

1.11. Transition Metal Oxides for Supercapacitors

Transition metal oxides have gained a massive interest for storage technologies due their sufficient reserves, eco-friendly nature, easy availability, and many other promising properties. Notably, diverse variety of constituents and morphologies, high surface to volume ratio, and elevated specific capacitance make them appealing materials.^{37, 118-119} Also, they can significantly enhance the capacitance by manipulating and controlling their defects and interfaces at the nanoscale level.¹²⁰⁻¹²¹ Although there has been progress in enhancing their energy density, these materials still face several challenges to their practical use. These challenges include limited electrical conductivity, uncontrolled expansion in volume, and slow ion diffusion within the bulk phase.¹²²⁻¹²⁵ The rational design of the metal oxide regarding their composition, fabrication of innovative materials, and enhancement in their electrical conductivity

and oxygen vacancies, has greatly improved the physical and chemical properties of these materials. These advancements have positively affected their electrical conductivity, specific surface area, electroactive sites, and chemical stability. Furthermore, the metal oxide materials exhibit desirable electroactive sites, along with exceptional chemical and high-thermal stabilities, ensuring their ability to deliver high pseudo-capacitive performance and cyclic stability.

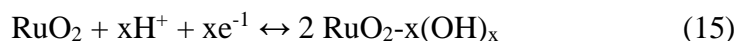
Due to the above-mentioned distinctive properties, the utilization of metal oxides has revolutionized pseudo-supercapacitors and progressive improvement in the energy density at the battery level while preserving the power delivering capabilities of conventional supercapacitors effectively bridges the gap between batteries and capacitors. To overcome the shortcoming of the bulk metal oxide materials, which have lower specific surface area and capacitive performance, there is a rising trend towards the prototype design and manufacturing of porous nanostructures and carbon materials-based energy-storage devices. Therefore, this comprehensive thesis focuses on the recent advancements in metal oxide-based supercapacitors, emphasizing their significance in the development of high-energy-density supercapacitors. The fundamentals of the metal oxide materials and the advancements made in the various types of the supercapacitor devices have been extensively reported. Therefore, recent literature review can provide a valuable insight into this field and future advancement of supercapacitors. The extensively investigated metal oxides for supercapacitors are thoroughly explained here.

1.11.1. RuO₂-Based Supercapacitors

RuO₂ has been extensively studied as a material for supercapacitor electrodes owing to its remarkable properties. These include an elevated voltage range of up to 1.2 V, capability for redox reactions, ability to exist in various oxidation states, exceptional specific capacitance, high conductivity, excellent thermal stability, extended cycle life, metallic conductivity, and impressive capacity to handle high charge/discharge rates.¹²⁶⁻¹²⁷ The RuO₂ electrodes in which the redox pseudocapacitive mechanism can occur, the contribution from the double-layer charging is very minute, around 10%.

Moreover, RuO₂ exhibits pseudocapacitive behaviour in both acidic and alkaline electrolytes, including a variety of distinct redox processes that are sensitive to crystalline forms. For instance, amorphous RuO₂ have a maximum capacitance of 720 F g⁻¹ in H₂SO₄ electrolyte,¹²⁸ while the crystalline form shows a highest capacitance of

710 F g⁻¹ in KOH electrolyte when annealed at 200°C.¹²⁹ The reason for the higher value of capacitance in the acidic medium is due to the fast reversible transfer of the electron by the adsorption of proton on the surface of the RuO₂ nanoparticles, where the conversion of Ru(II) to (IV) takes place as in equation (15).¹³⁰⁻¹³¹



The oxidation state of RuO₂ in alkaline solution is completely different. It is anticipated that when the composite of the ruthenium is charged, it will oxidize to RuO₄²⁻, RuO₄⁻, and RuO₄, and conversely get to reduce to RuO₂, when it is discharged.¹³² The performance of RuO₂-based electrodes not only depend on types of electrolytes, but other factors play a crucial role. The pseudocapacitive nature of the RuO₂ generally arises from the redox reactions occurred at the surface. For this, the large the surface area, the maximum metal sites will be available for redox reactions and the specific will be higher then. Therefore, the increase in the surface is effective to enhance the specific capacitance.¹²⁸ Hence, many attempts have been made, among them the deposition of RuO₂ on a substrate material with a high surface area to make thin film supercapacitor electrodes. These thin films exhibit many micropores for diffusion of ions.¹³³⁻¹³⁵ For instance, electrodeposition of the ruthenium oxide on titanium substrates shows reversible reactions, and superlative power density. The specific capacitance for the thin films reported 786 F g⁻¹.¹³⁴ Moreover, the nanoparticles of the metal prepared by polyol method and homogeneously distributed on carbon surface, results 914 F g⁻¹.¹³⁶ nontubular arrayed electrode was also demonstrate a performance of 1300 F g⁻¹, when hydrous ruthenium oxide being incorporated.⁸⁶

The amount of water present with the ruthenium oxide mainly depends on the synthesis conditions and electrocatalytically formed ruthenium oxide has more hydroxide states which cause additional redox reactions on the surface. Typically, a product dried at room temperature also contains some water content, however the dihydrate and trihydrate can also be achieved changing the conditions.¹³⁷ Another factor that causes the reduction of capacitance is the annealing at higher temperature can result in the evaporation of water molecules.¹³⁸⁻¹³⁹ Reduced diffusion path lengths and enhanced proton transport within the bulk of RuO₂ are supported by the utilization of smaller particle sizes.¹⁴⁰ Among various electrode structures, porous materials exhibit notable benefits, particularly when the pores exhibit a high degree of organization. This well-ordered pore structure help the diffusion of electrolyte ions into the electrodes, thereby

expediting redox reactions within pseudocapacitive electrodes.¹⁴¹ RuO₂ electrodes is significantly influenced by the choice of electrolyte, a critical factor in studying supercapacitor performance. RuO₂ oxide shows electrical-double layer capacitive behaviour in some electrodes “however” in others, it displays pseudocapacitive nature that depended on the loading content of the RuO₂. For instance, capacitance is highly influenced the concentration of KOH is higher than 0.5 M, capacitance increase otherwise decreases. So, the electrolyte concentration should not change in both the Faradaic and non-Faradaic reactions.

Furthermore, ruthenium is an expensive metal, and some efforts are being employed to combine it with other low-cost materials to reduce the cost for electrochemical applications. For example, the SnO₂-RuO₂ system was developed using a wet precipitate method to obtain capacitance of 710 Fg⁻¹.¹²⁹ Takasu et al. has fabricated a system of RuO₂ (33%)–VO₂ (67%)/Ti is much higher than RuO₂/Ti electrode.¹⁴² The incorporation of vanadium not only increases the working potential window but also stability.¹⁴³ Hwang et al. have produced a positive electrode using laser-scribed graphene (LSG) combined with RuO₂ for an asymmetric device, while the negative electrode is composed of activated carbon. The images **Figure 1.7(a)** and **1.7(b)**, showed the successful growth of RuO₂ nanoparticles on graphene flakes. The use of graphene helped to avoid the agglomeration of RuO₂ nanoparticles as well as enable the transportation of the electron. The LSG/RuO₂ electrode shown pseudocapacitive features and store energy due to the quick redox reaction that occurred at the interface of the electrode-electrolyte. The capacity achieved by this fabricated device is 1139 F g⁻¹. The structural representation of the asymmetric device is shown in **Figure 1.7(d)**. However, the CV profiles of positive and negative electrode are displayed in **Figure 1.7(e)**. Also, the optimized asymmetric cell demonstrates a rectangular and capacitive CV profile with a window of 1.8 V as seen in **Figure 1.7(f)**.

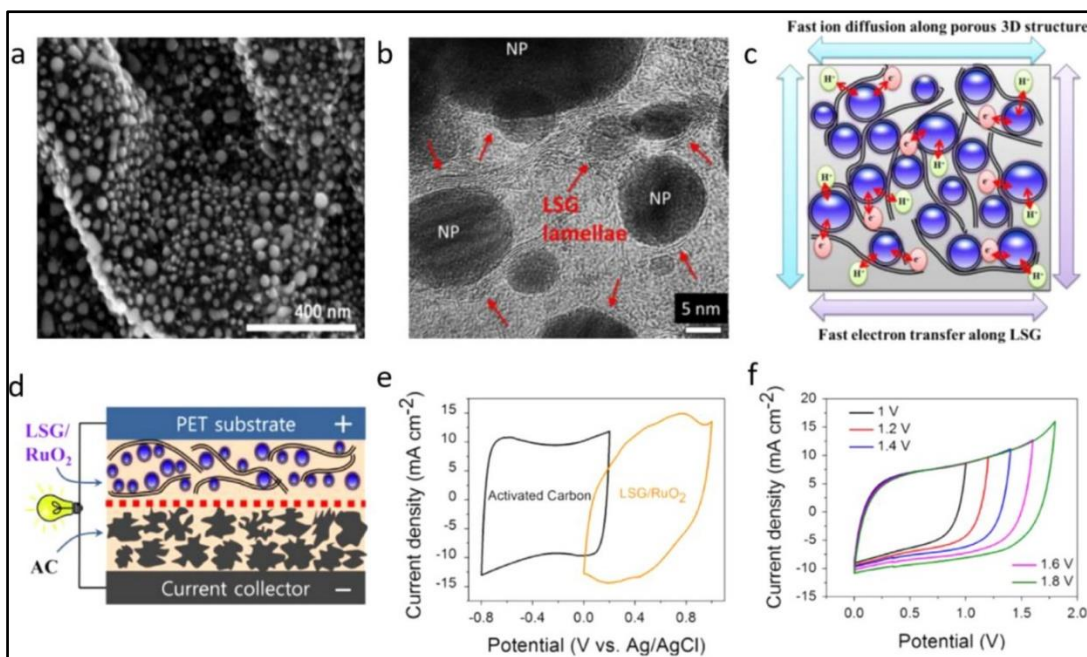


Figure 1.7. (a, b) SEM and TEM micrographs of LSG/RuO₂ system, (c) Graphical illustration of LSG/RuO₂ showing the diffusion phenomenon, (d) Asymmetric electrode fabrication of supercapacitor, (e) CV profiles of both electrodes, (f) CV profiles of device in wide potential window 1.0 to 2.0 V.¹⁴⁴

1.11.2. MnO₂-Based Supercapacitors

Recently, MnO₂ has been deemed to be the most attractive electrode material after ruthenium oxide due to less expensive, easy availability, and highest theoretical capacitance.¹⁴⁵⁻¹⁴⁷ MnO₂ can exist in a variable oxidation states like other transition metal oxide (MnO, Mn₃O₄, Mn₂O₃, MnO₂), and have various crystals forms. Due to a diverse range of crystal structures, structural defects, porosity, morphology, and surface features can make MnO₂ an ideal material for electrochemical applications. On the basis of these structural parameters, lots of research has been devoted to modifying the synthesis of MnO₂ with desire morphology, crystal phase, and defect chemistry to enhance the performance of the supercapacitors.¹⁴⁸⁻¹⁵⁵ The electrical conductivity of thick MnO₂ is lower than that of planar system due to less mass loading. For this reason, loading and incorporation of other transition metals into MnO₂ proved an obvious chemical strategy to improve the conductivity and storage capacity. Therefore, MnO₂ based electrode materials can be modified to elevate the performance by the deposition of Ni, Cu, Fe, V, Co, Mo, Ru,¹³⁸ and doping of the impurity metal Al, Sn, and Pb.¹⁵⁶ The chemical modification had major impact on the enhancement of the parameters

such as rate capability and capacitance. Using porous and highly conductive materials as substrate can improve the electrical conductivity of the MnO₂. The frequently used substrate materials could be carbon nanofoam, porous carbon, graphene, and nanotube assemblies. Among these hybrid systems, the carbon-based substrates are preferred because they provide continuous pathways for ions into the oxide materials.¹⁵⁷ Therefore, many ways have been used to integrate porous carbon with MnO₂ e.g., physical mixing,¹⁵⁸ thermal deposition,¹⁵⁹ chemical deposition,¹⁶⁰ and electrochemical deposition.¹⁶¹ Instead of poor electrical conductivity, a number of other mechanical issues for instance low structural stability, flexibility, and dissolution of electrode active material exist for MnO₂ causing long term cyclability. To overcome the electrochemical dissolution, a growth phenomenon based on electro-polymerization of o-phenylenediamine has been designed.¹⁶² In this process, the polymer coherently coats the nanoscale oxide and acts as a barrier for the electrolyte, which consequently protects the underlying MnO₂ nanoarchitecture from chemical dissolution.¹⁶³ Numerous efforts have been attempted to make MnO₂-polymer composites and their derivatives for supercapacitor electrodes with different morphologies.¹⁶⁴ The electrochemical parameters of the MnO₂-polymer composite system for supercapacitors were improved because of conductivity, stability, and mechanical strength of the used polymers.¹⁶⁴ The supercapacitor's electrodes based on MnO₂ nanostructures can be fabricated using a single component or assembled with the porous carbon and conductive polymers, creating new opportunities for the development of advanced supercapacitors.

Jiang et al. developed an aqueous-based MnO₂ system composed of 2-3 nm nanoflowers having high surface area $\sim 213 \text{ m}^2 \text{ g}^{-1}$ and pore size $\sim 3.6 \text{ nm}$ which was examined by Brunauer–Emmett–Teller (BET) technique.¹⁶⁵ Due to the porous nature of a prepared system and enough space available for smooth movement of the electrolyte ions. In recent times, Shi et al. prepared 2D MnO₂ nanosheets having $\sim 2 \text{ nm}$ thickness by a newly developed template based synthetic protocol.¹⁶⁶ The as-prepared MnO₂ nanosheets and its composite with graphene showed an excellent retention of 90% even over 10000 cycles in aqueous electrolyte. Furthermore, Gao et al. designed a unique architecture in which MnO₂ nanoplates were vertically electrodeposited onto nickel foam to enhance the capacitance.¹⁶⁷ In **Figure 1.8(a)**, the process of fabricating the asymmetric supercapacitor is depicted. Here, the positive electrode is formed by depositing MnO₂ on Ni foam, while the negative electrode consists of graphene hydrogel. The operational potential windows for these electrodes are 0-1.0 V and -1.0-

0 V, as illustrated in **Figure 1.8(b)**. As described, the electrode showed very high energy density 23.2 Whkg^{-1} and cyclic reversibility in a 2.0 V as seen in **Figure 1.8(c)**.

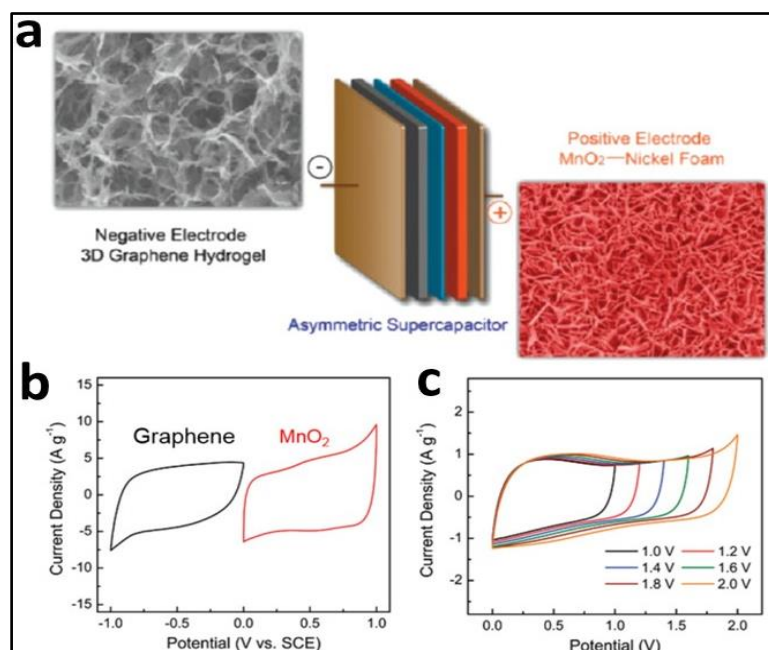


Figure 1.8. (a) Graphical demonstration of graphene hydrogel/MnO₂ based electrode, (b) Comparative CV profiles of graphene hydrogel and MnO₂ in three-electrode configuration, (c) CV profiles of graphene hydrogel/MnO₂ asymmetric device.¹⁶⁸

1.11.3. NiO-Based Supercapacitors

Presently, NiO is considered to be an appealing candidate due to its natural abundance, excellent thermal and chemical stability as well as pseudocapacitive behavior.¹⁶⁹⁻¹⁷⁰ Generally, an oxide material must have the properties for its use in the supercapacitor application e.g., electrically conductive, various oxidation states of the metal, large surface area, and electrolyte ions can intercalate and de-intercalate easily into the crystal structure. The performance of the NiO is usually determined by their redox reactions that occur in the alkaline electrolyte. The main reactions that can be possible for the formation of NiO: the first is that the conversion of NiO and NiOOH, while the second is that NiO converted to Ni(OH)₂ before the reaction between Ni(OH)₂ and NiOOH.¹⁷¹⁻¹⁷⁵ However, both the possibilities are given by equation 16 and 17.



Furthermore, both the reactions elaborate the origin of the oxidation reactions for Ni⁺² to NiOOH by removal of the electron. However, the second possibility is more realistic,

in which combination of NiO with OH⁻¹ ions occur in an alkaline electrolyte. Typically, in “pseudocapacitors” the surface characteristics are crucial in the charge-storage phenomenon.¹⁷⁶ Device efficiency is mainly depends on the surface properties, and therefore researcher are keenly focused to bring improvements in the synthetic techniques and morphological study of the NiO. In this thesis, we have thoroughly studied the morphology, and electrochemical performance of different metal oxide by employing our newly developed synthetic protocols. Although a number of synthetic methods are being used to the synthesis of NiO, the selection of an uncomplicated and eco-friendly protocol is important, which will enhance the surface properties for supercapacitor applications.¹⁷⁷⁻¹⁷⁸

1.11.4. V₂O₅-Based Supercapacitors

Vanadium pentoxide (V₂O₅) is another effectual electrode material for supercapacitor owing a very high energy density and exhibit very high capacitance with more appropriate energy storage mechanism.¹⁷⁹⁻¹⁸¹ V₂O₅ based nanomaterials are promising candidates due to their stable and layered structures, natural abundance, low cost, mixed oxidation sates, quick redox reaction, and broad working potential window.¹⁸² First, decreasing the size on to the nanoscale enhance the performance of the materials because of the lowering in the surface area which ultimately decrease the path length of the electron. Parallel to this, reduction in size create more sites and mitigate electrode material polarization. Second, electrically conductive materials can be added to V₂O₅ as they significantly enhance the electronic transport process. In order to examine the effectiveness of an amorphous V₂O₅, Lee et al. has applied the aqueous solution of KCl as electrolyte to obtain capacitance of 350 F g⁻¹. They anticipated that the K⁺ ions are the reason for the Faradaic reactions that take place in amorphous V₂O₅.^[144] V₂O₅ shows a unique electrochemical behaviour as it produced redox processes.^[145]

Graphene is considered to replace conventional carbon matrixes due to its exceptional features. Hence, the nanocomposite of V₂O₅/graphene composites have numerously used for energy storage. Hydrous V₂O₅ also used to produce thin film by electrochemical deposition in which carbon nanotubes are used as substrate with 3D porous structure to evaluate the supercapacitance. Generally, V₂O₅/nanotubes thin film shows high capacitance at lower scan rate such as 10 mV/s, 910 F g⁻¹ (LiClO₄ in propylene carbonate). The very fine structure of the thin layer may be the reason of electrode's high specific capacitance.^[146] Many reports anticipated that the structure

V_2O_5 plays a pivotal role to the enhancement of energy density e.g., bulk V_2O_5 shows a very lower value of energy density of 11.6 Wh kg^{-1} while a porous nanocomposite of V_2O_5 coated on carbon fibre deliver 45 Wh kg^{-1} .¹⁸³ The performance of V_2O_5 can enhance by an organic electrolyte of high potential window than aqueous electrolyte.¹⁸¹ V_2O_5 nanowires/carbon nanotubes composite demonstrated 65.9 Wh kg^{-1} energy density at power density of 8.32 kW kg^{-1} in bis(trifluoromethanesulfonyl)imide (LiTFSI) electrolyte. As for as our understanding, no study has yet been published a higher value than this and still efforts are being on going to the improvement of energy density for practical applications. Siddheswar Rudra et al. has fabricated a unique architecture of Au- V_2O_5 - MnO_2 which shows excellent specific capacitance 388 F g^{-1} at 1 A g^{-1} and this elevated capacitance of the composite because of synergistic effect produced by each component of the composite as shown in **Figure 1.9**.

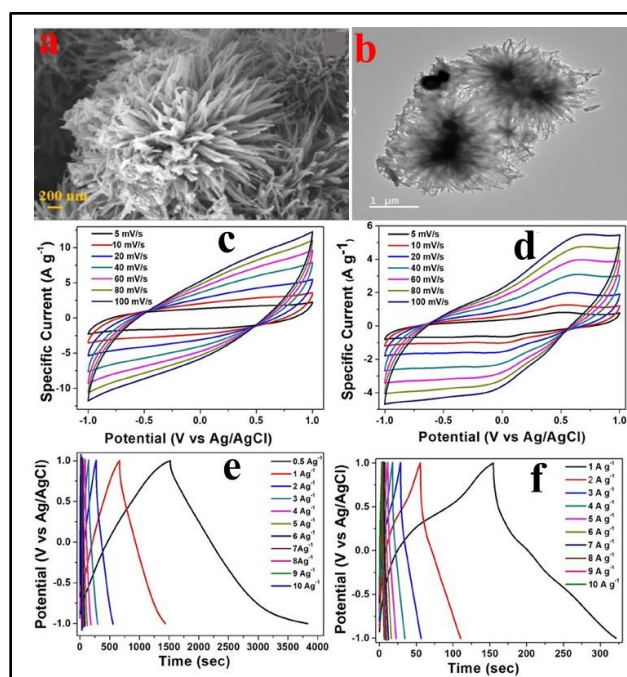


Figure 1.9. (a, b) As synthesized Au- V_2O_5 - MnO_2 nanoflower composites, (c, d) CV profiles of Au- V_2O_5 - MnO_2 and V_2O_5 with respect to potential at various current per gram, (e, f) GCD profiles Au- V_2O_5 - MnO_2 and V_2O_5 .

1.11.5. Ni(OH)₂-Based Supercapacitors

To date, there have been many electrode materials studied and synthesised for electrochemical supercapacitors up to this point. The earlier studies have demonstrated the suitability of conductive polymers, metal hydroxide/oxide, and carbon materials for supercapacitors. The extremely high specific capacitance, non-hazardous nature, low cost, and astonishing redox nature of Ni(OH)₂.^{10, 184-187} Ni(OH)₂ exists in two distinct

forms, namely the α and β phases, with the β -phase being comprised of well-aligned layers of $\text{Ni}(\text{OH})_2$. The appearance of the α - $\text{Ni}(\text{OH})_2$ phase is attributed to the insertion of anions and water molecules between these layers. During charging process, α - $\text{Ni}(\text{OH})_2$ undergoes a transformation into γ - NiOOH . Consequently, in studies of electrochemical activity, the α - $\text{Ni}(\text{OH})_2/\gamma$ - NiOOH combination generates surplus of electrons compared to the β - $\text{Ni}(\text{OH})_2/\beta$ - NiOOH pair. This behaviour, α - $\text{Ni}(\text{OH})_2$ consistently demonstrates superior performance as an electrode material.

Despite having several benefits, α - $\text{Ni}(\text{OH})_2$ synthesis remains an important challenge because of its unstable nature and easy conversion to β -phase. The redox reactions in supercapacitors occur at the interface of the electrode components, for this reason the 3D hierarchical structure usually have less diffusion path length for electrons and ions, which delivered higher specific capacitance. As the redox reactions in supercapacitors are very fast cause the rapid transfer of electrolyte proton in the pores. As a result, these active materials are appealing candidates for electrochemical utilizations. Additionally, the combination of various materials with $\text{Ni}(\text{OH})_2$ has been tried to bring progressiveness with reference to improving the supercapacitor performance. Graphene is an ideal 2D material and usually employed as a substrate for active materials with unique properties e.g., high surface area, excellent stability, amazing mechanical strength.^{173, 188-189} Many researchers have reported the various systems with potential super capacitive behaviour. Yang et al.¹⁹⁰ has grown the α - $\text{Ni}(\text{OH})_2$ at graphene with channel-like porous structure, representing a remarkable performance of 1760.72 F g^{-1} . Zhang et al.¹⁹¹ has also assembled a 3D α - $\text{Ni}(\text{OH})_2$ /graphite system which showed 1956 F g^{-1} at 1 A g^{-1} . The above mentioned studies have made significant improvements to the storage of $\text{Ni}(\text{OH})_2$ by making its composites with carbon material.

1.12. Carbon-Based Materials for Supercapacitors

Presently, carbon-based materials have gained significant interest owing to their abundant availability, stable at high temperatures, excellent electronic conductivity, ease of processing, lack of toxicity, substantial surface area, and robust chemical stability. They always showed rectangular shape of voltammograms which confirmed their suitability for supercapacitors, as see in **Figure 1.10(a, b)**. The galvanostatic charge-discharge profiles are appeared in a triangular symmetrical distribution as in **Figure 1.10(c)**. The accumulation of electric charge at the electrolyte interface occurs via a double layer, and the capacitance is depending on the available surface area for

the diffusion of electrolyte ions. Key factors for the efficient use of carbon-based materials in double layer supercapacitors encompass surface area, conductivity within a porous structure, and the electrolyte's capacity to reach the material's pore regions.

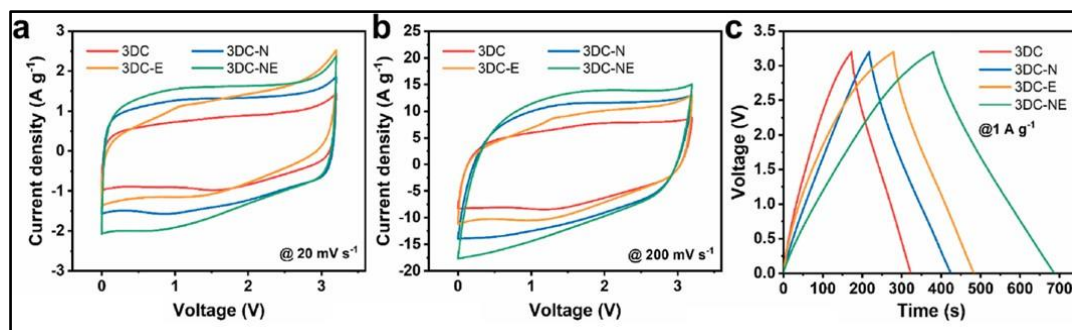


Figure 1.10. (a, b) CV profiles of 3D carbon network, (c) GCD profile at a current density of 1 A g⁻¹.

1.12.1. Graphene-Based Supercapacitors

Graphene is a promising material of 20th century and exist in a hexagonal form. Since Novoselov et al.¹⁹² has synthesized first time the mechanically exfoliated graphene in 2004. Many research efforts have been focused to developed new protocols for the synthesis of graphene materials. Ruoff et Al.⁶⁴ has explored that the exfoliated graphene can be used for EDLCs. During the reduction process graphene single layered starts to agglomerate and size of the particle can vary from 15 to 25 nm and surface area is (705 m² g⁻¹) which greatly influenced the performance of the supercapacitors. In aqueous an organic electrolyte graphene showed 135 and 99 F g⁻¹, respectively. To avoid the agglomeration of graphene layers, chemical vapour deposition (CVD) and hydrothermal methods are useful methods.

1.12.2. Graphene Nanosheets Based Supercapacitors

Graphene sheets represent a distinct form of carbon material capable of energy storage in the form of EDLCs with a capacity of up to 550 F g⁻¹. Over time, numerous synthetic techniques have been reported in literature. These methods encompass procedures like graphite exfoliation,¹⁹² carbon nanotube unzipping,¹⁹³ reduction from graphene oxide (GO),¹⁹⁴ solvothermal synthesis,¹⁹⁵ epitaxial growth on SiC surfaces,¹⁹⁶ epitaxial growth and CVD growth of graphene on matched substrate,¹⁹⁷ bottom-up organic synthesis.¹⁹⁸ Presently, Taghioskoui,¹⁹⁹ has compiled various synthetic methods. The main problem facing the research community related to the preparation of graphene is the stabilization of single sheet. This concern involves maintaining the

fundamental chemical and physical properties intact during exfoliation, whether in presence or absence of polymeric and surfactant dispersions. Herein, we will explain in detail the mechanical and chemical exfoliation of the graphene.

Geim et al.¹⁹² has also prepared exfoliated single-layer graphene by applying pressure to the opposite side of the substrate while using a scotch tape to break off the graphene layers from graphite using a micromechanical cleavage approach. The tape is removed in the final step, resulting in a single-layer graphene of substantially higher quality than that obtained by traditional methods. However, this method has a few drawbacks, including the inability to produce graphene on large amount due to the huge labour work and the lengthy processing time. Chen et al. have put a lot of effort into overcoming these limitations by developing a novel mechanical exfoliated method **Figure 1.11**.²⁰⁰ They used three-roll mill equipment, which is commonly available in the rubber industry for the conversion of graphite to graphene. Selecting the correct types of polymeric adhesives, this approach may be widely used to manufacture graphene-polymer composites by adjusting rolling time, temperature, and rolling speed.

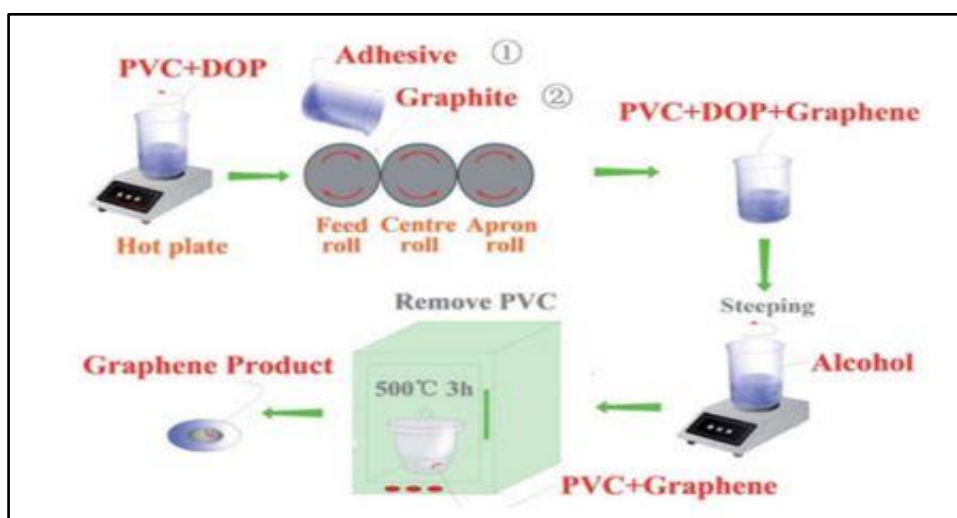


Figure 1.11. Schematic illustration for the exfoliation of the graphene.²⁰⁰

On the other hand, the low output of the mechanical exfoliated method caused its limitations in the supercapacitor's applications. Therefore, a new design of an alternative approach which yield a high mass production is desired. As an alternative to the exfoliation, the chemical technique is a more scalable and optimal process for the production of graphene in which graphite is oxidised to GO by Hummers or modified Hummer's as illustrated in **Figure 1.12**. The as-prepared GO was reduced to graphene using some reducing agent especially hydrazine solution. Furthermore, the GO can also

be employed for preparation of graphene nanosheets.²⁰¹ The large-size graphene can also be produced from modified Hummer's method using a very simple wet chemical synthesis. First, graphite oxide was made by oxidising it with a strong oxidant (KMnO_4 , P_2O_5 , etc.) and then reduced by using a reducing agent such as hydrazine hydrate,²⁰² NaBH_4 ,²⁰³ urea,²⁰⁴ UV light,²⁰⁵ and laser.⁶⁶

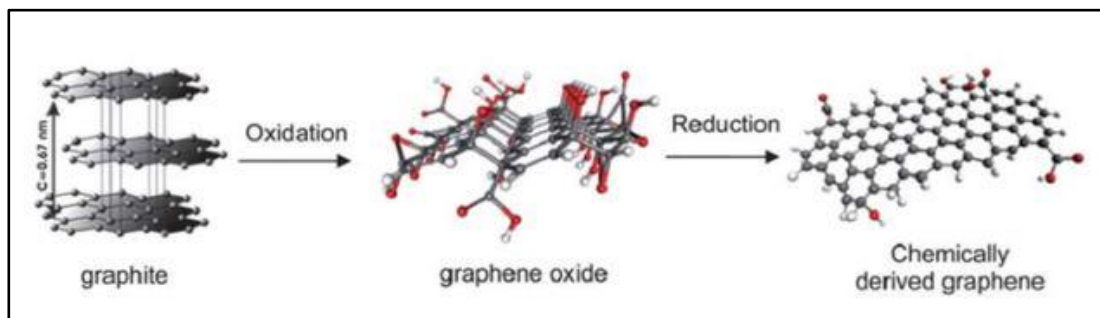


Figure 1.12. Graphical representation for the synthesis of chemically produced graphene.¹⁹⁴

The capacitance of individual graphene layer is calculated $\sim 21 \text{ mF cm}^{-2}$ and theoretical value in EDLCS could be $\sim 550 \text{ F g}^{-1}$.²⁰⁶ These values are still not encouraging comparative to theoretical values. In the previous work, the specific capacitance of chemically produced graphene in aqueous KOH and organic electrolyte was measured to be 130 and 99 F g^{-1} .⁶⁴ However, the values reported for the derivatives of graphene obtained from hydrazine via GO reduction are substantially lower than expected i.e., $\sim 200 \text{ F g}^{-1}$ in aqueous electrolyte,²⁰⁷ $\sim 120 \text{ F g}^{-1}$ in an organic electrolyte,²⁰⁸ and $\sim 75 \text{ F g}^{-1}$ in an ionic liquid.²⁰⁹ The aggregation phenomenon occurred in graphene layers is due to the π - π interactions. As the aggregation decreased the surface area which has results in reduction of the specific capacitance. Furthermore, the graphene's high conductivity also severely affected due to the inter-sheet's resistance. To avoid from these issues various strategies have been employed.²¹⁰ The intercalation of highly hard materials, polymers, and nanoparticles is one of them. In contrary, solvated graphene sheets that utilised water as a helpful separator abled to capacitance of 156.5 F g^{-1} .²¹⁰ The curved graphene supercapacitors showed very impressive energy density in comparison to Ni metal hydride battery, 136 Wh kg^{-1} at $80 \text{ }^\circ\text{C}$ at 1 A g^{-1} .²¹¹

It was also found that the N-doped rGO based electrode assembled by plasma process have very low resistivity as well as good conductivity and demonstrate higher capacitance than pure rGO.²¹² However, doping has no worse effect on the other parameters of the supercapacitors such as cyclic stability and compatibility with the

substrate. Doping with nitrogen is thought to be that atom enter into the rGO basal planes, increasing the binding energy and allowing the adjustment of additional electrolyte ions on the electrode surface. Flexible supercapacitors were also be fabricate by combination of polymers with graphene e.g., graphene/polyaniline system.²¹³ For instance, polyaniline (PANI)/ graphene system have capacitance of 970 F g⁻¹.²¹⁴ Chemical vapour deposition (CVD) was recently used to develop porous three-dimensional graphene networks (3DGNs).²¹⁵ NiO nanoparticles were grown on porous 3D GNs, which proved helpful to avoid the aggregation of the material during the GCD analysis. On a parallel fashion, 3DGNs provides a smooth channel for flow of charges and showed 816 and 573 F g⁻¹ determined from CV, respectively.²¹⁶

1.13. Techniques Used for the Analysis of Supercapacitors

The electrochemical behaviour of the materials is investigated by various electrochemical techniques including CV, GCD and EIS, respectively.

1.13.1. Cyclic Voltammetry (CV)

Typically, CV measurements are conducted within a system consisting of a three-electrode configuration. Capacitance values are evaluated in different electrolytes, ranging from acidic to alkaline, considering the operational potential window and various scan rates. The specific capacitance is determined using equation (18).

$$C_{sp} = \frac{\int IdV}{2km\Delta V} \quad (18)$$

Where C_{sp} refers to the specific capacitance (F g⁻¹), K represents scan rate mV s⁻¹, $\int IdV$ s area under the CV curve, I used for discharge current, m is mass (g), Δt indicates discharge time (s) and ΔV for potential window (V). The research conducted by Binglin Guo et sl. involved the synthesis of composites Ni(OH)₂-rGO. These samples were coded by GN1, GN2, GN5, and GN10. The nomenclature reflects the varying mass ratios of GO and Ni(OH)₂, specifically in the proportions 1:1, 1:2, 1:5, and 1:10. The CV profiles for each of these samples are depicted in **Figure 1.13**.

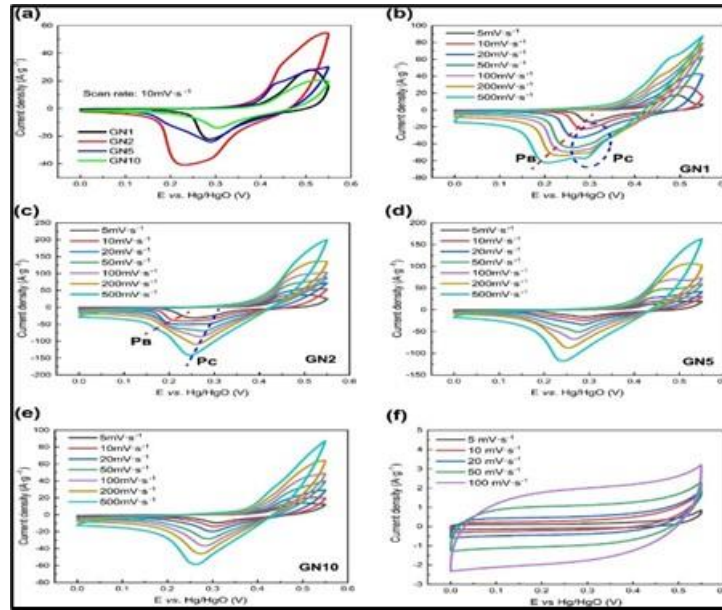


Figure 1.13. (a) CV profiles, (b-e) CV profiles of GN1, GN2, GN5, and GN10 at various scan rates, (f) CV profiles of rGO at various scan rates.²¹⁷

1.13.2. Galvanostatic Charge-discharge (GCD)

Chronopotentiometry was applied to carry out GCD behaviour in a supporting electrolyte at a specific working potential window at a certain current density. It can be observed from charge/discharge curves that charging and discharging curves usually show similar behaviour except from the initial charging time. The specific capacitance calculated from GCD by equation (19).

$$C_{sp} = \frac{I\Delta t}{m\Delta V} \quad (19)$$

However, specific capacitance for symmetric device evaluated by equation (20).

$$C_{sp} = 2 \frac{I\Delta t}{m\Delta V} \quad (20)$$

The GN2 with respective specific capacities in mAh g⁻¹, and different electrodes at constant current density are displayed in **Figure 1.14(a, b)**.

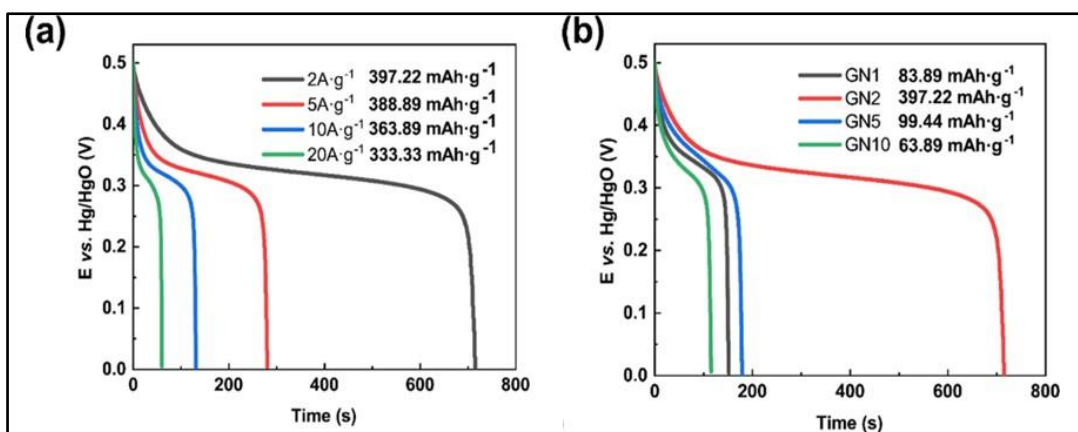


Figure 1.14. (a) GCD profiles of potential candidate GN2, (b) GCD analysis of GN1, GN2, GN5, and GN10 at 2 A g⁻¹.²¹⁷

The specific capacitance evaluated from both CV and GCD measurements are considerable reliable. Nevertheless, a significant reduction in power and capacity possibly attributed to the minor difference in potential at the initiation of the discharge curve as because of IR drop after each half-cycle.

1.13.3. Electrochemical Impedance Spectroscopy (EIS)

EIS stands a technique utilized for assessing the electrochemical performance of electrode materials at their open circuit potential. By utilizing an acidic or alkaline medium at both lower and higher frequency ranges, the Nyquist plots are generated. These plots depict the relationship between imaginary impedance (Z_{im}) and real impedance (Z_{re}). Notably, in the high-frequency region, an evident semicircle manifests, while a linear trend is observable in the lower frequency region for each of the Ni(OH)₂-rGO composite samples, illustrated in **Figure 1.15(a, b, c, d)**. The R_{ct} denotes the charge transfer resistance and evaluated from semicircle of the plots. Furthermore, the specific capacitance can also be calculated based on the semicircle region. The plot drawn through an angle of 45° relate to the Warburg impedance and anticipates the fast ion diffusion resistance. When high frequency resistance applied to the open circuit cause to increase the value of the effective series resistance (ESR) and electrode material resistance. Hence, the specific capacitance got to a highest value.

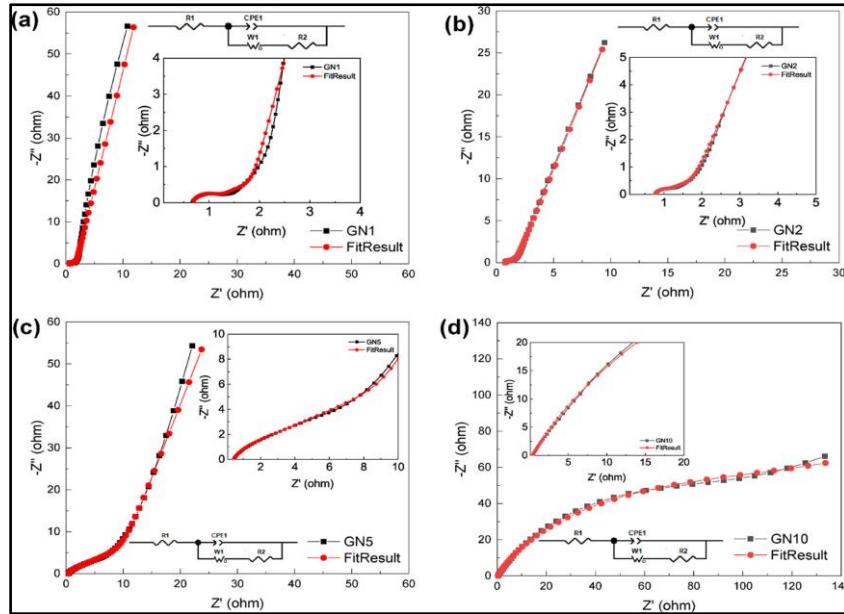


Figure 1.15. Nyquist plots with corresponding fitting data of given samples at open circuit voltage.²¹⁷

1.14. Parameters of Supercapacitors

1.14.1. Coulombic Efficiency

It is the ratio of discharge and charge time, which can be measure using the equation (21).

$$\eta = \frac{t_d}{t_c} \times 100\% \quad (21)$$

Here, η is coulombic efficiency, t_d discharge and t_c is charge time(s). Sachin Pundir et al. assembled a system which composed of 1D β - MnO_2 nanowires which was tested for cyclic stability test for 5000 cycles. After 5000 cycles, fabricated system maintained the coulombic efficiency of >98% with excellent cyclic stability of 97.5% as shown in **Figure 1.16.**

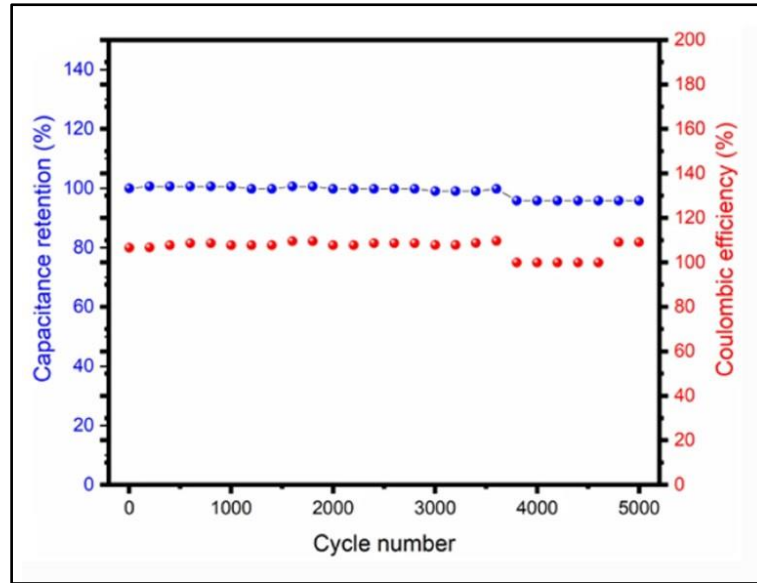


Figure 1.16. Capacitance retention and coulombic efficiency of 1D β -MnO₂ nanowires in aqueous electrolyte.²¹⁸

1.14.2. Power density (P) and Energy density (E)

Power and energy densities of supercapacitors are frequently measured from a well-known charge-discharge method. Additionally, both have an inverse relationship with each other and are effective tools for electrochemical study. Both the parameters have great importance to the estimation of electrode performance. E in Wh kg⁻¹ and P in W kg⁻¹ of the fabricated electrode materials were calculated using equations 22 and 23, respectively.

$$E = \frac{C_{sp} \times \Delta V^2}{2 \times 3.6} \quad (22)$$

$$P = \frac{E \times 3600}{\Delta t} \quad (23)$$

1.15. Important Synthetic Methods of Nanomaterials

The biggest challenge facing the field of nanoscience is the synthesis of nanomaterials with desired morphology and composition. The primary goal is to fabricate the state-of-the-art nanomaterials so that their physical and chemical properties can be fully exploited. As a result, numerous methods have been explored in the literature including thermal evaporation²¹⁹⁻²³², metal organic and chemical vapour deposition,²³³⁻²³⁷ hydrothermal or solvothermal synthesis²³⁸⁻²⁴³, template-based synthesis etc. These methods can be categorized into template-based and spontaneous.

In template-based synthesis, materials are grown using a certain template while in spontaneous the crystal structure and surface characteristics are changed in a particular way. The spontaneous technique is additionally split into three categories: dissolution-condensation, evaporation-condensation, and vapour liquid solid development (VLS). Generally, two approaches have been intensively employed to the synthesis of nanomaterials: top-down and bottom-up. In top-down strategy, the nanosized particles are prepared by using physical methods such as photolithography, slicing or sequential cutting of bulk materials while bottom-up approach involves the physical and chemical synthesis of nanomaterials in which materials are attached with each other from bottom to top e.g., atom to atom, molecules to molecules and cluster to cluster. Bottom-up approach is the best way for the large scale production of the electronic devices and 3D architectures because it provides noncovalent intermolecular interaction between the molecules to fabricate the structures at nanoscale.²⁴⁴⁻²⁴⁵ The biggest challenge faced by the semiconductor industry is to process the materials in solution phase and bottom-up approach seems to be a promising solution of this problem.²⁴⁶ Milling is an example of top-down method for the synthesis of the nanomaterials while colloidal synthesis anticipate the bottom-up approach.²⁴⁷⁻²⁴⁸ Hence, both the techniques have key importance in the field of nanotechnology. In the literature, a variety of experimental procedures have been investigated, but we have chosen solution phase growth methods:

- 1) Hydrothermal or solvothermal method
- 2) Hot-injection method

1.15.1. Hydrothermal or Solvothermal Method

For decades, researcher is using hydrothermal method for the synthesis of inorganic materials. The hydrothermal techniques applied for heterogeneous reactions that contains aqueous solvent at elevated temperature and under pressure to dissolve and recrystallize the materials which are not soluble at room temperature.²⁴⁹ The hydrothermal synthesis is carried out in an autoclave which have steel lined vessel and all the precursors are added into it with the water. The desired temperature is maintained to dissolve the nutrient from the opposite end of the growth chamber while the other end is responsible for further growth. The method was developed by the geologist in the middle of the 19th century and promoted by gradually to understand the formation of minerals at high temperature and pressure. The research associated with laboratory simulation have assisted the researchers to figure out the complicated phenomena such as exitance of rocks etc. In the 20th century, it was clearly anticipated that hydrothermal

technique is a key tool for material synthesis, especially in the area of hydrometallurgy and crystal formation. The commercial importance and viability of the hydrothermal method can be estimated that the sodium hydroxide has been successfully synthesized from leach bauxite, quartz crystals and zeolite etc. In recent years, hydrothermal method is essential in many areas of the science due to controlled reaction conditions as well as less chances of contamination. One of the main benefits of hydrothermal synthesis is the capacity to direct formation of the anhydrous, crystalline, and amorphous powders from solution phase. It can also control the shape, size, chemical composition, and stoichiometry of the materials. Most importantly, the powders are extremely reactive in sintering, in many situations no need of the calcination and milling process. Despite its many advantages, hydrothermal synthesis has a few drawbacks, such as high-cost equipment and the difficulty to monitor reaction progress. Currently, numerous efforts have been focused on the development of environmentally friendly materials due to the growing awareness of the health and safety. Furthermore, the processing methods for the fabrication, treatment, reuse, and recycling of the materials must be controlled and eco-friendly. Therefore, hydrothermal method stands apart in the contemporary science.

1.15.2. Hot-Injection Method

Currently, colloidal quantum dots (CQDs) are synthesized employing a method proposed by LaMer and Dinegar, described the rapid synthesis of monodisperse particle by nucleation and fast growth of the existence nuclei. Alivisatos and Bawendi et al. developed a new protocol "hot injection" for the synthesis monodisperse CdS, CdSe, and CdTe QDs using this method. In this approach, an organometallic reagent is rapidly injected into a hot high boiling solvent to produce homogeneous nuclei. To avoid the agglomeration of the nanocrystals an organic ligand was also added in the solution before the addition of reagent. For instance, the ligands that are usually used e.g., trioctylphosphine oxide, trioctylphosphine oxide, oleic acid, and oleylamine. After nucleation, the growth of nanocrystals observed in the solution with the larger particles growing more slowly than smaller. Ostwald ripening happens as the growth progresses in which smaller nanocrystals are dissolved by the larger nanocrystals. Therefore, the average size of the particle increases though the concentration of the particle decreases before reaching to the saturation point. Hot injection approach is useful as it provides fully control over the shape and size during the growth stage. Hence, nanocrystals of

different sizes can easily be obtained from this approach by adjusting the temperature, surfactant content, and reaction time.

1.16. Aims and Objectives

1.16.1. Aims

- The study of β -Ni(OH)₂ and NiO nanoparticles on rGO substrates as high-performance active layer for advanced supercapacitors.
- To explore the influence of Ag nanoparticles on N and S co-doped TiO₂ for battery-type Supercapacitor Application
- To investigate the electrochemical performance of as-synthesized α -Ni(OH)₂, NiO, MnO₂, and α -Ni(OH)₂-MnO₂ nanomaterials for battery-type supercapacitors.
- To investigate the super-capacitive performance of V₂O₅ based nanomaterials synthesized by unique molecular precursor route and its composites with GO and rGO substrates.

1.16.2. Objectives

- To perform in-situ synthesis of β -Ni(OH)₂ and NiO nanoparticles on graphene substrate by hydrothermal method.
- To investigate the β -Ni(OH)₂/rGO as precursor for the synthesis of NiO/rGO nanocomposites
- To the synthesis of heteroatom (N, S) co-doped TiO₂ decorated with Ag nanoparticles using a direct combustion approach.
- To design of a new synthetic protocol for the synthesis of spherical nanoparticles of α -Ni(OH)₂, NiO, MnO₂, and α -Ni(OH)₂-MnO₂ hybrid, employing the polar, aprotic solvent, Dimethylformamide (DMF).
- Colloidal synthesis of V₂O₅ nanoparticles using a single starting material from molecular precursor route in simple and efficient way.
- To comprehensively characterize all the synthesized nanomaterials using P-XRD, Raman spectroscopy, XPS, (TEM and SEM respectively), TGA and DSC.

2.1. Chemicals

All chemicals were analytical grade and used as received. The nickel acetate ($\text{Ni}(\text{OCOCH}_3)_2$, $\geq 98\%$), CTAB ($\text{C}_{19}\text{H}_{42}\text{BrN}$, $\geq 99\%$), urea ($\text{CH}_4\text{N}_2\text{O}$, $\geq 99\%$), deionized water, graphite powder (C, $\geq 99.9\%$), sodium nitrate (NaNO_3 , $\geq 99.9\%$), potassium permanganate (KMnO_4 , $\geq 99.9\%$), hydrochloric acid (HCl, 37%), sulfuric acid (H_2SO_4 , $\geq 98\%$), hydrogen peroxide (H_2O_2 , 30%), thiourea (NH_2CSNH_2 , $\geq 99.0\%$), titanium (II) oxide (TiO_2 powder, $\geq 99.8\%$), silver nitrate (AgNO_3 , $\geq 99.0\%$), (NaBH_4 , $\geq 99\%$), nickel(II) sulphate heptahydrate, ($\text{NiSO}_4 \cdot 7\text{H}_2\text{O}$, $\geq 99.9\%$), sodium hydroxide (NaOH, $\geq 98.0\%$), dimethylformamide (DMF, $\geq 99.8\%$), manganese(II) nitrate tetrahydrate ($\text{Mn}(\text{NO}_3)_2 \cdot 4\text{H}_2\text{O}$, $\geq 97.0\%$), sodium dodecyl benzene sulphonate (SDBS, technical grade) and potassium permanganate (KMnO_4 , $\geq 99.0\%$), oleylamine ($\text{C}_{18}\text{H}_{37}\text{N}$, $\geq 98\%$), vanadium (III) acetylacetonate ($\text{V}(\text{C}_5\text{H}_7\text{O}_2)_3$, $\geq 98\%$), 1-Octadecene ($\text{CH}_3(\text{CH}_2)_{15}\text{CH}=\text{CH}_2$, $\geq 99.0\%$), acetone (CH_3COCH_3 , $\geq 99.5\%$), methanol (CH_3OH , $\geq 99.8\%$), polyvinylidene fluoride (PVDF) $\{(\text{CH}_2\text{CF}_2)_n$, $\geq 99.0\%\}$, N-methyl-2-pyrrolidone (NMP) $\{\text{C}_5\text{H}_9\text{NO}$, $\geq 99.0\%\}$, carbon black (C, $\geq 95\%$), potassium hydroxide (KOH, $\geq 98\%$).

2.2. Material Synthesis

2.2.1. Synthesis of $\text{Ni}(\text{OH})_2$ and NiO Nanoparticles Supported on rGO

$\text{Ni}(\text{OH})_2$ nanoparticles were synthesized by direct hydrothermal technique. For this, a mixture of 30 mL of deionized water, 0.8 g of nickel acetate, 0.4 g of CTAB and 0.3 g of urea were stirred in a beaker for 0.5 h. Then, the mixture was added into an autoclave and maintained at 120 °C for 12 h. The resulting product was centrifuged and washed to obtain $\text{Ni}(\text{OH})_2$ nanoparticles. In the meantime, the same method described above was used to prepare $\text{Ni}(\text{OH})_2/\text{rGO}$ nanocomposite, with the exception that 15 mL of water was used along with a 15 mL of rGO, where the concentration of rGO was kept at 0.5 mL^{-1} .²⁵⁰ The NiO/rGO nanocomposite was also obtained by the same method after the annealing of $\text{Ni}(\text{OH})_2/\text{rGO}$ at 400 °C. Reduced graphene oxide was obtained by thermal annealing of the graphene oxide at 200 °C.²⁵¹

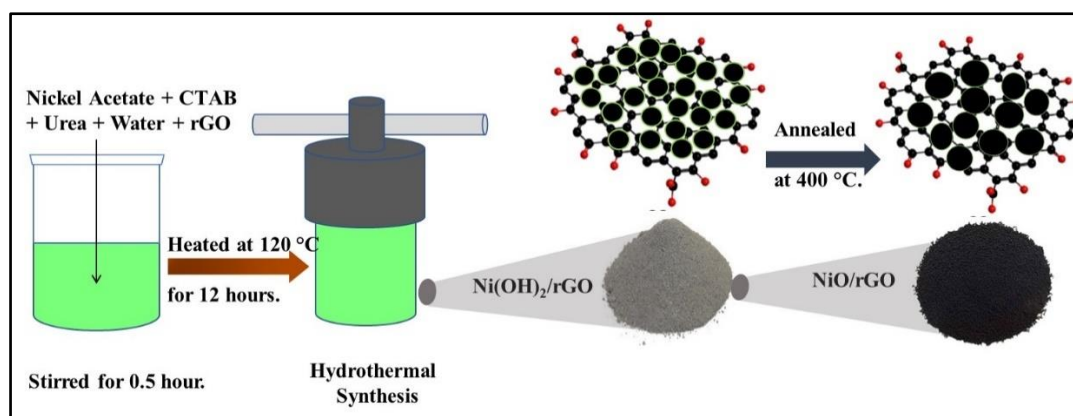


Figure 2.1. Schematic Illustration of Ni(OH)₂ and NiO nanoparticles grown on rGO by direct hydrothermal approach.

2.2.2. Synthesis of Ag/N,S co-doped TiO₂ Nanocomposite

In a typical synthesis of N, S co-doped TiO₂, a mixture of TiO₂ and thiourea with mass ratio of 1:1 was mixed in a ceramic dish and ground for 30 minutes to make a homogeneous fine powder. Then, the powder was heated at 400 °C for 1 hour. The obtained mixture is N, S co-doped TiO₂ nanoparticles with pale-yellow color. The nanoparticles were further decorated by Ag nanoparticles by reduction of the metal. For this 0.5 g of an aqueous AgNO₃ solution was mixed to 5% by weight of N, S co-doped TiO₂ and after that NaBH₄ aqueous solution added dropwise to reduce Ag metal to obtained Ag/N,S co-doped TiO₂ nanocomposite.

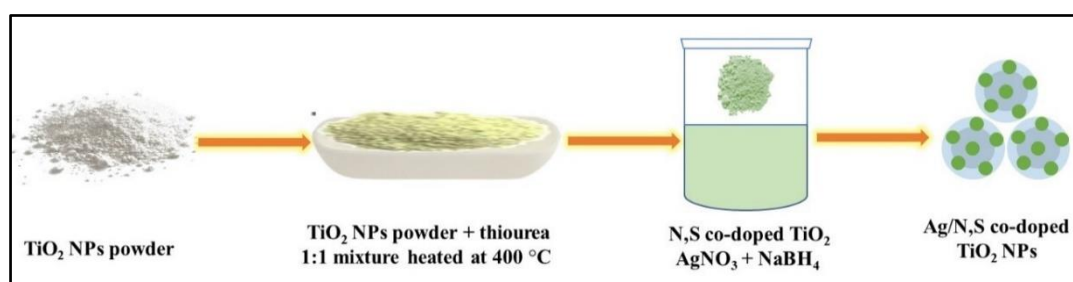


Figure 2.2. Illustration of Ag/N,S co-doped TiO₂ nanocomposite synthesis.

2.2.3. Synthesis of α -Ni(OH)₂ and NiO Nanoparticles

In the synthesis of α -Ni(OH)₂ nanoparticles, a mixture of NiSO₄·7H₂O (2.75 g, 9.8 mmol) and NaOH (0.132 g, 3.3 mmol) in 40 mL of DMF were degassed under vacuum and with vigorous stirring at 60 °C for 1 hr. Then maintained at 120 °C for 24 hrs. Subsequently, the reaction mixture was centrifuged at 6000 rpm for 5 minutes which resulted in the separation of a green paste-like precipitate. The green paste was dried in an oven at 60 °C for 12 hrs which yielded a green crystalline powder, identified

as α -Ni(OH)₂. Nanoparticles of NiO were obtained directly, by annealing at 500 °C for 2 hrs in a furnace.

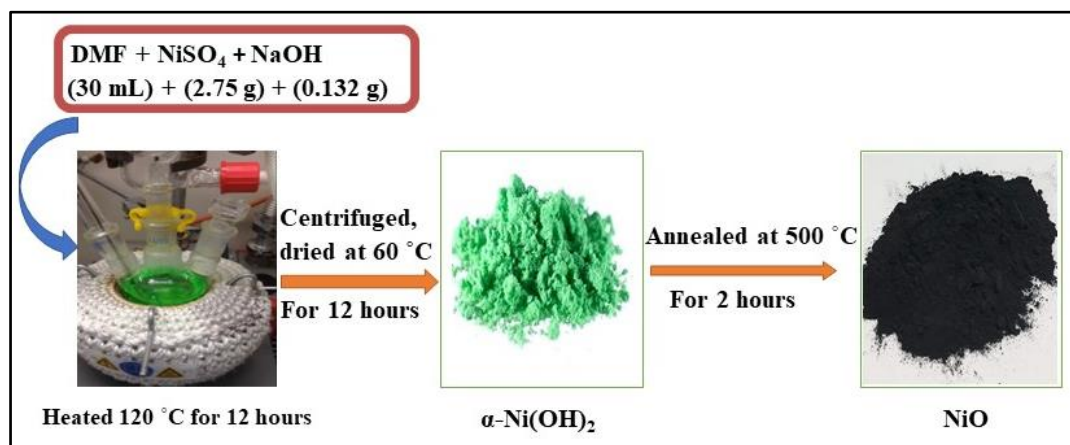


Figure 2.3. Schematic illustration for the synthesis of α -Ni(OH)₂ and NiO nanoparticles.

2.2.4. Synthesis of MnO₂ Nanoparticles

In a typical synthesis of MnO₂ nanoparticles, Mn(NO₃)₂·4H₂O (0.2685 g, 1.07 mmol) and sodium dodecyl benzene sulfonate (SDBS, 0.3845 g, 1.1 mmol) were dissolved in 30 mL of DMF in a 50 mL three necked, round-bottomed flask. When the solution turned clear, 5 mL of 0.2 M aqueous KMnO₄ was added, and the mixture was degassed under vacuum for 30 minutes at room temperature while continuously stirring. The temperature of the resulting solution was then maintained at 150 °C for 6 hrs and subsequently allowed to cool down to room temperature naturally and dried at 60 °C for 6 hrs.

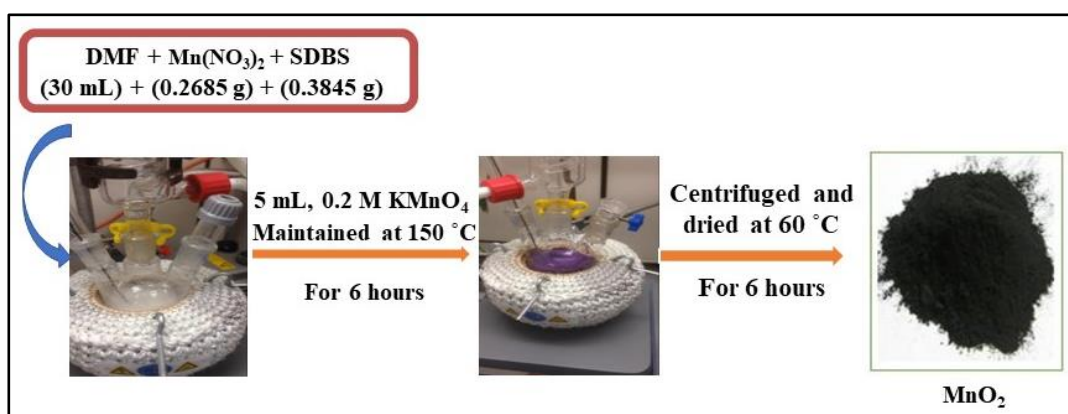


Figure 2.4. Schematic illustration for the synthesis of MnO₂ nanoparticles.

2.2.5. Synthesis of α -Ni(OH)₂-MnO₂ Hybrid Nanocomposite

The α -Ni(OH)₂-MnO₂ hybrid nanostructures, 50 mg of the above synthesized Ni(OH)₂ nanoparticles were placed in a 50 mL three necked, round-bottomed flask and dispersed in 30 mL of DMF. Then, 10 mL of 0.08 M KMnO₄, prepared in DMF, was added to the suspension and the mixture was degassed under vacuum. The solution was kept under constant stirring for 3 hrs. The temperature of the mixed solution was then maintained at 150 °C for 5 hrs and centrifuged at 6000 rpm for 5 minutes as well as dried at 60 °C for 6 hrs.

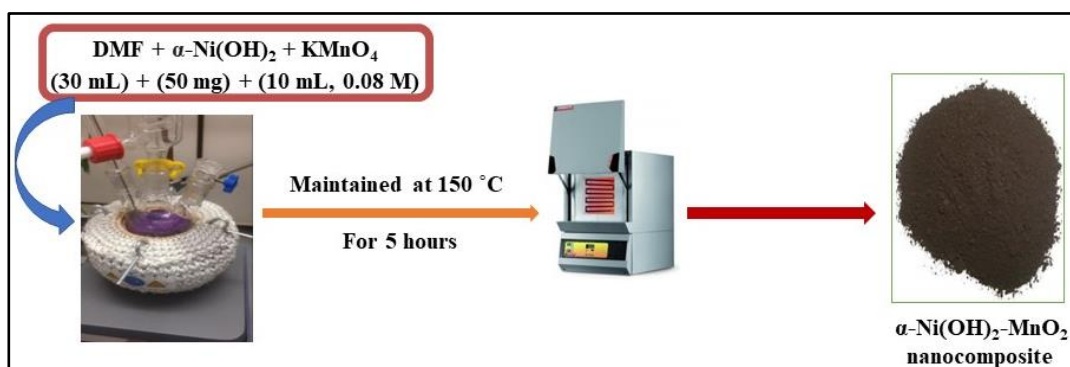


Figure 2.5. Schematic illustration for the synthesis of α -Ni(OH)₂-MnO₂ nanocomposite.

2.2.6. Synthesis of V₂O₅ Nanoparticles, V₂O₅/GO, and V₂O₅/rGO Nanocomposites

V₂O₅ nanoparticles were synthesized by using a colloidal synthetic route. Initially, 6 ml of oleylamine heated to 200 °C in a three necked, round-bottom flask. Subsequently, 0.3 g of vanadium (III) acetylacetonate which was sonicated in 3 ml of 1-octadecne (ODE), injected to heated oleylamine. The temperature of the reaction mixture decreased approximately 15-20 °C upon injection. The temperature was maintained to 200 °C for 1 hour and centrifuged at 6000 rpm for 5 minutes which resulted in the separation of a black precipitates. The precipitates were dried product was calcined at 500 °C for 2 hrs to obtain V₂O₅ nanoparticle and colour was changed from black to yellowish-brown. The composite of pre-synthesized V₂O₅ nanoparticles with GO and rGO were prepared by sonicating in a weight ratio of ~7:3 in water.

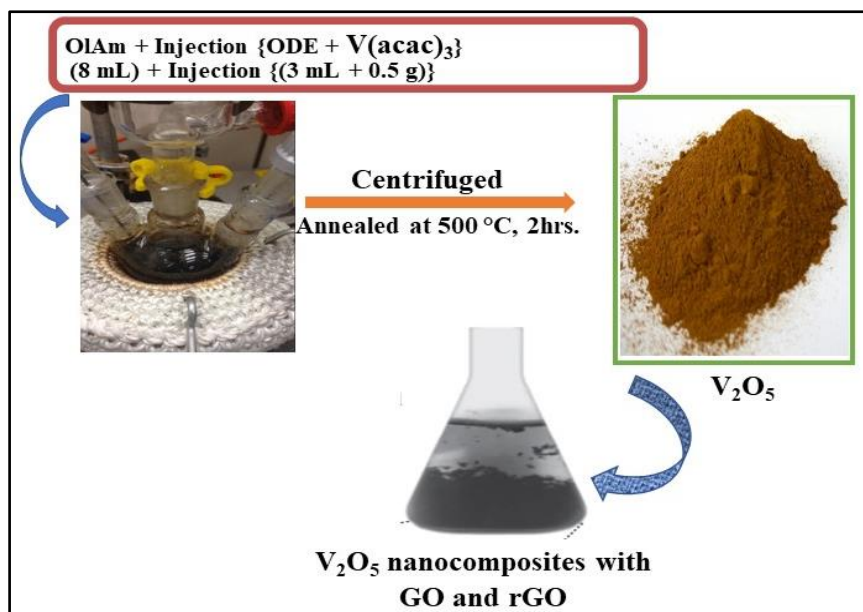


Figure 2.6. Schematic illustration for the synthesis of V_2O_5 nanoparticles, $\text{V}_2\text{O}_5/\text{GO}$, and $\text{V}_2\text{O}_5/\text{rGO}$ nanocomposites.

2.2.7. Synthesis of Graphene Oxide (GO) and Reduced Graphene Oxide (rGO)

In a typical synthesis, 3.0 g of graphite powder and 1.5 g sodium nitrate were mixed in flask. Then, 10 mL of sulphuric acid was added dropwise at $10 \text{ }^\circ\text{C}$ and 9.0 g of KMnO_4 immediately added in the mixture while stirred for 3 hours. In addition, 300 mL of H_2O poured into the solution and maintained at $90 \text{ }^\circ\text{C}$ for 1 hour. After that, 60 mL of 35% H_2O_2 added, washed with deionized water and 5% HCl to attain neutral pH. The mixture was centrifuged and dried at 70°C to obtain brownish powder of GO. The rGO was obtained by annealing of GO at 350°C .

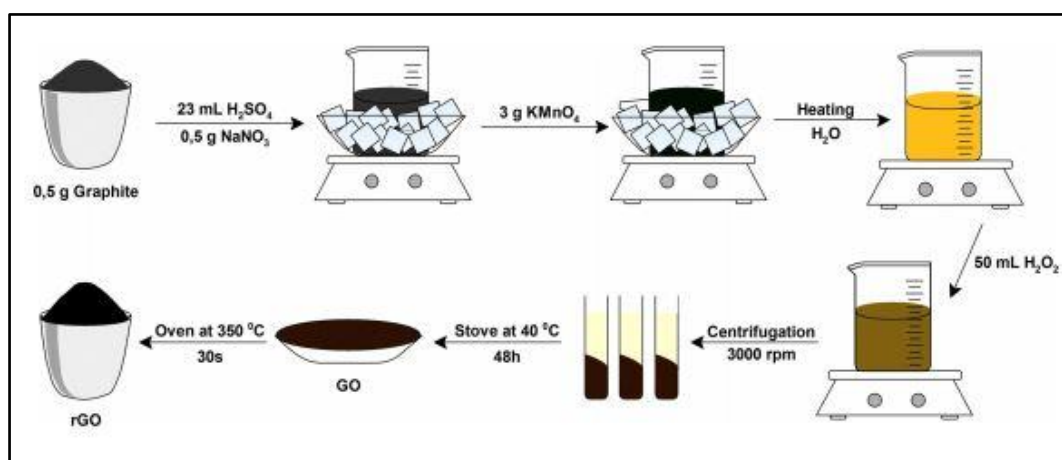


Figure 2.7. Schematic illustration for the synthesis GO and rGO.

2.3. Electrode Fabrication

Gamry instrument (interface 1010E) is used for electrochemical analysis. However, reference (Ag/AgCl) and counter (Pt foil) are employed. The active material, carbon black, and binder (polyvinylidene fluoride, PVDF) are used for the fabrication of working. The slurry is prepared with the weight ratios of 8:1:1 and dissolved in N-methyl-2-pyrrolidone (NMP). Then the slurry deposited on nickel foam having dimensions $1 \times 1 \text{ cm}^2$. Moreover, the fabrication process for the symmetric device followed the same steps as for the three-electrode system and measurements were carried out in 2 M KOH electrolyte with the exception that the nickel foam dimensions are $2 \times 3 \text{ cm}^2$. The mass of the materials has been loaded $1 \text{ mg} \pm 5\%$ on each electrode which was calculated before and after the loading. In case of three electrode configuration, the specific capacitance was determined by CV and GCD profiles using equation 18 and 19.²⁵² For symmetric devices, Csp values are evaluated by equation (20).

2.4. Physical Characterization with Sample Preparation Method

2.4.1. Powder X-ray Diffraction (P-XRD)

PXRD recorded on Bruker advance AXS D8 using a Cu source running at 30 kV and 10 mA. The as-prepared nanostructures powder was spread out over a silicon waver to prepare the sample. The measurement was carried out using WinXPow program and references from the inorganic Crystal Structure Database.

2.4.2. Raman and FTIR Spectroscopy

Nanostructures were analysed by exciting materials using a 633 nm diode-pumped solid-state laser and registered with a Renishaw InVia equipped with a Leica microscope at a spectral resolution of approximately 2 cm^{-1} . The samples were prepared via spreading nanostructures powder onto a thin Al film for Raman measurements. To prevent samples from heating under the microscope lens, the incident laser power was maintained below 0.02 mW. Furthermore, the nanostructures were elucidated via FT-IR (PerkinElmer Frontier 100 with ATR Diamond). The sample is placed over the surface of the attenuated total reflectance (ATR) diamond crystal and then IR beam is directed from below into the sample to a depth of only 1 to 2 micrometres.

2.4.3. X-ray Photoelectron Spectroscopy (XPS)

A Kratos Axis Super XPS (X-ray Photoelectron Spectroscopy) instrument with Al $K\alpha$ X-ray source ($h\nu = 1486.6 \text{ eV}$) was used to carry out XPS analysis. The

adventitious C 1s with 284.8 eV as a reference for the binding energies of all the elements.

2.4.4. Scanning Electron Microscopy (SEM), Elemental Mapping, and Energy-dispersive X-ray (EDX) Spectroscopy

Nanostructures were analysed via scanning electron microscopy (SEM, FEI Quanta 400) on an Oxford Instrument Explore 30. The samples were prepared by uniformly depositing powders on Al stubs and then a layer of carbon was coated onto them via sputtering to prevent the build-up of charge, enhancing the quality of the images. Furthermore, the elemental mapping and energy-dispersive X-ray spectroscopy (EDX) were carried out during the conventional SEM analysis to determine the homogeneous particles distribution and composition.

2.4.5. Transmission Electron Microscopy (TEM)

The images were acquired by making their dispersion in the water and dropping them onto copper grids that had been coated with carbon, and the solvent was then evaporated. The imaging was carried out on a conventional JEOL JEM-1200 EX MKII microscope.

2.4.6. Thermogravimetric Analysis (TGA) and Differential Scanning Calorimetry (DSC)

TGA spectra of as-prepared nanostructures were measured by using TA Instruments Q5000, under N₂. The sample was placed over the platinum pan and maintained the desire temperature of the instrument for analysis. Similar to TGA, DSC analysis was carried out under the same conditions using TA Instruments Q2000. The sample was placed on an aluminium pan, covered with a lid, and subjected to desired temperature for analysis. TA universal analysis software being used to interpret the data for both the techniques. The data for both techniques were being interpreted using TA universal analysis software.

This chapter is consisting of four main sections, which are as follows: (i) probing the synergy of Ni(OH)₂/NiO nanoparticles supported on rGO for battery-type supercapacitors, (ii) investigating the impact of Ag nanoparticles on N and S co-doped TiO₂ for battery-type supercapacitor application, (iii) Hydroxide/oxides of nickel and Mn for their ability to be employed as electrochemical battery-type supercapacitors, (iv) V₂O₅ based nanocomposites electrode materials for high-performance electrochemical supercapacitors, Throughout this chapter, a comprehensive investigation of the as-synthesize materials was discussed for supercapacitor applications.

Part-01

3.1. Probing the Synergy of Ni(OH)₂/NiO Nanoparticles Supported on rGO for Battery-Type Supercapacitors

3.1.1. PXRD Analysis

The phase purity of pure Ni(OH)₂, NiO, Ni(OH)₂/rGO and NiO/rGO was confirmed by PXRD analysis as represented in **Figure 3.1(a)**. The profile of Ni(OH)₂ nanoparticles matches well to the β-phase of hexagonal brucite structure with standard pattern (JCPDS 01-1047). No extra peak appeared which indicated that the material is in a single phase. **Figure 3.1(b)** presents PXRD of NiO nanoparticles which were obtained via thermal decomposition of Ni(OH)₂ nanoparticles. All peaks observed are those expected for cubic crystalline structure of NiO nanoparticulate. The Ni(OH)₂/rGO nanocomposite has almost identical characteristic peaks to those of Ni(OH)₂ except a less intense characteristic peak of rGO nanosheets at 25.55°, which matches well with the (002) plane of the rGO and confirm the uniform growth of nanoparticles as demonstrated in **Figure 3.1(c)**. NiO/rGO nanocomposite has all the peaks revealing the perfect cubic crystalline structure of the NiO with an additional less intense peak of graphene nanosheets as seen in **Figure 3.1(d)**.

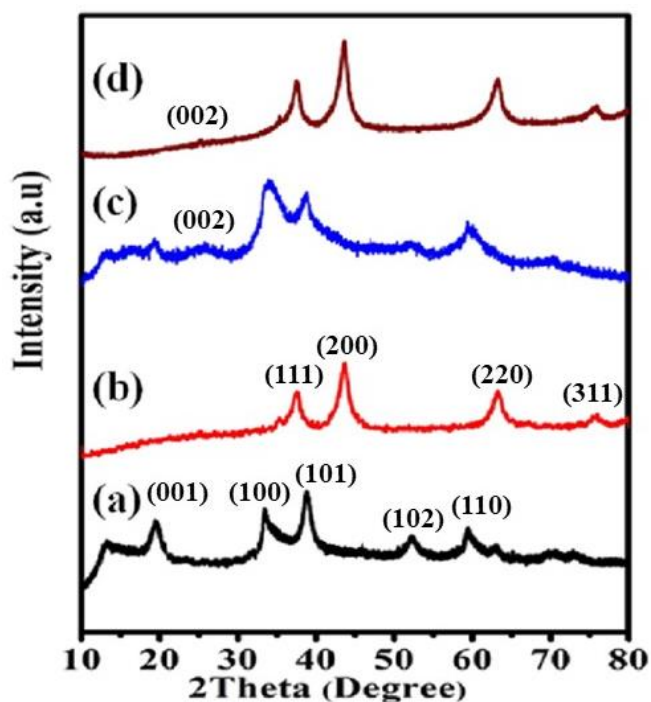


Figure 3.1. PXRD patterns of (a) Ni(OH)₂ nanoparticles, b) NiO nanoparticles, c) Ni(OH)₂/rGO nanocomposite, d) NiO/rGO nanocomposite.

3.1.2. XPS Analysis

Additionally, oxidation state of each element present in Ni(OH)₂/rGO was indicated by XPS analysis. The two main spin-orbit peaks which are appeared at 856 (2p_{3/2}) and 873.6 eV (2p_{1/2}) can be assigned to Ni 2p with two satellite peaks at 862.7 and 274.1 eV, which is consistent with the literature on Ni(OH)₂/rGO,²⁵³ as displayed in **Figure 3.2(a)**. C1s spectra revealed five characteristic bands of C=C, C-C, C-O, C=C, and O-C=O located at energies of 284.39, 285.60, 287.90, and 289.00 eV displayed in **Figure 3.2(b)**. The C1s spectrum verified that the sample contained rGO. There were two peaks in the deconvoluted O1s spectrum that are caused by Ni-O-H and surface water as in **Figure 3.2(c)**. However, for NiO/rGO nanocomposite similar characteristics appear for each element with slight change in the binding energies as in **Figure 3.2(d, e, f)**. In case of O1s no peaks observed for surface water because the NiO/rGO obtained after the annealing of Ni(OH)₂/rGO. The surface water molecules have been evaporated due to annealing effect.

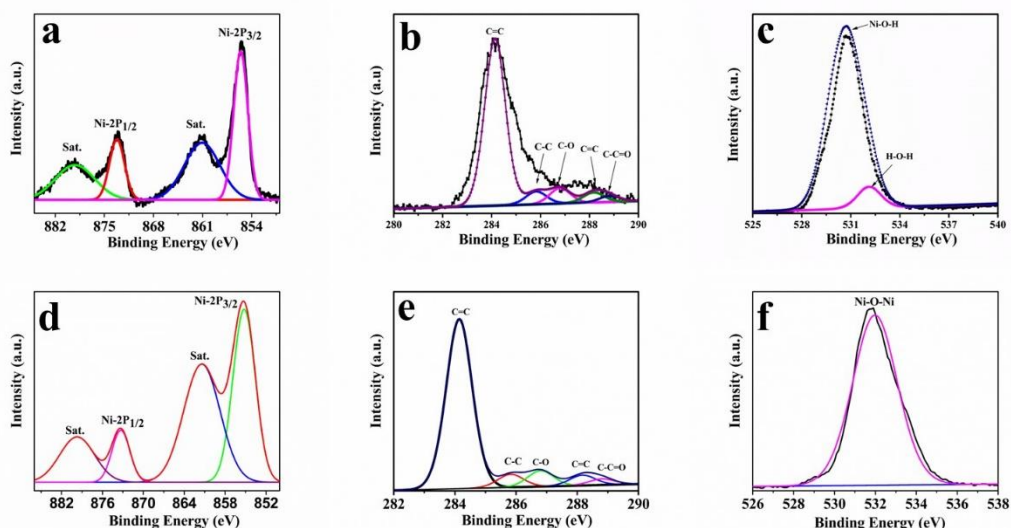


Figure 3.2. XPS spectra of Ni(OH)₂/rGO nanocomposite, a) Ni-2p, b) C-1s, c) O-1s, and NiO/rGO nanocomposite, d) Ni-2p, e) C-1s, f) O-1s

3.1.3. SEM Analysis

Figure 3.3(a) demonstrated that the pure Ni(OH)₂ nanoparticles have nearly spherical shape. The shape of NiO nanoparticles is approximately spherical and of different sizes. After annealing at higher temperature, the size of the particles increased, as the small particles diffused with each other due to thermal effect as seen in **Figure 3.3(b)**. Moreover, the morphology of the nanocomposites has been seen in **Figure 3.3(c, d)**.

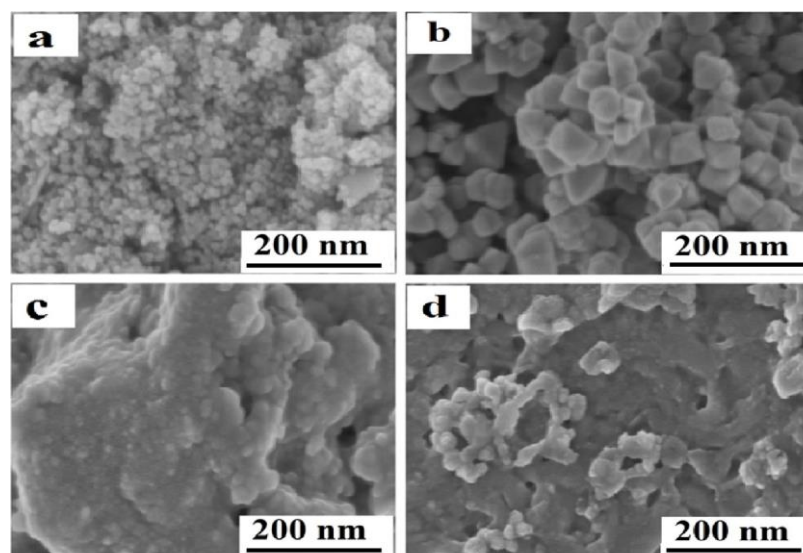


Figure 3.3. SEM images a) Ni(OH)₂ nanoparticles, b) NiO nanoparticles, c) Ni(OH)₂/rGO nanocomposite, d) NiO/rGO nanocomposite.

3.1.4. Elemental Mapping Analysis

Furthermore, the elemental mapping of Ni(OH)₂/rGO nanocomposite is demonstrated in **Figure 3.4**. The images show homogeneous distribution of nickel, oxygen, and carbon. The mapping was recorded at lower magnification so that the distribution can be presented in a satisfying way.

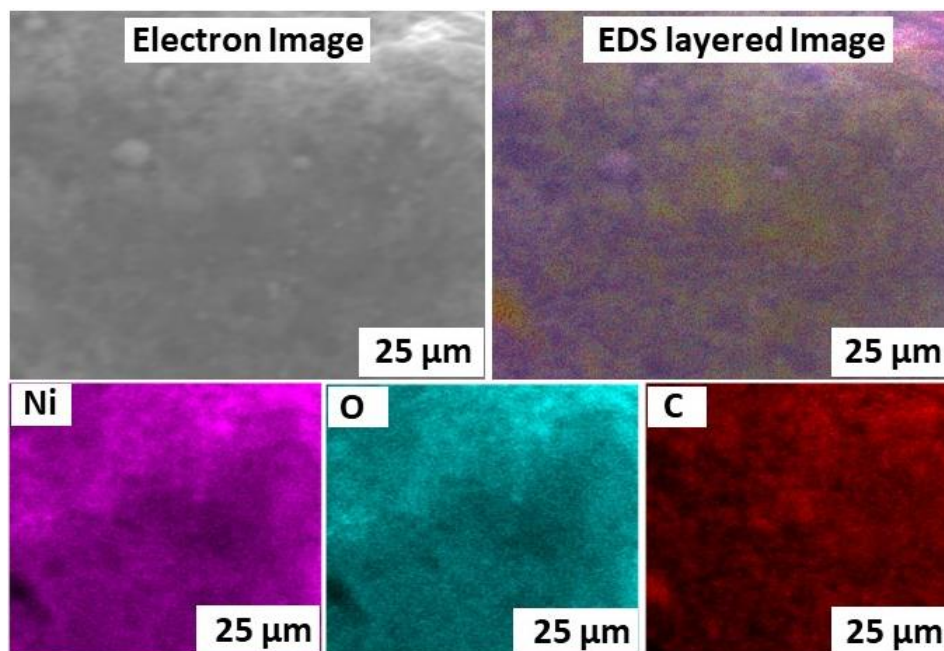


Figure 3.4. Elemental mapping images of Ni(OH)₂/rGO nanocomposite.

3.1.5. TEM Analysis

Figure 3.5 depicts the representative TEM images of as prepared nanomaterials. Ni(OH)₂ shows a very smooth and spherical particle morphology, which form a network through attachment and align themselves at certain planes. The particle sizes are indeed in the nanoscale as in **Figure 3.5(a)**. NiO nanoparticles obtained are presented in **Figure 3.5(b)**. Annealing at higher temperature, a growth of nanoparticles was observed in the micrographs and mean particle diameter has been increased. NiO nanoparticles possess mainly spherical shape. Further, Ni(OH)₂ nanoparticles grown on rGO can be clearly detected as displayed in **Figure 3.5(c)**. The presence of rGO sheets can be easily distinguished around the nanoparticles. By incorporating graphene sheets, NiO nanoparticles are well decorated homogeneously on the rGO sheets shown in **Figure 3.5(d)**.

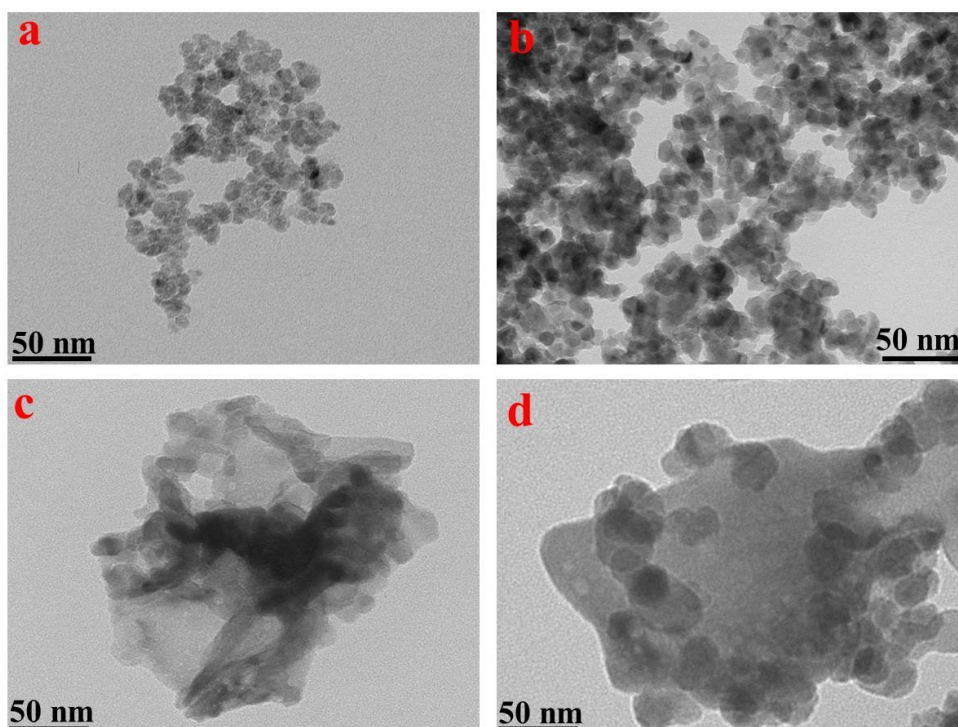


Figure 3.5. TEM images a) Ni(OH)₂ nanoparticles, b) NiO nanoparticles, c) Ni(OH)₂/rGO nanocomposite, d) NiO/rGO nanocomposite.

3.1.1. Electrochemical Investigation of Nanocomposites for Three-Electrode Configuration

3.1.1.1. CV Analysis

The redox behaviour of as-prepared active materials was investigated via CV over a range of scan rate from 10-100 mV s⁻¹ in an operating potential window of -0.2 to +0.6 V using 2 M KOH as seen in **Figure 3.6(a, b, c d)**. The CV curves reflect the battery-type behaviour for all the fabricated electrodes and remain undisturbed even at higher scan rates.²⁵⁴ A pair of reversible peaks appeared in the CV profiles which contributed to Faradaic reactions for the Ni ions in the basic medium, which normally occur at electrode. As scan rate increase caused a change in the position of the redox peaks values which suggests that the Faradaic reactions may be controlled by the ion diffusion process and results in electrode polarization.²⁵⁵ Furthermore, an increase in scan rate results in a gradual increment in the peak current, implying ion and electron transfer in the electrode. Under positive current density, the anodic peak appeared for Ni(OH)₂ at 0.42 V and for NiO at 0.38 V (vs Ag/AgCl), indicating an oxidation process, whereas the cathodic peak appeared for Ni(OH)₂ at 0.16 V and NiO at 0.21 V

against the reference electrode, anticipating the reduction process. The Faradaic reaction can be illustrated by equation (24).



$\text{Ni(OH)}_2/\text{rGO}$ nanocomposite achieved a maximum of 1255.12 F g^{-1} specific capacitance at 10 mV s^{-1} , from CV curves as shown in **Figure 3.6(b)**. The reason for the high performance of the nanocomposite is primarily due to synergistic effect arises from both the components of the active material. It is clear from the morphology of the nanocomposite that the Ni(OH)_2 nanoparticles are uniformly grown on rGO sheets, which consequently enhance the electrochemical kinetic. However, the NiO/rGO nanocomposite has shown lower value of 636.84 F g^{-1} at same scan rate of 10 mV s^{-1} as presented in **Figure 3.6(d)**, which was resulted due to the growth of NiO particle size after annealing at higher temperature. As the particle size increases the density of grain boundaries decreases, which causes inefficient paths for the transport of the electrons and ions. In addition, NiO and Ni(OH)_2 nanoparticles have also shown a significant electrochemical performance in comparison to nanomaterials described above. **Table 3.1** demonstrated the values of specific capacitance determined from CV.

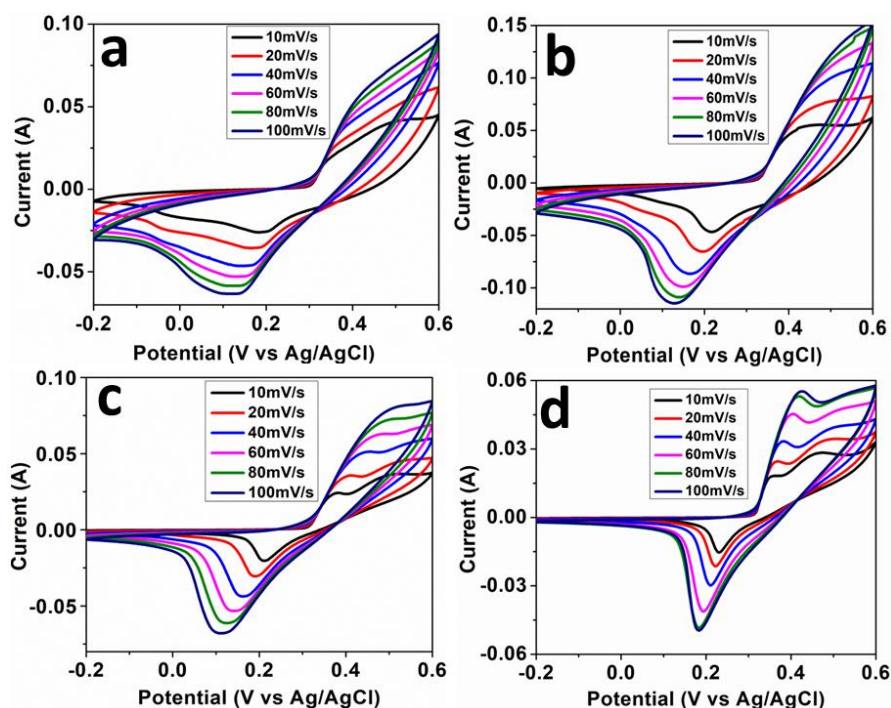


Figure 3.6. Cyclic voltammogram for the fabricated electrodes a) Ni(OH)_2 nanoparticles, b) $\text{Ni(OH)}_2/\text{rGO}$ nanocomposite, c) NiO nanoparticles, d) NiO/rGO nanocomposite.

Table 3.1 Specific capacitance (F g^{-1}) calculated from CV.

Scan rate (mV s^{-1})	10	20	40	60	80	100
Ni(OH) ₂	959.91	600.88	342.96	240.05	192.17	162.73
Ni(OH) ₂ /rGO	1255.12	1042.42	834.67	587.78	365.90	261.63
NiO	475.87	323.78	215.33	198.71	176.34	144.28
NiO/rGO	636.84	474.84	344.81	284.56	247.94	144.28

3.1.1.2. GCD Analysis

To further elucidate the electrochemical behaviour, we performed the galvanostatic charge-discharge analysis from 1 to 10 A g^{-1} over a potential range 0 to 0.4 V in 2 M KOH electrolyte as in **Figure 3.7(a, b, c, d)**. The GCD curves anticipate the non-linear slope with respect to current density which reveals a battery-type capacitive nature of the materials, meaning that Faradaic reactions predominate than linear reactions and in coherence with CV curves. However, the curves reveal the great reversibility and symmetric nature at 10 A g^{-1} . GCD curves of Ni(OH)₂/rGO nanocomposite indicate greater discharge time as compared to pristine Ni(OH)₂ which resulted in a highest specific capacitance of 1092.5 F g^{-1} at 1 A g^{-1} as shown in **Figure 3.7(b)**. Subsequently, the higher specific capacitance of Ni(OH)₂/rGO nanocomposite is due to its larger charge capacity than other tested materials. While NiO/rGO shows a decrease in the specific capacitance to Ni(OH)₂/rGO determined from GCD, which is 1070 F g^{-1} at 1 A g^{-1} as in **Figure 3.7(d)**. The decrease in capacitance can be due to agglomeration of NiO nanoparticles on the surface of rGO and increase in particle size which consequently cause the inadequate redox reactions. Furthermore, another reason contributes to the reduction in the capacitance resulting from the leaching of electroactive material from electrodes during electrochemical reactions. **Table 2** summarizes the specific capacitance values determined from GCD analysis at various current densities.

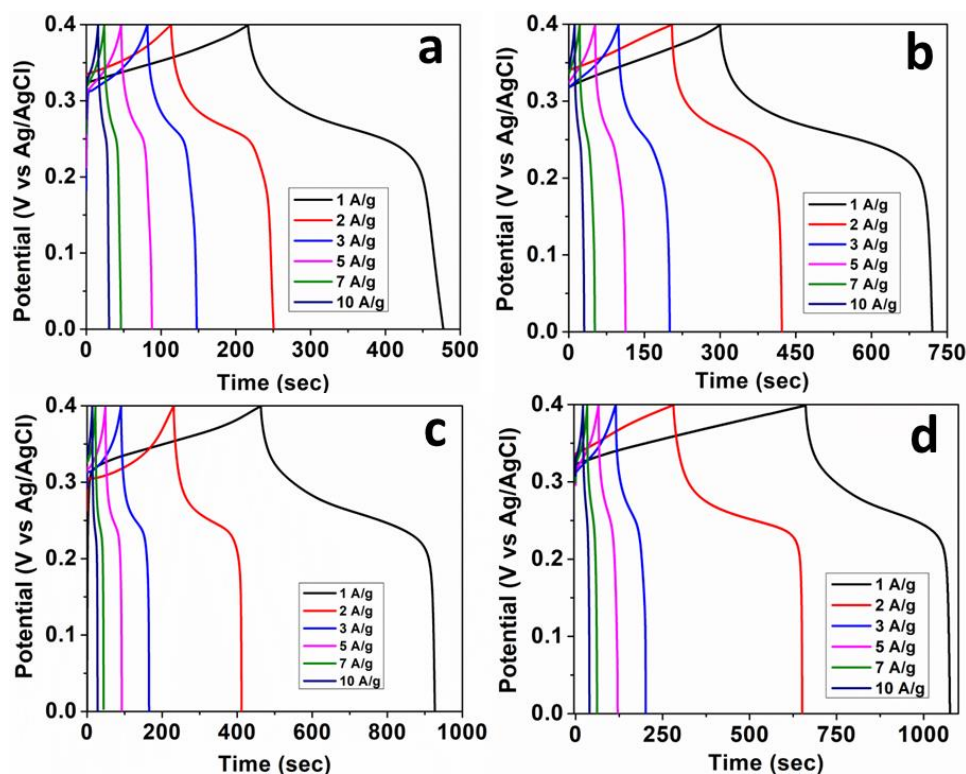


Figure 3.7. GCD profiles of a) Ni(OH)₂ nanoparticles, b) Ni(OH)₂/rGO nanocomposite, c) NiO nanoparticles, d) NiO/rGO nanocomposite.

Table 3.2 Specific capacitance (F g⁻¹) calculated from GCD.

Current density (A g ⁻¹)	1	2	3	5	7	10
Ni(OH) ₂	707.5	645	510	455	332.5	300
Ni(OH) ₂ /rGO	1092.5	975	810	737.5	612.5	450
NiO	987.5	905	595	482.25	385	312.5
NiO/rGO	1070	965	742.5	700	560	475

3.1.1.3. Quantitative Calculation of Surface and Diffusion Capacitance by Dunn's Method

Furthermore, the detailed capacitive behaviour of the Ni(OH)₂/rGO and NiO/rGO nanocomposites was investigated by Dunn method to analyse the surface and diffusion capacitance in the aqueous electrolyte. Equation below is employed to calculate the surface and diffusion contribution.

$$i(V) = k_1 v + k_2 v^{\frac{1}{2}}$$

Where, k_1v and $k_2v^{1/2}$ are the contribution from the surface and diffusion capacitance. The value of the K_1 and k_2 can be evaluated from the slope and intercept of the line, when a plot is drawn between $i(V)/v^{1/2}$ vs $v^{1/2}$ at various scan rates as shown in **Figure 3.8(a, c)**. At lower scan of 10 mV s^{-1} Ni(OH)₂/rGO showed 91% stored energy from diffusion-controlled and 9% from the surface process. On the other hand, NiO/rGO possesses 81% diffusion and 19% surface phenomena as seen in **Figure 3.8(b, d)**. Therefore, at low scan rate the more contribution from the diffusion process indicates that the ions have enough time to permeate into the inner surface of the materials comparative to higher scan rates.

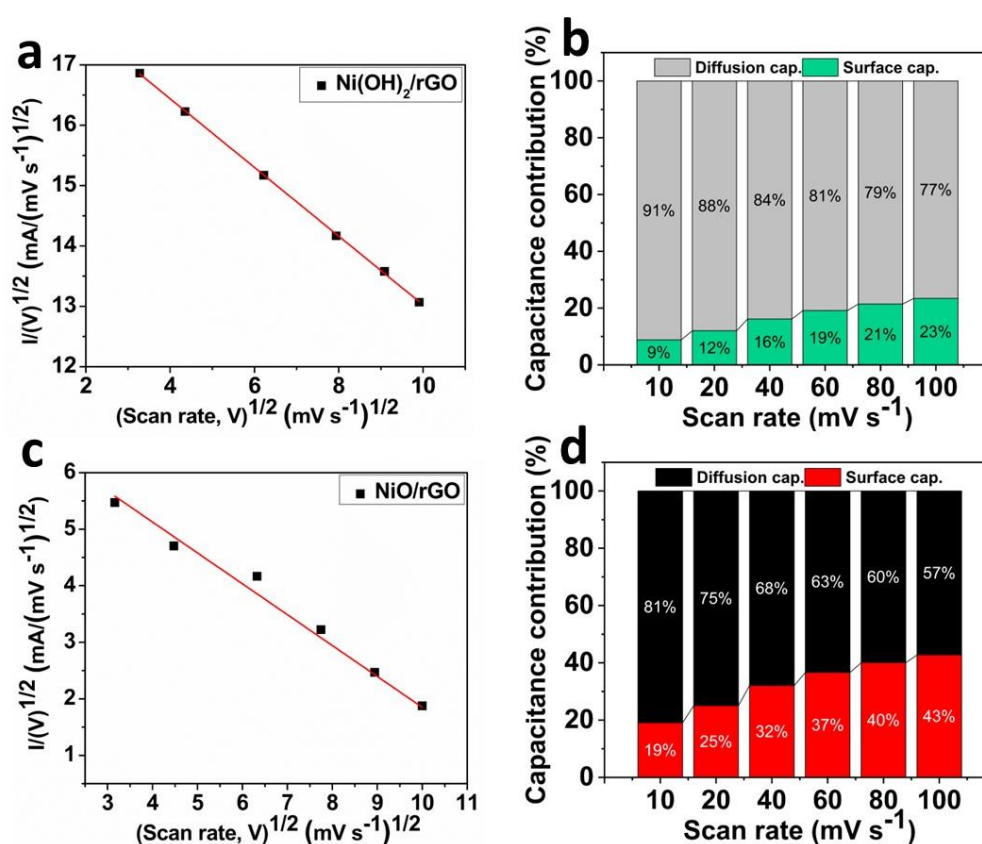


Figure 3.8. Percentage analysis of surface and diffusion capacitance for Ni(OH)₂/rGO and NiO/rGO nanocomposites using Dunn's method (a, c) Plots of $(i/v^{1/2})$ vs $(v^{1/2})$, (b, d) Contribution from both the capacitance at various scan rates.

3.1.1.4. EIS Analysis

EIS is one of the important tools to determine the electrochemical kinetic and performance of supercapacitor electrodes. EIS was performed in 0.1 Hz to 100 kHz at open circuit potential (OCP). Nyquist plots showing the EIS spectra of as-prepared nanomaterials, which revealed a much-suppressed semi-circle towards longer

frequency while a steep line in lower frequency and can be assigned to charge transfer processes occurring at the electrode²⁵⁶ as displayed in **Figure 3.9**. The bulk resistance is indicated by the intercept of the real axis, and a shift to lower values indicates a decrease in bulk resistance of the electrode. The bulk resistivity of Ni(OH)₂ and NiO is much more than that of their nanocomposites with rGO. In the low frequency range, a steeper slope and a narrow curve to the imaginary line anticipate a higher ion transfer rate. Ni(OH)₂/rGO nanocomposite has larger slope value of all the tested electrodes, indicating a faster rate of ion transfer through the interface and demonstrating lower ion diffusion resistance while small arc at high frequency region and substantially very low charge transfer resistance. Randles equivalent circuit has also been included inset of Figure 3.9.

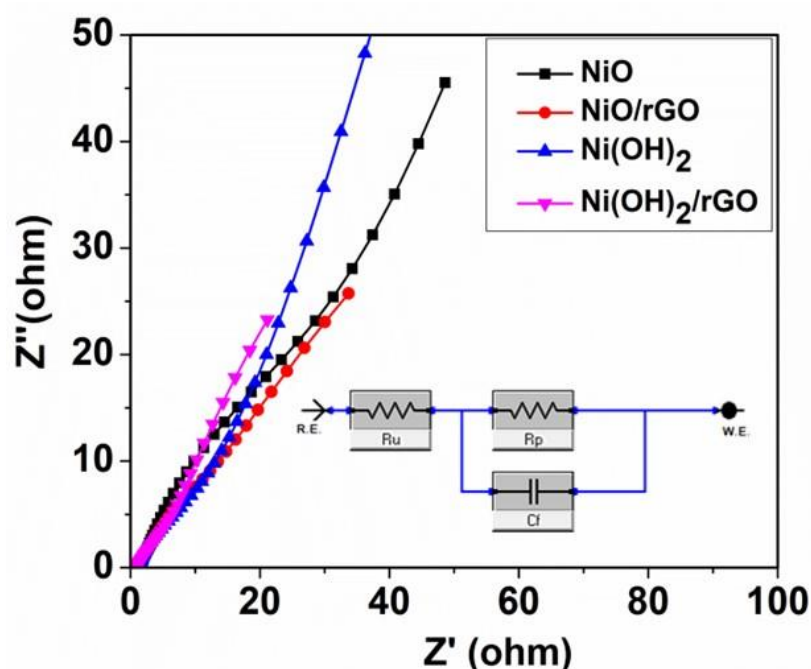


Figure 3.9. Nyquist plots.

3.1.2. Electrochemical Investigation of Nanocomposites for Symmetric Devices

3.1.2.1. CV Analysis

Additionally, the symmetric device performance for Ni(OH)₂/rGO and NiO/rGO were also investigated. During the analysis, Whatman filter paper is utilized as a separator between the electrodes. The CV measurements revealed that the appropriate operating potential window is up to 0 to 1.4 V for both the materials²⁵⁷, and a sudden rise in the current observed at high voltage because the battery-type materials

involve the Faradaic reaction in which many kinetic effects lead to the electrode polarization in battery materials as shown in **Figure 3.10(a, c)**. However, the CV analysis for devices was studied from 10 to 80 mV s^{-1} as seen in **Figure 3.10(b, d)**. The curves retained their distinctive shapes within the potential range, satisfying their characteristic capacitive nature of the symmetric devices. Notably, the CV profiles displayed a nearly identical quasi-rectangular shape at higher scan rates which indicates kinetic reversibility of the device.

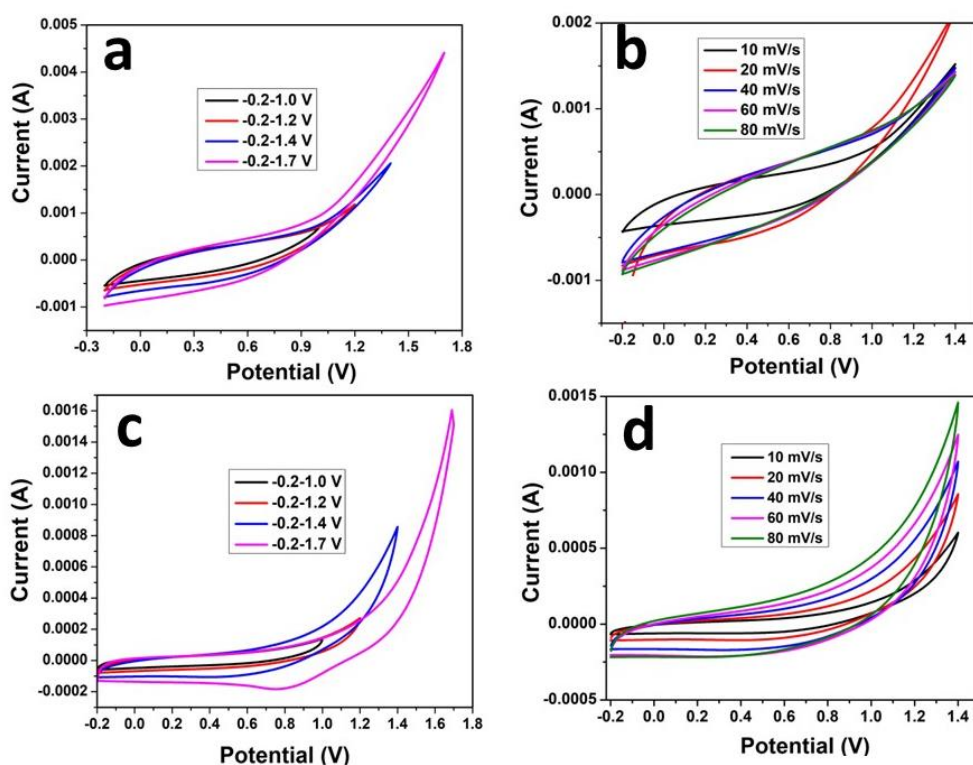


Figure 3.10. (a, c) Optimisation of voltage window for $\text{Ni(OH)}_2/\text{rGO}$ and NiO/rGO , (b, d) CV profiles of $\text{Ni(OH)}_2/\text{rGO}$ and NiO/rGO at various scan rates.

3.1.2.2. GCD Analysis, Cyclic Stability, EIS, Ragone Plots, and Device Architecture

GCD analysis was carried out for $\text{Ni(OH)}_2/\text{rGO}$ and NiO/rGO from 1 A g^{-1} to 5 A g^{-1} current densities in a constant operating window of 0 to 1.4 V as in **Figure 3.11(a, b)**. Herein, the discharge curves show the nonlinear behaviour which is again consistent with battery-type materials. When compared to NiO/rGO electrode, shapes of all the charge-discharge curves reflect that $\text{Ni(OH)}_2/\text{rGO}$ electrode has better rate capability and reversibility. The calculated gravimetric specific capacitance values of as fabricated $\text{Ni(OH)}_2/\text{rGO}$ symmetric device are 115.71, 76.57, 46.71, 32.12, and 24.28 F g^{-1} at 1,

1.5, 2, 3, and 5 A g⁻¹. For NiO/rGO, values are 80.28, 52.86, 38.4, 32.01, and 24.78 F g⁻¹ at the same current densities. The gradual increase in the specific capacitance for both the devices indicates that the electrolyte ions are rapidly moving to the bulk materials with enhancement in current densities. Moreover, with increment in current densities the capacitance values mimicked well with the behaviour seen in the three-electrode.

Cyclic stability of devices is also essential for practical applications. The lifetime for both the devices were also examined for 1000 cycles at 3 A g⁻¹ in the same operating potential window. It was found that the fabricated symmetric devices have retained the 81% and 93% capacity retention which means high cyclic stability of the devices as shown in **Figure 3.11(e)**. Ni(OH)₂/rGO has poorer stability than NiO/rGO because Ni(OH)₂ can undergo chemical transformations, such as conversion to NiOOH or Ni(OH)₃, which can lead to structural instability over time. The EIS measurements of both the devices are illustrated in **Figure 3.11(d)**. Nyquist plots exhibit the same behaviour as observed for three-electrode systems. Ni(OH)₂/rGO demonstrated low Warburg and charge transfer resistance which result the higher conductivity and quick electron transfer for the composite. The corresponding Randles equivalent circuit has also been included inset of the Figure 3.11(d). Ragone plots were also drawn for both the devices which anticipated the improved performance as shown in **Figure 3.11(e)**. Among both the investigated devices, Ni(OH)₂/rGO delivered the highest energy density of 31.5 Wh kg⁻¹ at a power density of 1.4 kW kg⁻¹, which corresponded to a current density of 1 A g⁻¹. The stable high energy and power density of Ni(OH)₂/rGO showed high-rate capability. The results of devices suggest that Ni(OH)₂/rGO and NiO/rGO have massive potential to function in a broad potential window. The schematic illustration of the fabricated device was presented in **Figure 3.11(f)**. **Table 3** compares the electrochemical performance of our fabricated symmetric devices with several previously reported devices.

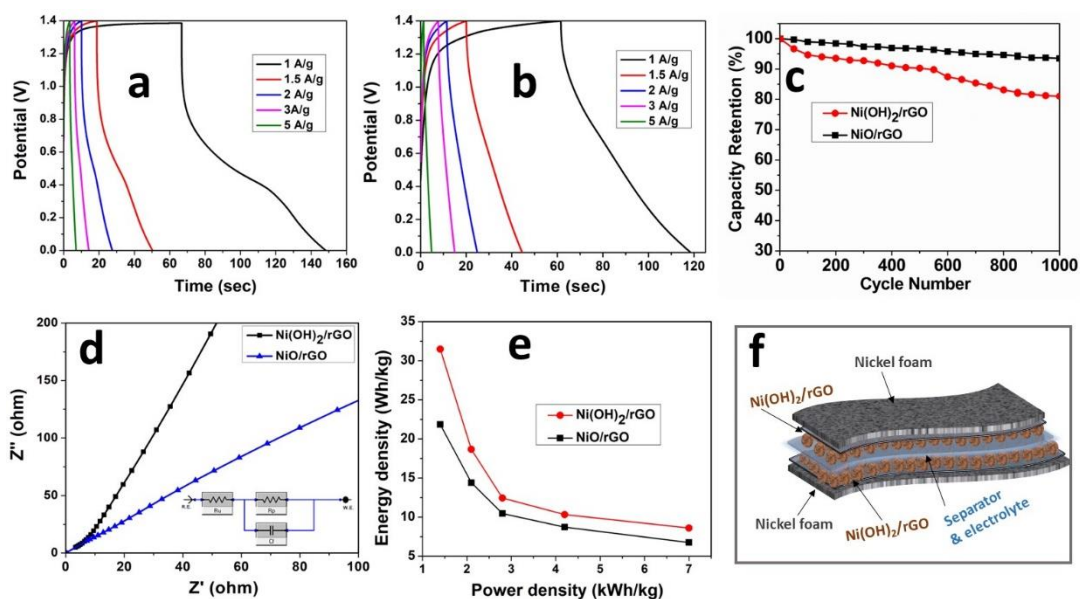


Figure 3.11. GCD profiles of a) $\text{Ni(OH)}_2/\text{rGO}$ nanocomposite, b) NiO/rGO nanocomposite, c) Cyclic stability, d) Nyquist plots, e) Ragone plots, f) Schematic representation of symmetric device.

Table 3.3 Comparison of $\text{Ni(OH)}_2/\text{rGO}$ and NiO/rGO performance with literature reports.

Number	Materials	Configuration	Electrolyte	Energy density (Wh kg^{-1})	Power density (kW kg^{-1})	Ref.
1	3D Porous Carbon	Symmetric	1 M Na_2SO_4 .	12	0.4	258
2	3D Flower-like Porous Carbon	Symmetric.	1 M Na_2SO_4 .	15.9	0.317	259
3	MOF-Derived Porous Carbon	Symmetric.	1 M H_2SO_4 .	10.86	0.225	260
4	$\text{Co(OH)}_2/\text{Co}_3\text{O}_4$	Asymmetric.	2 M KOH.	22.4	0.291	261
5	$\text{NiCo}_2\text{O}_4/\text{rGO}$ Composite	Asymmetric.	2 M KOH.	23.32	0.325	262
6	Leaf-like CuCo_2O_4	Symmetric.	PVA-KOH.	26.52	0.763	263
7	$\text{Ni(OH)}_2/\text{UGA}/\alpha\text{-MGO}$	Asymmetric.	6 M KOH.	6.9	0.044	264
8	$\text{Ni(OH)}_2/\text{CCF}$	Symmetric.	6 M KOH.	35.78	0.350	252
9	$\text{Ni(OH)}_2/\text{AC}$	Symmetric.	6 M KOH.	32.9	0.8	265
10	NiO/rGO	Symmetric.	1 M NaOH.	5.4	0.43	266
11	NiO/rGO	Symmetric.	2 M KOH.	21.86	1.4	This work
12	$\text{Ni(OH)}_2/\text{rGO}$	Symmetric.	2 M KOH.	31.50	1.4	This Work

Part-02

3.2. Investigating the Impact of Ag Nanoparticles on N and S Co-Doped TiO₂ for Battery-Type Supercapacitor Application

3.2.1. PXRD Studies

The PXRD spectra in **Figure 3.12(a)** displays the characteristic patterns of synthesized nanomaterials. The major peaks in PXRD profiles match well with anatase phase of the TiO₂, which are consistent with JCPDS number 83-2243. The peak position at 25.4°, 38.4°, 48.2°, 74.5°, 54.0°, 63.2°, and 64.9° corresponds to (101), (004), (200), (215), (220), (002), and (310) planes, respectively. Notably, no extra peak has been observed for Ag, which possibly overlaps of the Ag signals with TiO₂. It was also noticed that the N, S co-doping and Ag deposition did not create any phase change in TiO₂.

3.2.2. Raman Studies

The structural analysis of the prepared nanomaterials was conducted, as depicted in **Figure 3.12(b)**. In each sample, four characteristic bands were observed, confirmed the anatase phase of TiO₂. Specifically, the band observed at 636.89 cm⁻¹ can be of E_g mode, while the 392.22 cm⁻¹ assigned to B_{1g} mode.²⁶⁷⁻²⁶⁸ The band at 512.50 cm⁻¹ arises from the A_{1g} mode, indicating anatase phase was prominent in all synthesized materials. Furthermore, the band observed at 129.49 cm⁻¹ can be assigned to asymmetric stretching modes. The intensities of these bands vary among the samples, which can be of size, concentration, oxygen vacancies, and defects present in the materials.²⁶⁹ The co-doping of TiO₂ nanomaterials did not cause a shift in the positions of the Raman bands, suggesting the absence of phase transformation. However, the decoration of Ag nanoparticles on TiO₂ did not show any signals in the Raman spectra due to the low concentration and the extremely weak Raman stretching ability of Ag.²⁷⁰⁻²⁷¹ In contrast, an increase in the intensity of bands observed after the co-doping and deposition indicates the interaction between Ag and TiO₂.²⁷²⁻²⁷³

3.2.3. UV-Visible Studies

The absorption spectra of the synthesized nanomaterials have been shown in **Figure 1.12(c)**. The pristine TiO₂ nanoparticles showed the maximum absorption at 286 nm while doping of N, S caused a shift towards the longer wavelength of 300 nm, respectively. However, deposition of Ag on co-doped material showed further shift in

maxima to 318 nm. Consequently, the area under the visible band increased which can be attributed to surface plasmon resonance (PSR) effect. The observed PSR effect arises from the overall vibration of Ag nanoparticle electrons which accelerated by photo excitation.²⁷⁴

3.2.4. Band Gap Studies

Tauc's plot method was applied to calculate the band gap (E_g) of synthesized nanomaterials as in **Figure 3.12(d)**. The band gap calculated for pristine TiO_2 is 3.5 eV, and for co-doped TiO_2 3.2 eV. The reduction in the band gap after co-doping was observed, which can be attributed to the substitution of N and S into the lattice TiO_2 . This decrease in the band gap was observed due to the interaction of N 2p and S 2p with O 2p. Additionally, Ag deposition on co-doped TiO_2 further decreases in the band gap (3.1 eV). The phenomenon has been explained by the free electron properties exhibited by Ag, leading to a shift in the position of the valence and conduction band of TiO_2 . This shift ultimately contributes to a decrease in the E_g value.²⁷⁵

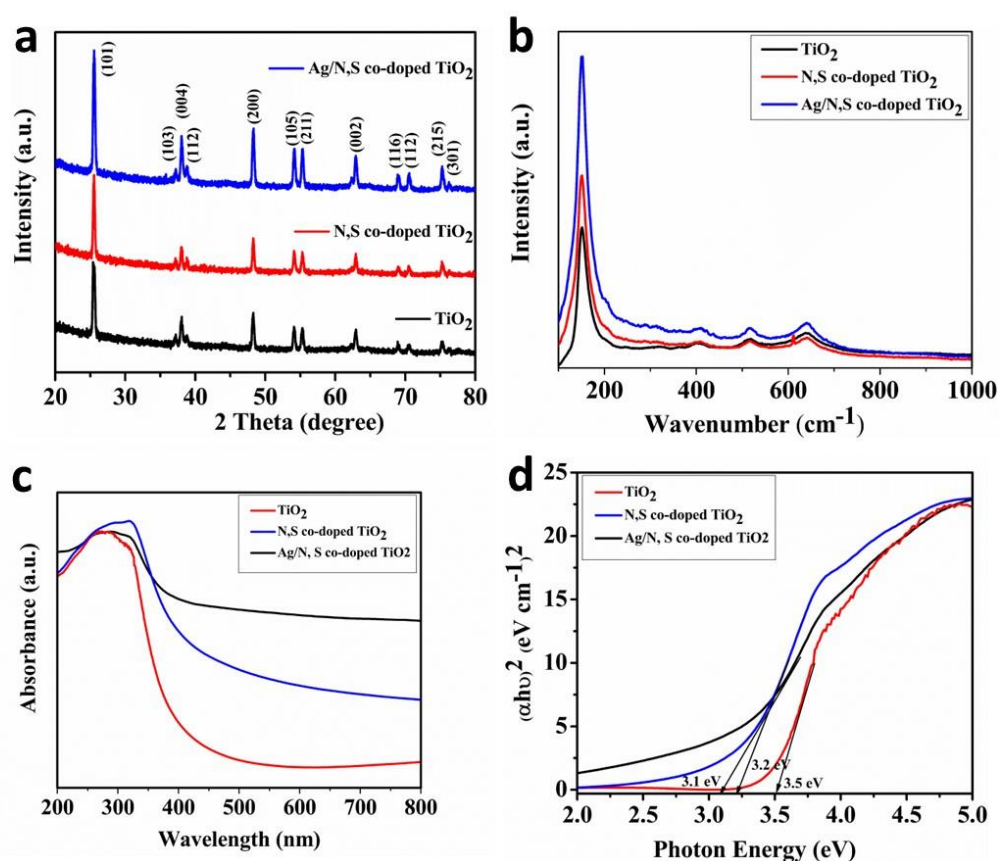


Figure 3.12. (a) XRD patterns, (b) Raman spectra, (c) UV-Vis profiles, and (d) Tauc's plots of pristine TiO_2 nanoparticles, N,S co-doped TiO_2 nanoparticles, and Ag/N,S co-doped TiO_2 nanocomposite.

3.2.5. SEM Studies

Furthermore, morphology of nanomaterials was examined by SEM as illustrated in **Figure 3.13(a-c)**. The images reveal the presence of some spherical and irregular shape of the materials with slight agglomeration of particles at certain regions of images. Overall, no major morphological changes occurred after co-doping with nonmetals. However, very small Ag particles can be observed which were decorated on co-doped materials. Additionally, elemental mapping revealed a homogeneous distribution of all the elements throughout the samples as depicted in **Figure 3.13(d)** with images of each element.

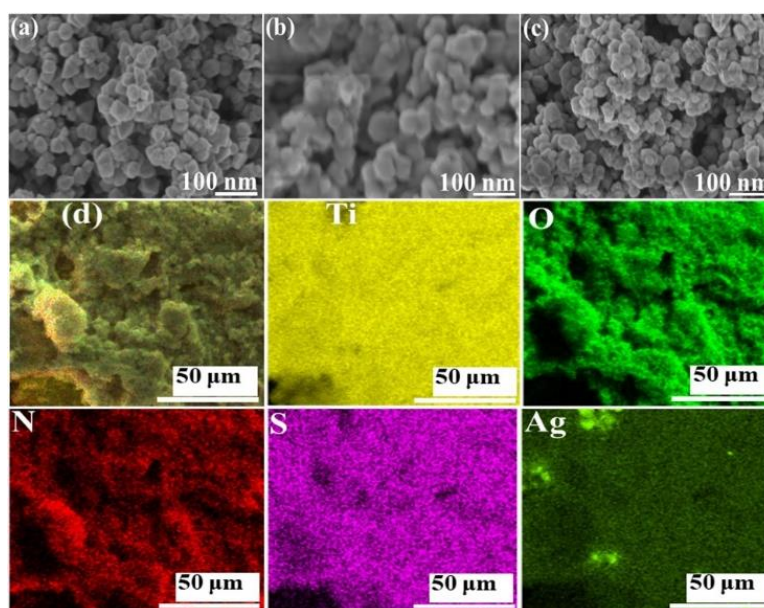


Figure 3.13. Presents SEM images of various materials: a) pristine TiO₂ nanoparticles, b) N,S co-doped TiO₂ nanoparticles, c) Ag/N,S co-doped TiO₂ nanocomposite, and d) EDS mapping of the Ag/N,S co-doped TiO₂ nanocomposite with images of each element.

3.2.6. TEM Studies

The precise shape and size of selected materials was analysed by TEM images as seen in **Figure 3.14(a, b, c)**. The images can clearly indicate that the materials have spherical shape, with particle sizes measuring less than 100 nm. It was also worth mentioning that very small Ag particles decorated on N, S co-doped TiO₂. Furthermore, the SEM images were obtained after the stability test for all the fabricated electrodes as seen in **Figure 3.14(d, e, f)**. There was no change occurred in the morphology of all materials which affirm their exceptional structural stability. Additionally, the SEM

images provide evidence that the nanoparticle films remain fully intact on the surface of the nickel foam and do not leach out into the alkaline electrolyte solution.

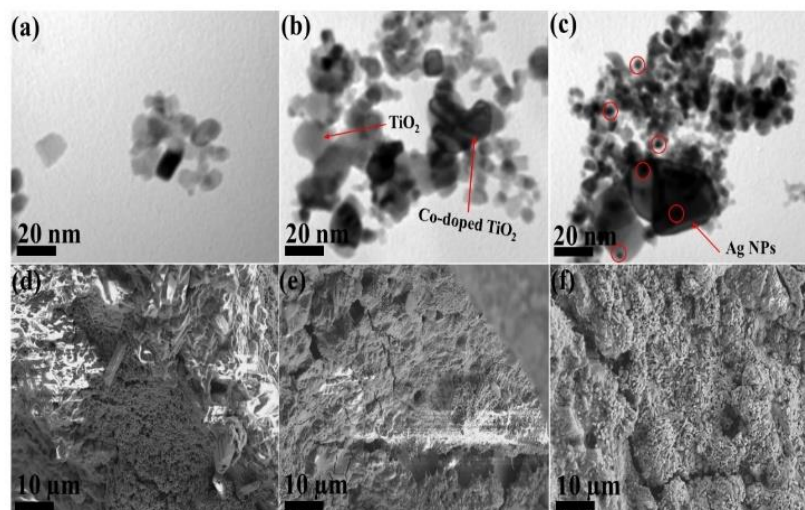


Figure 3.14. TEM images a) pristine TiO_2 nanoparticles, b) N,S co-doped TiO_2 nanoparticles, c) Ag/N,S co-doped TiO_2 nanocomposite, and (d, e, f) SEM images of all materials after stability test.

3.2.1. Electrochemical Investigation of Nanomaterials for Three Electrode Configuration

3.2.1.1. CV Analysis

The as-synthesized nanomaterials were optimized in different electrolytes for CV to check the performance of the prepared materials and no redox peaks appeared as seen in **Figure 3.15(a)**. However, the CV profiles of Ag/N,S co-doped TiO_2 was obtained in 2 M LiOH, 2 M NaOH, and 2 M KOH at 100 mV s^{-1} as displayed in **Figure 3.15(b)**. The redox peaks and area confined by the CV curves is more prominent in KOH than others, suggesting that the KOH has been the most appropriate for further analysis. It is essential to highlight that in aqueous electrolytes, metal cations such as Li^+ , Na^+ , and K^+ undergo hydration, resulting in the formation of hydrated ions. Smaller ions tend to produce larger hydrated ions, while larger ions exhibit distinct hydrated ions. Specifically, Na^+ and K^+ generate hydrated ions with an ionic radius of 3.58 \AA and 3.31 \AA , whereas Li^+ forms larger hydrated ions with an ionic radius of 3.82 \AA . This difference in hydrated ion sizes is crucial as it influences the electrochemical performance of the nanocomposite. As a result, the Ag/N,S co-doped TiO_2 nanocomposite exhibits the highest capacitance when used in the KOH electrolyte compared to LiOH and NaOH.²⁷⁶ Therefore, KOH is a potential candidate for further

electrochemical investigations and CV curves were tested at different concentrations to check the consistency of the redox peaks which suggested the excellent stability of the materials in KOH as in **Figure 3.15(c)**. The CV profiles were conducted for TiO₂, N,S co-doped TiO₂, and Ag/N,S co-doped TiO₂ in 2 M KOH from 0 to 100 mV s⁻¹ as in **Figure 3.15(d, e, f)**. The pair of redox peaks observed in each material because of Faradaic reactions occurred at electrode. For all prepared materials, a consistency has been observed in the CV profiles which demonstrates the superior reversibility and rapid transformation of electrons of active material and electrolyte ions,²⁷⁷ which indicates that the synthesized materials have typical battery-type nature.²⁷⁸ The pair of redox peaks attributed to conversion ion of Ti⁴⁺/Ti³⁺ in the alkaline media while peaks become more prominent with the co-doping of TiO₂ and deposition of Ag nanoparticles.²⁷⁹ Furthermore, oxidation peak and reduction peaks slightly shift to lower and higher voltage, suggesting that great reversibility and improve the stability of electrode. The peaks observed in the CV profiles indicative of surface oxidation and reduction reactions, which were represented by equation (25).

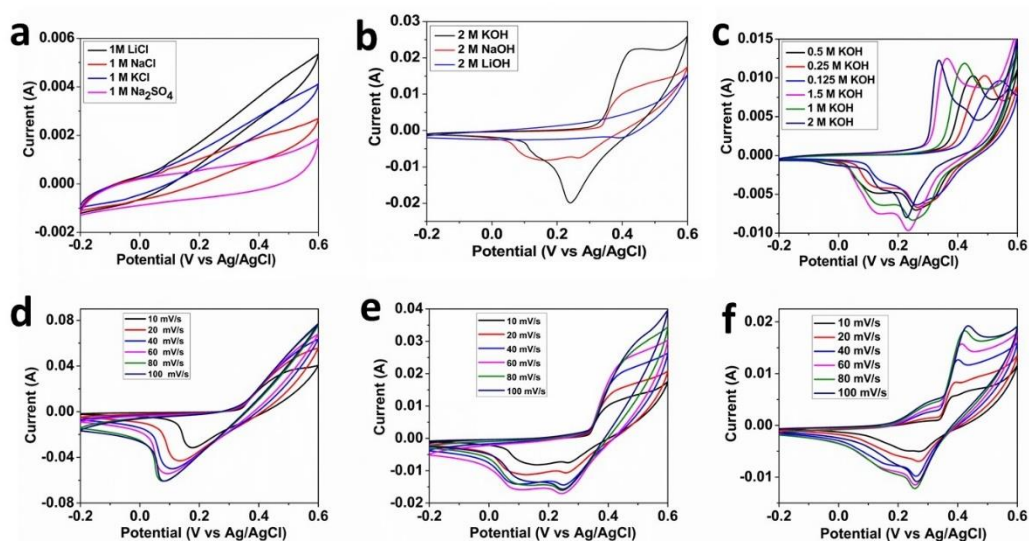
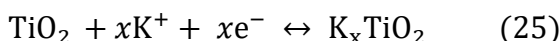


Figure 3.15. shows the following: a) CV curves at different electrolytes, b) Comparative CV profiles of the Ag/N,S co-doped TiO₂ nanocomposite in KOH, NaOH, and LiOH, b) CV curves in different concentrations of KOH, d) pristine TiO₂ nanoparticles, e) N,S co-doped TiO₂ nanoparticles, f) Ag/N,S co-doped TiO₂ nanocomposite.

3.2.1.2. GCD Analysis, Cyclic Stability, EIS, and Bode Phase Angle Plots

The GCD profiles show a non-linear shape which indicates the typical battery-type behaviour as shown in **Figure 3.16(a-c)**. Pristine TiO₂ nanoparticle displayed a Csp values of 274 F g⁻¹ at 1 A g⁻¹. However, upon co-doping of TiO₂ with N, S resulted in an improved Csp value to 360 F g⁻¹. The maximum enhancement in the Csp was observed after the decoration of Ag nanoparticle on co-doped of TiO₂ which is 480 F g⁻¹ at 1 A g⁻¹. The enhancement in Csp of co-doped TiO₂ and Ag deposited co-doped TiO₂ nanoparticles because of synergistic effect which produced N, S co-doping and Ag nanoparticle when combined with TiO₂. All the materials showed excellent Csp values even at the highest current densities which were presented in **Table 4**. However, different working potential windows have been used in CV and GCD because at higher current densities, the materials start performing oxygen evolution reactions during the charging process. The capacity retention as function of cycle number was studied for 1000 cycles at 3 A g⁻¹ for all fabricated electrodes as depicted in **Figure 3.16(d)**. The capacity retention values were 79%, 81%, and 83% for pristine TiO₂, co-doped TiO₂, and Ag/N, S co-doped TiO₂. These capacity retention results clearly demonstrate that the co-doping and deposition of co-doped TiO₂ with Ag nanoparticles excellently improve the performance of the pristine TiO₂ and enhance its versatility for practical applications.

EIS was done in order to find the charge transfer dynamic of the electrode and interface for all the fabricated electrodes. Nyquist plots were drawn for each material which demonstrated a slight semicircle in the low frequency while a linear line towards higher frequency as shown in **Figure 3.16(e)**. R_{ct} can be evaluated from semicircle of the curves. The Ag/N, S co-doped TiO₂ has a very small diameter compared to pristine and co-doped TiO₂, which indicates the rapid transfer of electrons and ions at interface of electrode-electrolyte. The R_{ct} values calculated for N,S co-doped and Ag/N, S co-doped TiO₂ were 0.374 Ω and 0.084 Ω, however, R_s values were 1.028 Ω and 0.898 Ω, respectively. On the other hand, R_s is the overall contribution from electrolyte, internal and contact resistance that can be evaluated from the intercept of the line on the X-axis in high frequency region. The reduction in resistance observed in Ag/N,S co-doped TiO₂, as compared to N,S co-doped TiO₂, can be attributed to the enhanced conductivity achieved through the deposition of Ag nanoparticles. The equivalent circuit model was derived by fitting Nyquist plot data, as illustrated inset of **Figure 3.16(e)**. Therefore, the introduction of a constant phase element (CPE) with diffusion is necessary to fit the

impedance data as depicted in the equivalent circuit diagram. The CPE primarily arises from various internal factors, including processes such as intercalation and deintercalation, active diffusion, non-uniformity, and, most notably, the characteristics and porosity of the fabricated electrode.²⁸⁰ Bode plots demonstrated that all synthesized materials have an excellent capacitive in nature as displayed in **Figure 3.16(f)**.

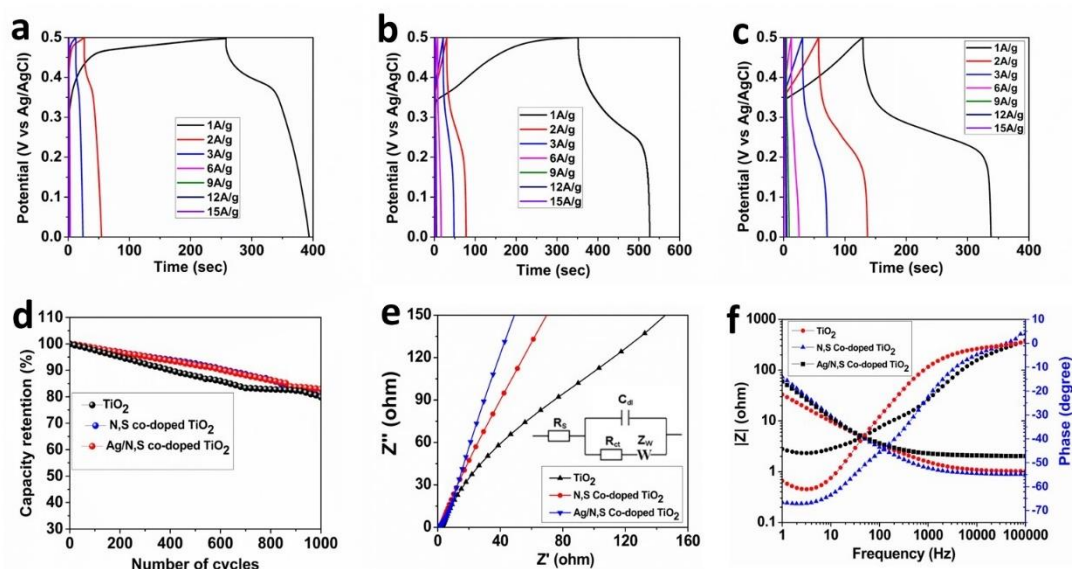


Figure 3.16. GCD profiles of a) pristine TiO₂ nanoparticles, b) N,S co-doped TiO₂ nanoparticles, c) Ag/N,S co-doped TiO₂ nanocomposite, d) cyclic stability, e) Nyquist plots, f) Bode phase angle plots.

Table 3.4 Specific capacitance (F g⁻¹) calculated from GCD.

Current density (A g ⁻¹)	1	2	3	6	9	12	15
TiO ₂	274	112	72	54	48	40	30
N,S co-doped TiO ₂	360	192	132	96	90	80	48
Ag/N,S co-doped TiO ₂	480	320	246	134	90	72	60

3.2.1.3. Quantitative Calculation of Surface and Diffusion Capacitance by Dunn's Method

The surface and diffusion capacitances of the co-doped and Ag decorated co-doped TiO₂ nanomaterials were determined by employing Dunn's method using equation (11). The plots between $i(V)/v^{1/2}$ vs $v^{1/2}$ from the currents obtained from CV at

fixed potentials as depicted in **Figure 3.17(a, c)**. **Figure 3.17(b, d)** illustrates the total contributions of surface and diffusion capacitance for N, S co-doped and Ag deposited TiO₂ electrodes, represented as percentage bars. Notably, at lower scan rates, the diffusion contribution surpasses the surface contribution for both materials. This finding suggests that at lower scan rates, there is sufficient time for ions to intercalate into the inner regions of the electrodes. Specifically, the co-doped TiO₂ exhibits a diffusion capacitance of 84% and a surface contribution of 16%, while Ag deposited TiO₂ shows 85% attributed to diffusion and 15% to the surface.²⁸¹

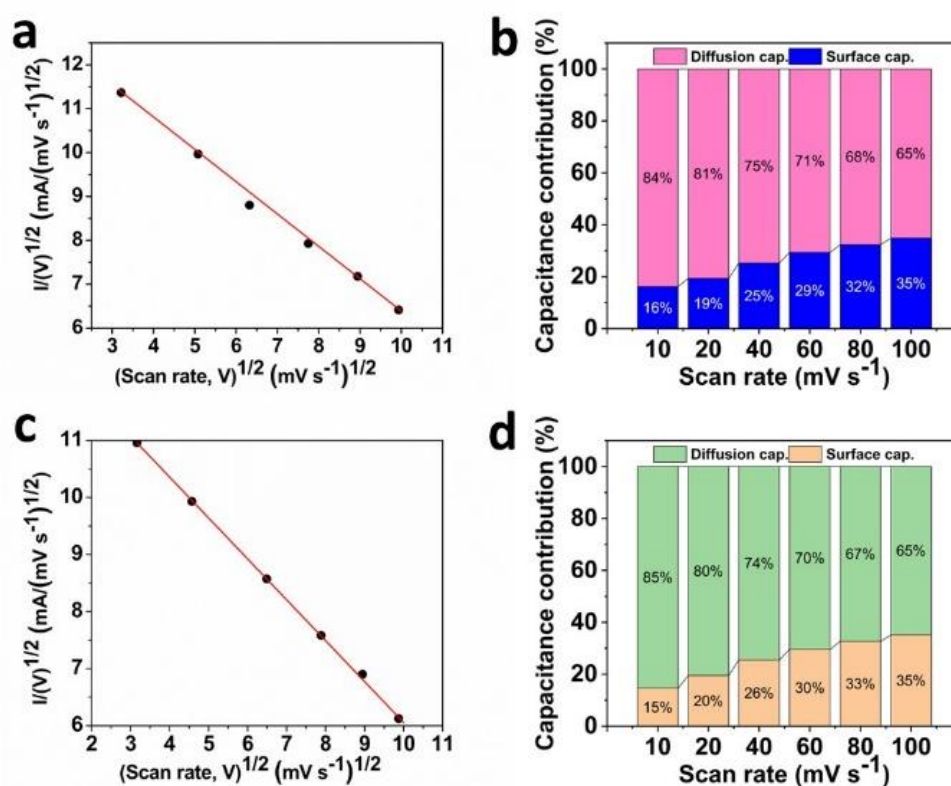


Figure 3.17. A quantitative analysis of surface and diffusion capacitance is presented for N,S co-doped TiO₂ nanoparticles and Ag/N,S co-doped TiO₂ nanocomposite. Panels (a) and (c) Plots of $(i/v^{1/2})$ vs $(v^{1/2})$, (b, d) illustrate the contribution from surface and diffusion capacitances at different scan rates.

3.2.2. Electrochemical Investigation of Ag/N, S co-doped TiO₂ for Symmetric Devices

3.2.2.1. CV, GCD, EIS, and Cyclic Stability Analyses

Additionally, the Ag/N, S co-doped TiO₂ nanocomposite showed promising results in three-electrode studies. As a result, this nanocomposite was chosen for use in symmetric devices. The CV profiles of fabricated device were studied at 10 to 100 mV s⁻¹ in -1 to 1 V in 2 M KOH as shown in **Figure 3.18(a)**. The CV profiles of device reflects the quasi-rectangular shape while GCD profiles are nearly triangular which demonstrated the excellent reversibility of the fabricated device. The Csp of the device was calculated by using GCD profiles as displayed in **Figure 3.18(b)**. Csp values of Ag/N, S co-doped TiO₂ nanocomposite are 183, 165, 133, and 120 F g⁻¹ at 3, 5, 7, and 10 A g⁻¹. **Figure 3.18(c)** displays the Nyquist plot of symmetric device and inset shows the fitting model circuit. The plots was fitted using a constant phase element (CPE) with diffusion model and the values calculated for Rs as well as Rct were 1.401 Ω and 0.521 Ω, respectively. Furthermore, cyclic stability of the device was assessed for 3000 discharge cycles which reveals a capacity retention of 80% as shown in **Figure 3.18(d)**. This highest capacity retention suggested a good structural stability of the device. The obtained data of device indicated that Ag/N, S co-doped TiO₂ nanocomposite holds great prospect for energy storage. The investigated device of Ag/N,S co-doped TiO₂ delivered 105 Wh kg⁻¹ at a power density of 6 kW kg⁻¹ at 3 A g⁻¹. The stable energy and power density of Ag/N,S co-doped TiO₂ demonstrated a remarkable high-rate capability.

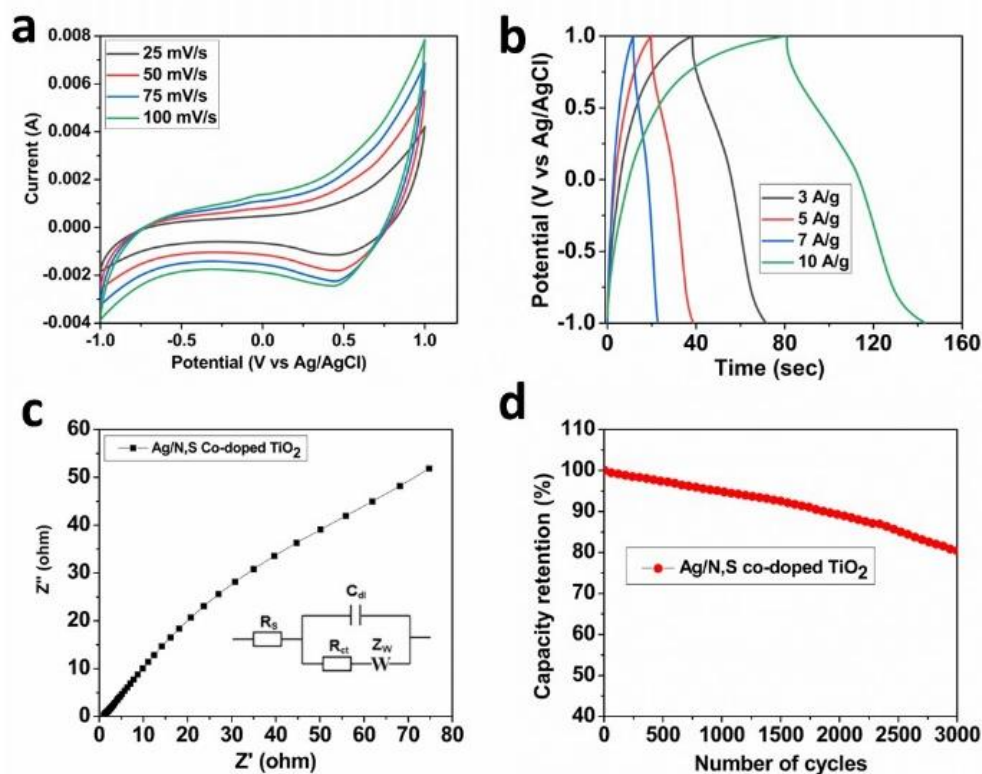


Figure 3.18. (a, b) CV and GCD profiles of fabricated symmetric device of Ag/N,S co-doped TiO₂ nanocomposite, c) EIS profile, d) cyclic stability.

Part-03

3.3. Versatile Synthesis of Metal Oxide Nanoparticles to Fabricate High-Performance Electrode Materials for Advanced Supercapacitors

3.3.1. PXRD Analysis

The X-ray diffraction technique was employed to determine the phase purity of the as-prepared samples as depicted in **Figure 3.19**. The diffraction peaks match well with the monoclinic phase of the α -Ni(OH)₂ with consistent to JCPDS No. 41-1424. No extra peak has been observed which confirmed the single phase of the material **Figure 3.9(a)**. For NiO, which is obtained from heating the Ni(OH)₂ nanoparticles match well with the cubic phase of the material as in **Figure 3.19(b)**. All peaks observed are those expected for cubic crystalline structure and again reveal the phase purity of the nanoparticulate NiO. The crystal structure of the MnO₂ nanoparticles is presented in profile **Figure 3.19(c)**. The PXRD pattern matches that of the tetragonal crystalline phase of MnO₂ in accordance with the standard card (JCPDS No. 44-0141) and indexed

with their respective planes. The XRD profile contains no additional peaks again indicating the formation of a single-phased material. Moreover, profile **Figure 3.19(d)** presents the X-ray diffractogram of α -Ni(OH)₂-MnO₂ hybrid shows peaks associated with α -Ni(OH)₂ (JCPDS No. 41-1424, indicated using an asterisk,*) and MnO₂ (JCPDS No. 44-0141, indicated using a hash, #) are clearly observed in the diffractogram of the hybrid material, confirming that the product does indeed consist of a composite of nanostructures. The peak that appears at $2\theta = 60$ degrees, and represented by (#*), is present in both materials.

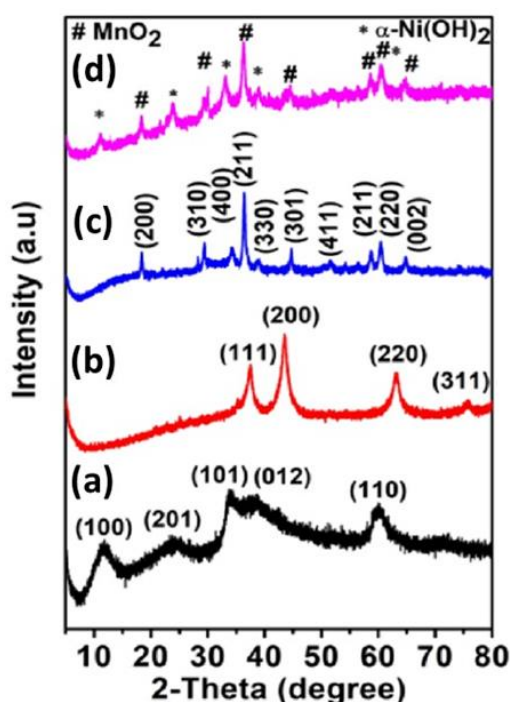


Figure 3.19. PXRD of (a) of α -Ni(OH)₂ nanoparticles, (b) NiO nanoparticles, (c) MnO₂ nanoparticles, (d) α -Ni(OH)₂-MnO₂ hybrid nanomaterial.

3.3.2. Raman Analysis

Further, Raman technique was used elucidate the structural properties of the prepared materials as in **Figure 3.20**. α -Ni(OH)₂ shows strong phonon vibrations at 478 cm⁻¹ and 611 cm⁻¹ which are due to E_g(T) and A_{1g}(T) of Ni-OH vibrations as displayed in **Figure 3.20(a)**. However, the band observed at 998 cm⁻¹ can of α -Ni(OH)₂ two order phonon vibration. Profile **Figure 3.20(b)** shows the profile of nanosized NiO in which three bands at 503 cm⁻¹, 995 cm⁻¹ and 1531 cm⁻¹, are present. The first two bands are vibrational in origin and assigned accordingly as a one longitudinal optical (LO) phonon (503 cm⁻¹) and a two LO phonon (994 cm⁻¹) mode. While at 1531 cm⁻¹ is because of two-magnon (2M). The MnO₂ has only one band at 650 cm⁻¹ can be of Mn-

O lattice stretching shown in **Figure 3.20(c)**. This MnO₂ band appeared due to collective vibrations of MnO₆ octahedron in the tetragonal hollandite-type framework. α -Ni(OH)₂-MnO₂ hybrid has two modes at 515 cm⁻¹ and 630 cm⁻¹ which can attributed to the Ni-O and Mn-O stretching vibrations as seen in **Figure 3.20(d)**.

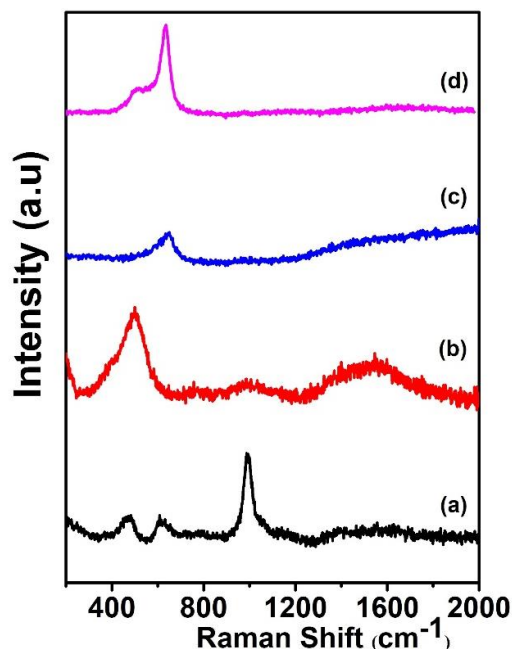


Figure 3.20. Raman spectra of (a) of α -Ni(OH)₂ nanoparticles, (b) NiO nanoparticles, (c) MnO₂ nanoparticles, (d) α -Ni(OH)₂-MnO₂ hybrid nanomaterial.

3.3.3. XPS Analysis

The XPS analysis was used to find out the oxidation state of each element present in the sample. The Ni 2p core-level shows two spin-orbit peaks at 872.2 eV (Ni 2p_{1/2}) and 854.3 eV (Ni 2p_{3/2}) with the existence of two satellite peaks which confirmed that the Ni⁺² state as in **Figure 3.21(a)**.²⁸²⁻²⁸³ The satellite peaks appeared at 861.4 eV and 879 eV, respectively. The separation between the peaks is 17.9 eV, and exactly match reported values. For Mn, two peaks centred at 653.1 eV (Mn 2p_{1/2}) and 642.3 eV (Mn 2p_{3/2}) shows the presence of Mn⁺⁴ state as presented in **Figure 3.21(b)**.²⁸⁴ The O 1s contained three deconvoluted sub peaks at 530.7, 531.6, and 532.8 eV which arises to the Mn-O-Mn, Ni-O-H, and H₂O, respectively, see **Figure 3.21(c)**.²⁸⁵ The XPS analysis carried out after the electrochemical investigations were undertaken shows a negligible shift in the binding energies and area under the curves for nickel, manganese and oxygen as shown in **Figure 3.21(d, e, f)**. The before and after XPS spectrum confirms that no oxidation state changes occurred for each element present in the α -Ni(OH)₂ and MnO₂ in the hybrid material.

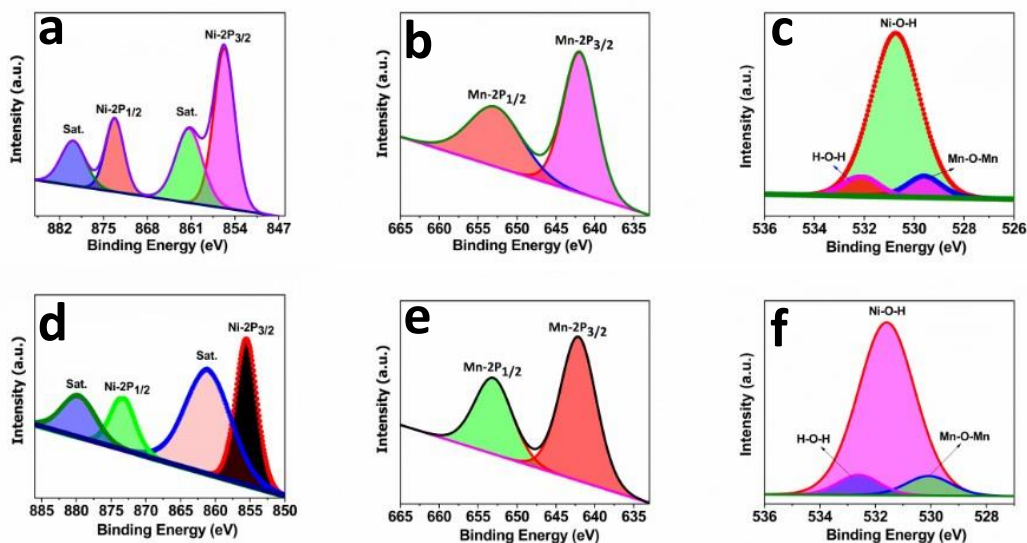


Figure 3.21. XPS profiles of α -Ni(OH)₂-MnO₂ hybrid before, a) Ni-2p, (b) Mn-1p, (c) O-1s, and after stability tests, d) Ni-2p, e) Mn-1p, f) O-1s.

3.3.4. SEM Analysis

Further, SEM images was obtained for all the materials to investigate the surface morphology as shown in **Figure 3.22**. α -Ni(OH)₂ shows a spherical shape particles with sizes ranges from 40 to 60 nm and very fine textured observed. NiO also demonstrate approximately spherical but the size increases up 50 nm to 60 nm due to the thermal annealing of the α -Ni(OH)₂ to NiO as depicted in **Figure 3.22(a, b)**. Also, the morphology of the particles observed in the image suggests that most of the particles are agglomerates of smaller individual moieties. Moreover, the MnO₂ nanoparticles were also identified as spherical in shape **Figure 3.22(c)**, with diameters of about 50 nm. The existence of these spherical aggregates suggests a homogeneous nucleation process of MnO₂ under the conditions employed.²⁸⁶ In addition, hybrid materials can be seen in **Figure 3.22(d)**. α -Ni(OH)₂ nanoparticles are decorated on the surface of the MnO₂ nanoparticles in the hybrid material. Hence, a degree of control over the morphology of the as-synthesised nanostructures could be exercised and subsequently optimised by applying this additional step in the solvothermal treatment. In **Figure 3.22(e)** the elemental mapping of hybrid nanostructures is presented, indicating the homogeneous distribution of manganese, nickel and oxygen. The mapping is presented at a lower magnification so as to provide an overview of the as-synthesised material and testifies to the uniformity of the distribution of each element in the sample.

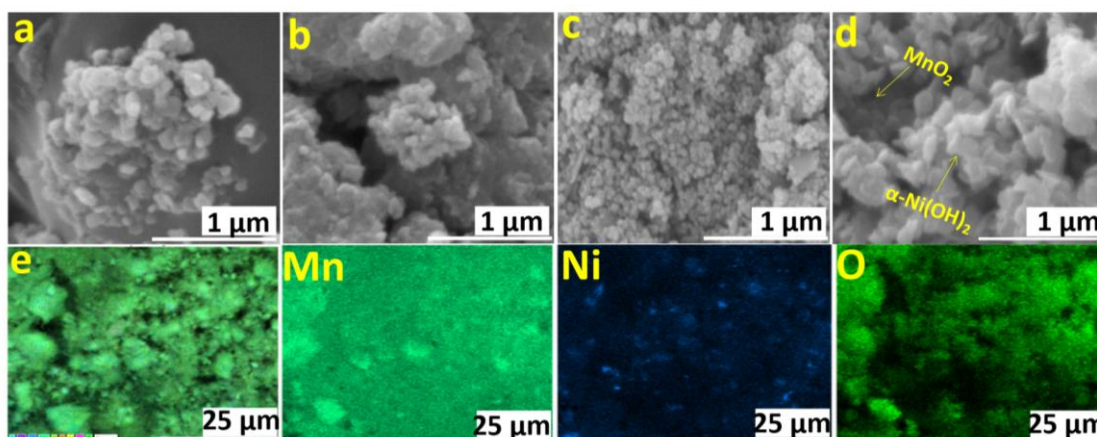


Figure 3.22. (a, b, c, d) on the top row are SEM of α -Ni(OH)₂, NiO, MnO₂, and α -Ni(OH)₂-MnO₂ hybrid, while on the bottom row are elemental mapping images of (e) α -Ni(OH)₂-MnO₂ nanostructures followed by images of the Mn, Ni and O distributions.

3.3.5. TEM and FE-SEM Analyses

High magnification TEM images of the as-prepared nanostructures **Figure 3.23** reveal that α -Ni(OH)₂ nanoparticles are spherical having diameters in 10 to 15 nm **Figure 3.23(a)** with a consistent size uniformity of the nanoparticles evidenced from the image. The image of NiO nanoparticles acquired by annealing of α -Ni(OH)₂ at 500 °C are presented in **Figure 3.23(b)**. A difference in the diameter of the nanoparticles compared to that of α -Ni(OH)₂ precursor examined and the structures are more agglomerated after calcination. Additionally, the morphology present in the Ni(OH)₂ material was not perfectly retained after thermal decomposition to NiO and it should be highlighted that many voids can be clearly seen, confirming the porosity of the extended structures formed by the NiO nanoparticles. Furthermore, the MnO₂ material demonstrates spherical morphology **Figure 3.23(c)**. From the image of the α -Ni(OH)₂-MnO₂ hybrid nanostructures **Figure 3.23(d)** that both the α -Ni(OH)₂ and MnO₂ materials are enlarged with respect to their starting material sizes. The hybrid hierarchical aggregates consist of ultrafine MnO₂ nanoparticles interconnected with particles of α -Ni(OH)₂, resulting in what has been predicted to be an attractive heterostructure for electrochemical applications.

FE-SEM images were collected for all of the fabricated electrodes after 5000 stability cycles and are in **Figure 3.23(e, f, g, h)**. The images reveal that no major changes have occurred in the morphology of the all the fabricated electrodes after undergoing stability

tests which indicates excellent structural stability. Furthermore, the images demonstrate that the nanoparticle films are completely intact at the surface of the nickel foam and do not leach out into the alkaline electrolyte solution. This supports what is observed visually i.e., that there are no major structural abnormalities indicative of damage observed in all fabricated electrodes after cyclic stability.

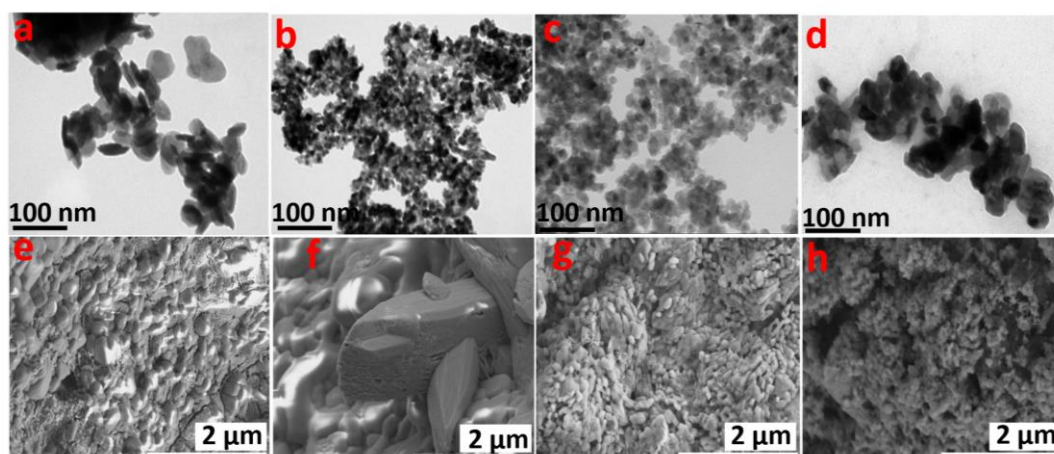


Figure 3.23. (a, b, c, d) TEM of α -Ni(OH)₂, NiO, MnO₂, and α -Ni(OH)₂-MnO₂ hybrid nanomaterials, (e, f, g, h) FE-SEM of α -Ni(OH)₂, NiO, MnO₂, and α -Ni(OH)₂-MnO₂ hybrid films after cyclic stability tests.

3.3.6. TGA Studies

The thermal changes that occur during the heat treatment of the as-prepared nanostructures between 20 and 800 °C were probed using TGA analysis, **Figure 3.24**. α -Ni(OH)₂ nanoparticles exhibit three principal mass loss steps. From 20 to 250 °C a mass loss of approx. 13% occurs because of water of crystallisation. The second region, which occurs from 260 to 550 °C and accounts for approximately 24% of the mass loss, represents the elimination of water for the conversion α -Ni(OH)₂ to NiO nanoparticles. The third mass loss of approx. 6% occurs in the region from 630 to 700 °C and is due to the oxidation of carbon to CO₂. The TGA profile of the NiO nanoparticles shows a continuous mass loss of approx. 27.6% in the 630 to 750 °C which can be assigned to the oxidation of carbon, present as organic material, to CO₂. Above 750 °C the TGA curve remains constant, which indicates that all carbon present has been converted to CO₂. Two mass loss events were detected for MnO₂ nanoparticles with the first, occurring under 100 °C and accounting for approx. 4% loss, is due to traces of moisture bound at the particle surface. The second mass loss occurs from 500 to 600 °C and is

most likely associated with the phase transformation of two MnO_2 units to form Mn_2O_3 . From the mass loss curve of nanocomposite, the mass loss of approx. 8% that occurs under 100 °C corresponds to the evaporation of surface adsorbed water. Moreover, approx. 16% loss that occurs between 110 and 440 °C can be ascribed to the conversion of $\alpha\text{-Ni(OH)}_2$ to NiO and the mass loss of approx. 26% that occurs from 480 to 530 °C in the nanocomposite material is related to transformation from MnO_2 to Mn_2O_3 .

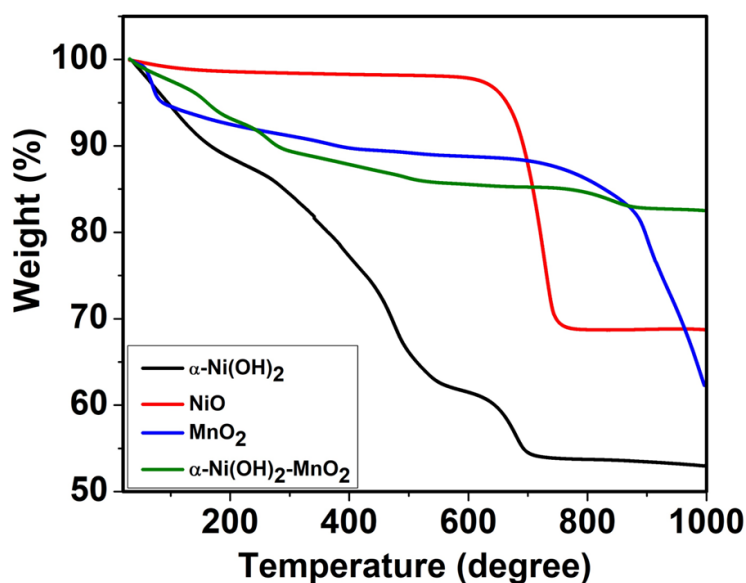


Figure 3.24. TGA spectra of the nanomaterials.

3.3.7. DSC Analysis

DSC was also undertaken, the profiles of which are presented in **Figure 3.25**. $\alpha\text{-Ni(OH)}_2$ nanoparticles display a broad peak in the region below 200°C which is related to the energy required to bring about the evaporation of strongly adsorbed water from the surface. In addition, $\alpha\text{-Ni(OH)}_2$ exhibits endothermic peak at 300°C with two, peaks at 340 °C and 415 °C. The temperature range of these endothermic peaks matches well with that of the mass loss corresponding to the $\alpha\text{-Ni(OH)}_2$ to form NiO. NiO nanoparticles do not show any observable thermal behaviour in their DSC profiles, which is to be expected as NiO is obtained by the the higher temperature decomposition of $\alpha\text{-Ni(OH)}_2$ at 500°C. For MnO_2 and nanocomposite two endothermic peaks can be observed in each of the DSC profiles from 50 °C to 450 °C. The lower temperature endothermic peak below 100 °C is related to the loss of absorbed water molecules incorporated during the synthesis. The broad band observed in the region from 300 °C to 340 °C is due to mass losses associated with the structurally associated water molecules.

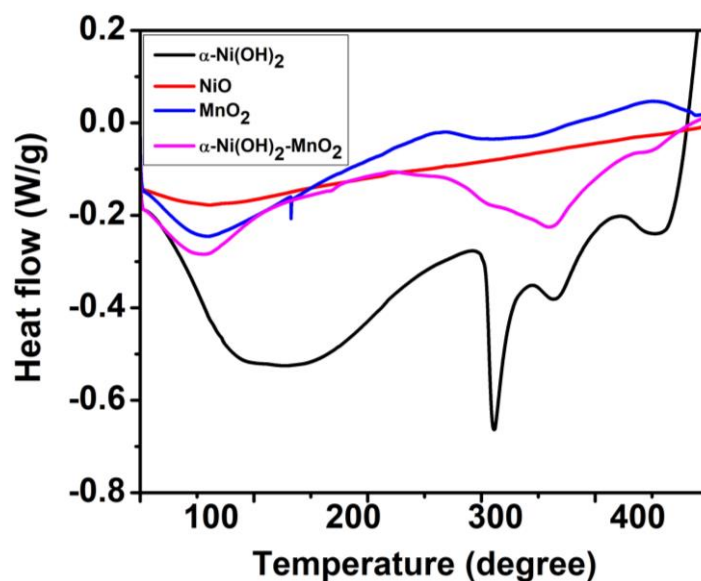


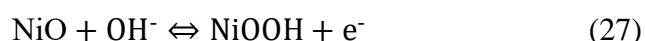
Figure 3.25. DSC spectra of the nanomaterials.

3.3.1. Electrochemical Investigation of Nanomaterials for Three Electrode Configuration

3.3.1.1. CV Investigation

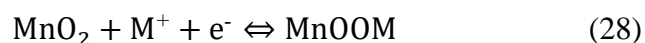
The fabricated electrodes were optimized in KOH, NaOH and LiOH. The CV measurements of each material along with the bare nickel foam were acquired at 20 mV s^{-1} in 3 M KOH, NaOH, and LiOH are depicted in **Figure 3.26(a, b, c)**. It is found that the area encompassed by the bare nickel foam curve (**a**) is negligible, demonstrating a significantly smaller charge storage capacity than the active materials. In contrast, the area enclosed within the CV curves increases in the different electrolytes in the order $\text{LiOH} < \text{NaOH} < \text{KOH}$, indicating good performance. Of the three electrolytes employed here, the active materials displayed a pair of redox peaks in KOH indicating its suitability for further electrochemical studies. The trends in the observed electrochemical performance can be explained by the hydrated ionic radii of the electrolyte cations. The K^+ (0.3 nm) has the smallest of the three hydrated ionic radii compared to Na^+ (0.4 nm) and Li^+ (0.6 nm).²⁸⁷ The solution resistance depends on the hydrated ionic radii, if radii is smaller than the resistance will be lower. Based on this observation it was resolved to undertake further electrochemical studies of the materials using KOH as the background electrolyte. The CV curves of $\alpha\text{-Ni(OH)}_2$ and NiO exhibit a typical battery-type behaviour with two broad redox peaks, as seen in **Figure 3.26(d, e)**. The increase in the scan rate leads to a gradual increase in the peak current, implying the presence of both ion and electron transfer in the electrode.²⁸⁸ The behaviour of the

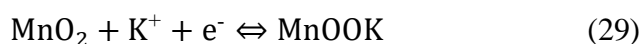
curves remains undisturbed with increasing scan rate indicating the excellent electrochemical stability of the active material. In case of NiO, both the peaks remain symmetrical even at higher scan rates which confirm the high reversibility of the redox reaction. The specific capacity and scan rate has reverse relation which demonstrate that electrolyte have enough time to enter into the inner of the electrode, results in the complete usage of the material. The reactions occurred at the surface of the electrode are represented by equations 26 and 27, respectively.



Additionally, the NiO nanomaterial exhibits more promising electrochemical properties as a supercapacitor electrode material compared with α -Ni(OH)₂ due to its fast electron/ion diffusion rate during the Faradaic reactions which is facilitated by the extremely porous morphology,^{254, 289} that results from this synthetic protocol and which enhances the feasibility for the material to be used in electrochemical applications. Evidence for this porosity was presented earlier in the TEM image of the NiO nanomaterial obtained by the thermal decomposition of the α -Ni(OH)₂ **Figure 3.26(b)**, where a closed interconnected network type structure could be observed. As a result of the porous nature of the nanostructure, ion diffusion is more likely and consequently provides a more effective matrix for energy storage.²⁹⁰ The presence of the larger pores allows for faster electrolyte ion transportation, while nanoscale sized undulations in the surface efficiently increases the available surface area for the redox reactions.²⁹¹ This results in a structure possessing excellent electrochemical performance and also accounts for its high rate of storage capacity.

The MnO₂ and α -Ni(OH)₂-MnO₂ nanocomposite were also elucidated for CV at same conditions as seen in **Figure 3.26(f, g)**. For MnO₂ nanoparticles, anodic peak arises at +0.41 V and that for α -Ni(OH)₂-MnO₂ at +0.39 V, indicating an oxidation process, whereas the cathodic peak for MnO₂ occurred at 0.30 V and that for α -Ni(OH)₂-MnO₂ at +0.16 V. The area under the CV curve of composite is comparatively higher than the MnO₂ which anticipated that composite is capable providing the higher capacity as in **Figure 3.26(g)**. The equation 28 and 29 can therefore be used to represent the pseudocapacitive processes of MnO₂ in aqueous solutions:





The high-performance of hybrid material in this study is likely because of the synergy exist MnO_2 and $\alpha\text{-Ni(OH)}_2$ nanoparticles. From the TEM images as in **Figure 3.26(d)**, $\alpha\text{-Ni(OH)}_2$ nanoparticles are uniformly spread over the MnO_2 , resulting the porous structure with high active sites where electrolyte adsorbed successfully. Such a situation can improve the electrochemical kinetics and ultimately lead to an enhancement of the specific capacity. As a result, the as-synthesised MnO_2 and $\alpha\text{-Ni(OH)}_2\text{-MnO}_2$ hybrid materials demonstrate improved supercapacitive performance.

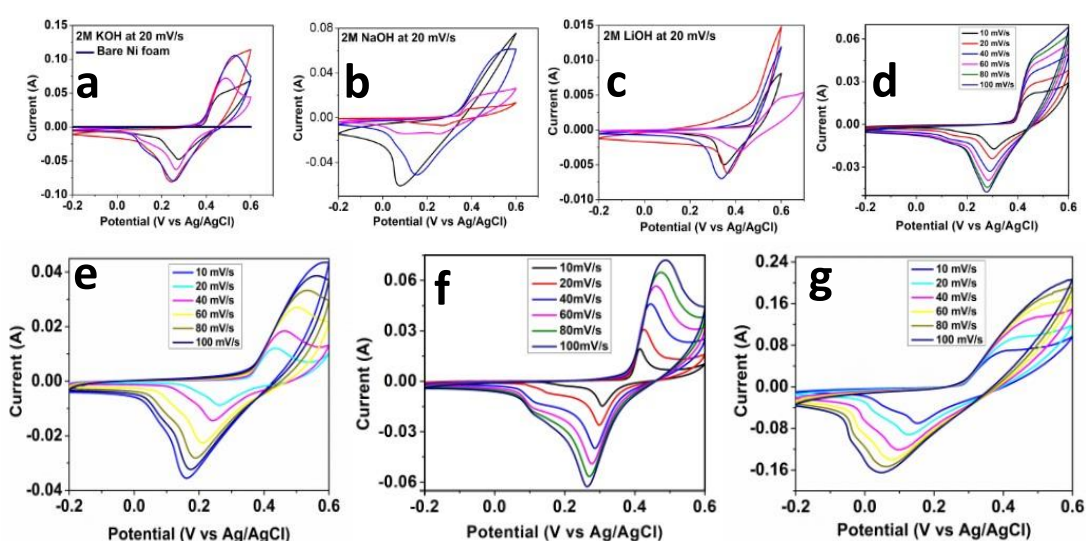


Figure 3.26. CV profiles of $\alpha\text{-Ni(OH)}_2$, NiO, MnO_2 , and $\alpha\text{-Ni(OH)}_2\text{-MnO}_2$ hybrid in (a) KOH, (b) NaOH, and (c) LiOH. CV profiles recorded at different scan rates in 2 M KOH of (d) $\alpha\text{-Ni(OH)}_2$, (e) NiO, (f) MnO_2 , and (g) $\alpha\text{-Ni(OH)}_2\text{-MnO}_2$ hybrid.

3.3.1.2. GCD, EIS, and Bode Phase Angle Studies

The GCD profiles of $\alpha\text{-Ni(OH)}_2$ and NiO nanoparticles are presented in **Figure 3.27(a, b)**. The non-linear discharge profiles indicate the battery-type behaviour of the materials.[66] In comparison to $\alpha\text{-Ni(OH)}_2$ nanoparticles the porous NiO showed the highest capacitance of 1450 F g^{-1} at 1 A g^{-1} . The specific capacitance values remain still high even at higher current densities such as 1085 F g^{-1} at 10 A g^{-1} . While the charge-storage behaviour is primarily a result of the battery-type nature of the materials, through the redox reactions that take place at interface, the increased specific capacity of the NiO nanomaterials is certain to be due to an enhancement by their distinctive morphology and high porosity. The electrolyte is expected to be readily absorbed by

this type of structure, which also creates a region that can store OH^- ions for the redox reaction. As a result, the interaction between the electrode and electrolyte is increased and consequently the diffusion lengths are reduced, resulting in an acceleration in ion diffusion in the charge-discharge process.²⁹²⁻²⁹³

MnO_2 and $\alpha\text{-Ni(OH)}_2\text{-MnO}_2$ hybrid materials were also employed for GCD analysis and the profiles are present in **Figure 3.27(c, d)**. The slope of the curves demonstrates the redox nature of the materials and in accordance with the CV profiles. However, at high current densities (e.g., 10 A g^{-1}), the curves show that the redox reactions are reversible and symmetric in nature, demonstrating the high-performance rate of both these electrodes. In comparison to pure MnO_2 nanoparticles, which have a specific capacitance of 470 F g^{-1} , the $\alpha\text{-Ni(OH)}_2\text{-MnO}_2$ hybrid achieved an even higher value of 1604.75 F g^{-1} revealing that the hybrid material has an increased performance over the pure MnO_2 nanoparticles. Moreover, it has been reported that MnO_2 nanoparticles can enable facile redox reactions and provide short diffusion lengths for electrons and ions.²⁹⁴ The combination of both materials produces a synergistic effect and this distinctive feature provides potential competitive benefits to $\alpha\text{-Ni(OH)}_2\text{-MnO}_2$ hybrid based supercapacitors. It has been reported that, at higher current densities, oxygen evolution reactions can take place in aqueous electrolyte during the charging process which impacts the GCD results,²⁹⁵ and therefore different potential windows for the CV and GCD investigations were chosen.

EIS curves and the equivalent circuit model shown as insets in **Figure 3.27(e)** Nyquist plots were drawn with straight line in the low frequency region indicate the capacitive behaviour and a semi-circle appeared in the high frequency region which can of charge transfer resistance of redox reaction.²⁹⁶ The bulk resistance is represented by the intercept with the real axis, and a shift to lower values indicates a decrease in the bulk resistance of the electrode. Here, NiO and $\alpha\text{-Ni(OH)}_2\text{-MnO}_2$ electrodes exhibit minimum charge-transfer and series resistance in the high-frequency region, implying that both materials have very facile charge-transfer and hence conductivity. Additionally, it can be seen from the enhancement in the conductivity that the performance of the hybrid materials has improved because of the integration of MnO_2 with $\alpha\text{-Ni(OH)}_2$. Bode plots were shown for each material in the **Figure 3.27(f)**. The phase angles lie in the range of -70° to -77° which is quite close to -90° , demonstrating the ideal capacitive nature of the materials. The specific capacity values, as estimated from GCD curves, are summarised in **table 5**.

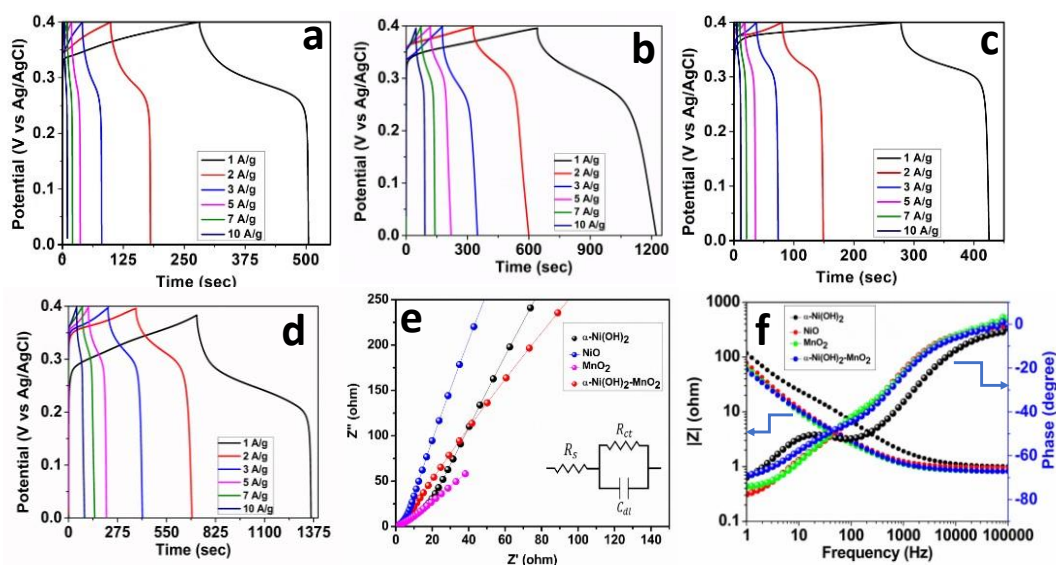


Figure 3.27. GCD profiles of (a) α -Ni(OH)₂ nanoparticles, (b) NiO nanoparticles, (c) MnO₂ nanoparticles and (d) α -Ni(OH)₂-MnO₂ hybrid. Nyquist plots (e) and Bode plots (f) for all four materials.

Table 3.5 Specific capacitance values of nanomaterials calculated from GCD in F g⁻¹.

Current density (A g ⁻¹)	1	2	3	5	7	10
α -Ni(OH) ₂	612.5	460	367.5	262.5	192.5	125
NiO	1450	1355	1286.25	1262.5	1184.75	1085
MnO ₂	470	370	285	250	192.5	150
α -Ni(OH) ₂ - MnO ₂	1604.75	1570	1445.25	1271.25	1225	1100

3.3.1.3. Quantitative Calculation of Surface and Diffusion Capacitance by Dunn's Method

The total capacity of the electrodes arising from the quantitative contribution from the surface and diffusion capacitances can be estimated using equation (11). The plots were drawn between $i(V)/v^{1/2}$ vs $v^{1/2}$ at fixed potentials and various scan rates from CV curves for NiO and α -Ni(OH)₂-MnO₂ as presented in **Figure 3.28(a, c)**. **Figure 3.28(b, d)** shows the overall percentage capacitance contribution from both the storage mechanisms. For NiO, the percentage diffusion contribution of the capacitance (90%) is higher than that of the surface capacity (10%) at lower scan rate (10 mV s⁻¹).

However, the diffusion capacitance contribution from the hybrid electrode is 85% and 15% surface capacitance at lower scan rate of 10 mV s^{-1} . At lower scan rate the diffusion capacitance accounted that the electrolyte ions have enough time to permeate into the inner surface of the electrode materials. On the other hand, diffusion capacitance decreases at higher scan rate where the capacitance arises from both the contribution from the surface and diffusion capacitances.

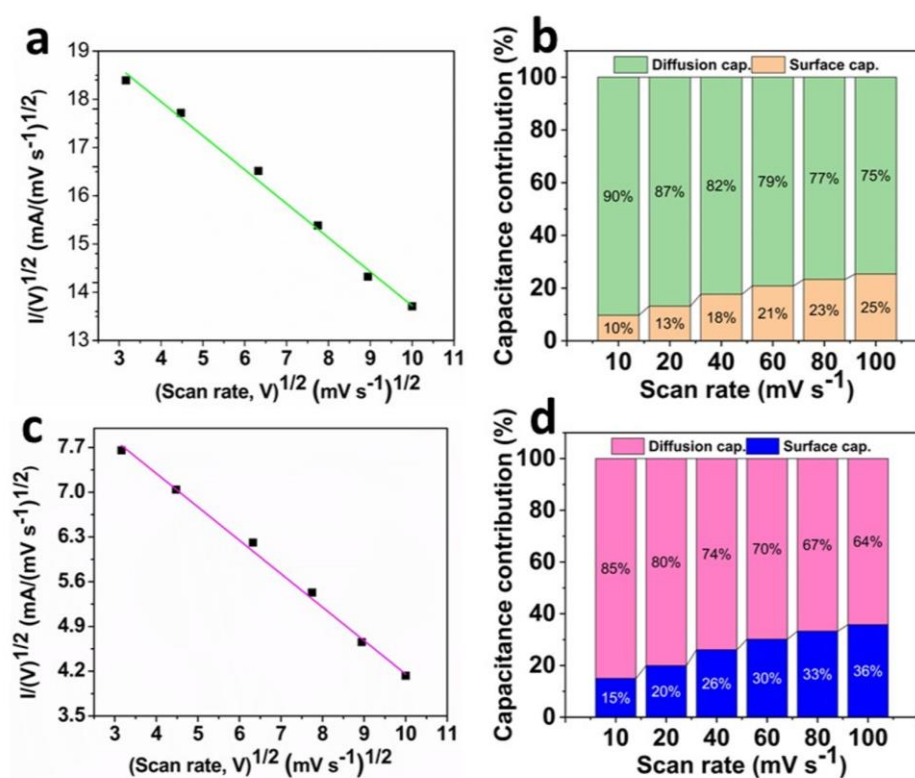


Figure 3.28. Quantitative capacitive analysis of NiO nanoparticles and α -Ni(OH)₂-MnO₂, (a, c) Plots of $(i/v^{1/2})$ vs $(v^{1/2})$, (b, d) Contribution of surface and diffusion capacitances.

3.3.2. Electrochemical Investigation of Nanomaterials for Symmetric Devices

3.3.2.1. CV Investigation

The nanomaterials were also tested within symmetric devices, using Whatman filter paper as a separator between both electrodes. CV analysis was conducted for the devices at different scan rates and the curves show that the operating potential window for the materials is in the range from 0 to 1 V, see **Figure 3.29(a, b, c, d)**. The behaviour of curves remains undisturbed at higher scan rates, indicating the characteristic capacitive behaviour of the symmetric devices.

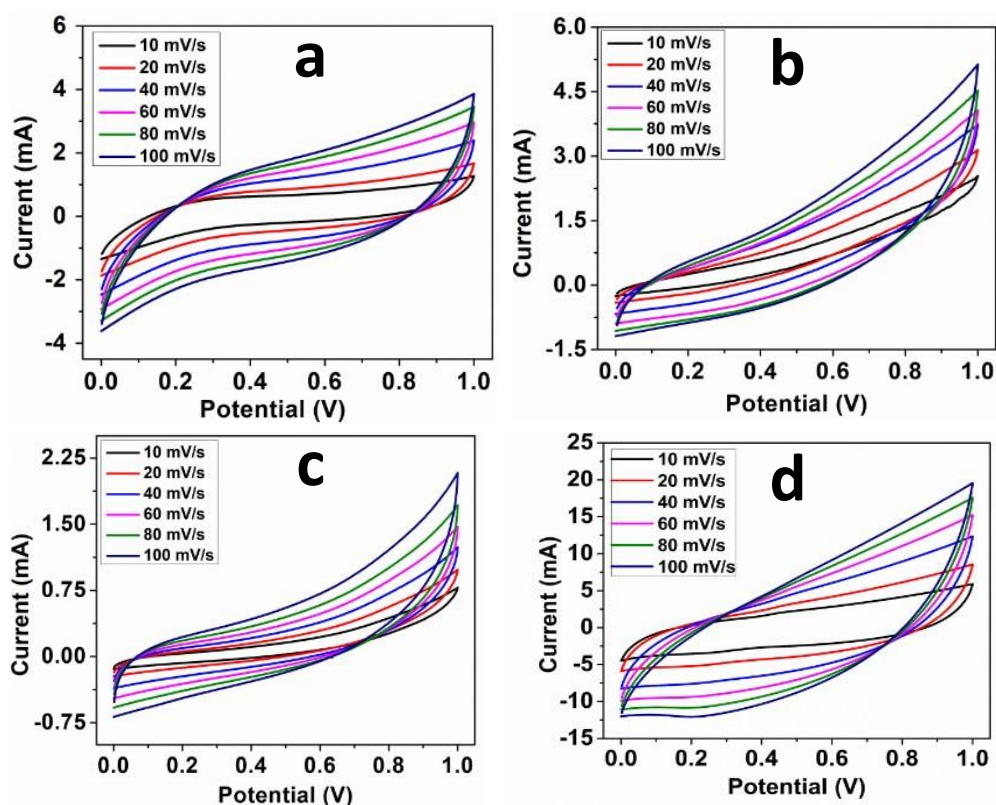


Figure 3.29. CV profiles of symmetric devices of a) α -Ni(OH)₂ nanoparticles, b) NiO nanoparticles, c) MnO₂ nanoparticles and d) α -Ni(OH)₂-MnO₂ hybrid.

3.3.2.2. GCD, Cyclic Stability, and Self-Discharge Studies

The GCD analysis was studied for each nanomaterial in a potential window of 0 to 1 V at 1 to 10 A g⁻¹, and displayed in **Figure 3.30(a, b, c, d)**. From the GCD curves, it is clear that the time required for charging and discharging of symmetric devices is higher for lower currents and lower for higher currents. This phenomenon occurs as at higher current densities the ions of the electrolyte are not being utilized over the total area of the electroactive sites of the electrode while at lower current densities ions are completely utilised to the bulk of the materials. A sudden voltage drop (IR drop) was observed in the GCD profiles because of combined ohmic resistances of electrolyte, and electrical contact of the devices. Also, the results indicate that the discharge curves exhibit the non-linear behaviour consistent with that of battery-type supercapacitors. The GCD curves of NiO and α -Ni(OH)₂-MnO₂ show a better rate capability and reversibility compared to other materials. The specific capacitance values calculated for NiO, and α -Ni(OH)₂-MnO₂ are 340 F g⁻¹ and 502 F g⁻¹ at 1 A g⁻¹, respectively. With the increase in the current densities the capacity values were found to follow the behaviour observed in three-electrode configuration again demonstrating that NiO

and α -Ni(OH)₂-MnO₂ electrodes exhibit good symmetric device performance. The capacity retention as a function of number of cycles is presented in **Figure 3.30(e)**. The fabricated devices were tested over 5000 cycles after all electrochemical studies had been completed. The symmetric devices for each nanomaterials showed a capacity retention of 53, 65, 95 and 72% respectively, indicating their excellent stability. The coulombic efficiency was determined for every cycle of GCD analysis as shown in **Figure 3.30(e)**. When tested for 5000 cycles, all materials showed extremely high coulombic efficiency, indicating that the electrodes are exceedingly reversible. The long charging and discharging times exhibited by the materials are a result of their outstanding structural stability.

Self-discharging, in which the electrodes were first charged to a fixed potential, the power turned off and the open circuit potential measured with respect to time was assessed. **Figure 3.30 (f)** demonstrates the comparative self-discharge potential profiles of each electrode initially charged at 1.0 V. From the self-discharge profiles that the hybrid material has the slowest discharge rate while the NiO has the quickest. The NiO curve reaches a constant value of 0.36 V after a very long discharge time.

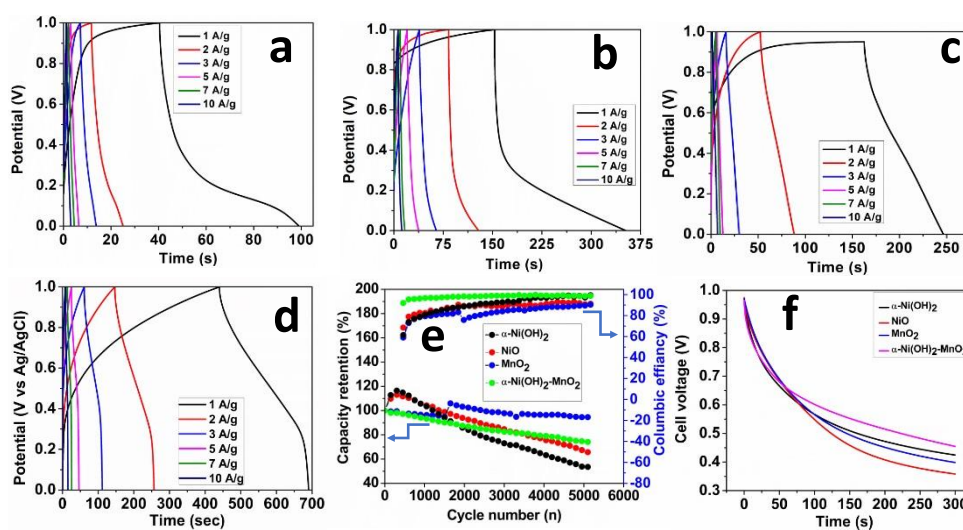


Figure 3.30. GCD analysis of symmetric devices a) α -Ni(OH)₂ nanoparticles, b) NiO nanoparticles, c) MnO₂ nanoparticles, d) α -Ni(OH)₂-MnO₂ hybrid, (e) Cyclic stability and coulombic efficiency and (f) self-discharge curves.

Nyquist plots, recorded in three-electrode configuration, showed a similar behaviour as can be seen from **Figure 3.31(a)**. The NiO and α -Ni(OH)₂-MnO₂ have a very low Warburg impedance and charge transfer resistance leading to an increase in conductivity and faster electron transfer. However, NiO and α -Ni(OH)₂-MnO₂ have the

highest energy densities of 47.21 Wh kg⁻¹ and 69.72 Wh kg⁻¹ at power densities of 1 kW kg⁻¹ respectively at 1 A g⁻¹ as in **Figure 3.31(b)**. These values illustrate the high-rate capability of both devices. The performance of NiO and α -Ni(OH)₂-MnO₂ based symmetric devices clearly demonstrate a sizable potential to work across a wide potential window even at higher energy densities making these materials very promising candidates for supercapacitor applications.

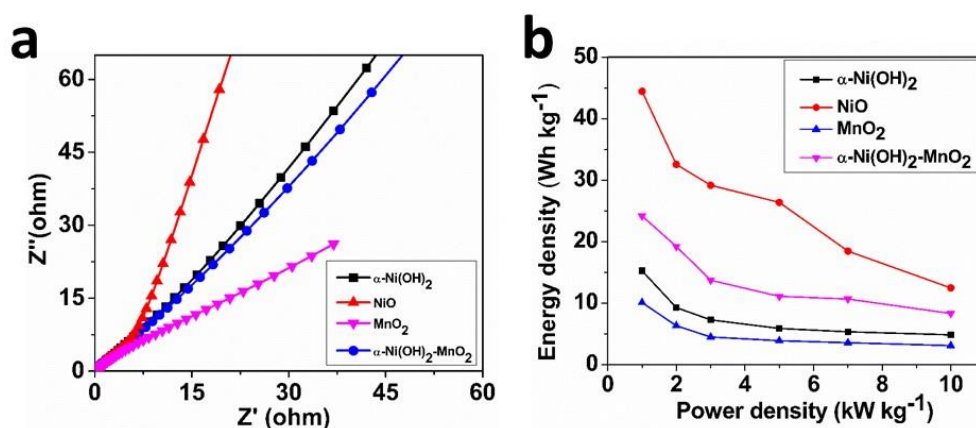


Figure 3.31. (a) Nyquist plots after cyclic stability test, (b) Ragone plots of fabricated symmetric devices.

Part-04

3.4. Colloidally Synthesized V₂O₅ Based Nanocomposites Electrode Materials for High-Performance Electrochemical Supercapacitors

3.4.1. PXRD Studies

The X-ray diffraction analysis of both the as-prepared V₂O₅ nanoparticles and their composite was conducted as depicted in **Figure 3.32(a)**. The distinct peaks observed in the pure V₂O₅ samples closely correspond to the orthorhombic phase (JCPDS Card No. 41-1426). Notably, there were no indications of impurity peaks in the X-ray diffraction pattern. The sharp intensity of the diffraction peaks suggests being high crystallinity of the materials. Interestingly, the conventional peaks of GO and rGO in the composites were not appeared at their respective positions which possibly due to the uniform formation of V₂O₅ nanoparticles on sheets displayed.

3.4.2. Raman Analysis

Raman spectra were recorded to study the further structural properties of as-prepared V_2O_5 , and nanocomposites as displayed in **Figure 3.32(b)**. V_2O_5 nanoparticles exhibited the bands at 143, 193, 285, 404, 478, 483, 525, 703, and 992 cm^{-1} which are the characteristic modes of V_2O_5 . The peaks appearing at 143, 193 cm^{-1} are corresponding to the relative motion of the V_2O_5 layers with respect to each other which confirms the layered structure and good crystallinity of the V_2O_5 . The peaks assigned at 285, 404 cm^{-1} corresponding to V=O bending mode while two less intense peaks at 478, 483 cm^{-1} ascribed to the bending vibration of V-O-V mode. The observed bands at 525 cm^{-1} are a result of the stretching and bending modes involving V-O bonds. Additionally, the distinctive peak at 992 cm^{-1} attributed to the stretching mode of V=O bonds. Furthermore, in both the nanocomposite samples, two broad bands were evident at 1319 cm^{-1} and 1585 cm^{-1} , corresponding to the D and G bands of G and rGO (graphene and reduced graphene oxide), respectively. The G band signifies the in-plane bond-stretching motion of the two carbon sp^2 atoms (the E_{2g} phonons), while the D band arises from the presence of sp^3 carbon atoms or k-point phonons of A_{1g} symmetry.

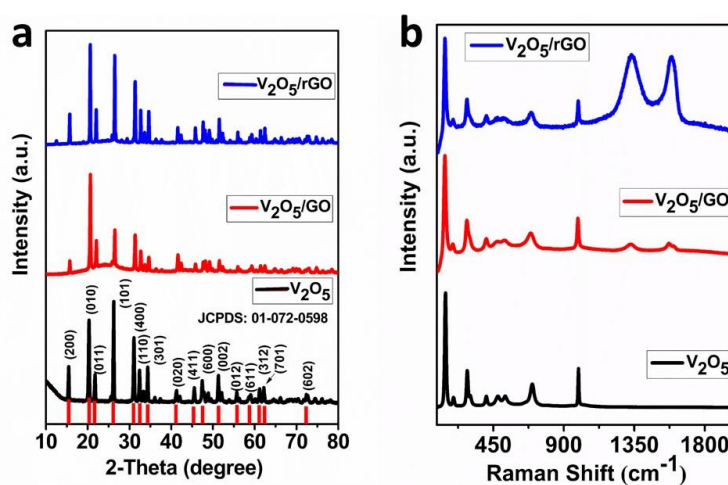


Figure 3.32. (a) PXRD patterns of V_2O_5 nanoparticles (black), V_2O_5/GO nanocomposite (red), V_2O_5/rGO nanocomposite (blue), (b) Raman spectra of nanostructures V_2O_5 nanoparticles (black), V_2O_5/GO nanocomposite (red), V_2O_5/rGO nanocomposite (blue).

3.4.3. SEM Studies

Furthermore, pure V_2O_5 and composites morphology was confirmed by SEM as presented in **Figure 3.33**. The SEM micrographs depicted that the V_2O_5 nanoparticles are mixed irregular to spherical morphology as in **Figure 3.33(a)**. While the average diameter of the particles ranges from 15 to 20 nm. The morphology of V_2O_5/GO nanocomposite was presented in **Figure 3.33(b)**. The image reveals that the V_2O_5 nanoparticles were successfully attached to GO sheets. For the V_2O_5/rGO nanocomposite, images are displayed in **Figure 3.33(c, d)**. The images showed that the particles are grown on rGO sheets. The nanoparticles are approximately spherical in shape after the sonication and drying processes but most of them get agglomerated due to stacking with each other.

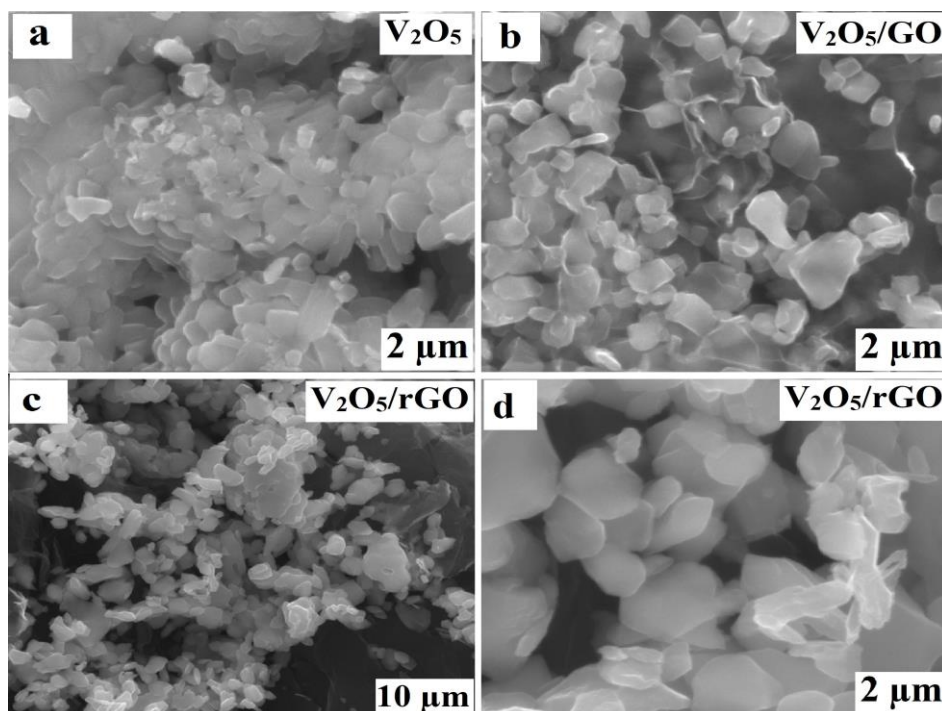


Figure 3.33. SEM micrographs of nanostructures (a) V_2O_5 nanoparticles, (b) V_2O_5/GO composite, (c, d) V_2O_5/rGO composite.

3.4.4. Elemental Mapping Analysis

Figure 3.34(a, e) illustrates the elemental mapping of the V_2O_5/GO nanocomposite which demonstrates that the vanadium, oxygen, and carbon are homogeneously distributed. The mapping was recorded at low magnification to represent the homogeneous spreading of each element on GO sheets. The elemental composition and purity of the nanocomposite was estimated by EDX investigations as shown in **Figure 3.34(f)**. The EDX demonstrates the predominant peaks of V, O and

C, respectively. Moreover, the existence of some minute impurity peaks of Cu which is not in real number and may be raised due to the instrumental error.

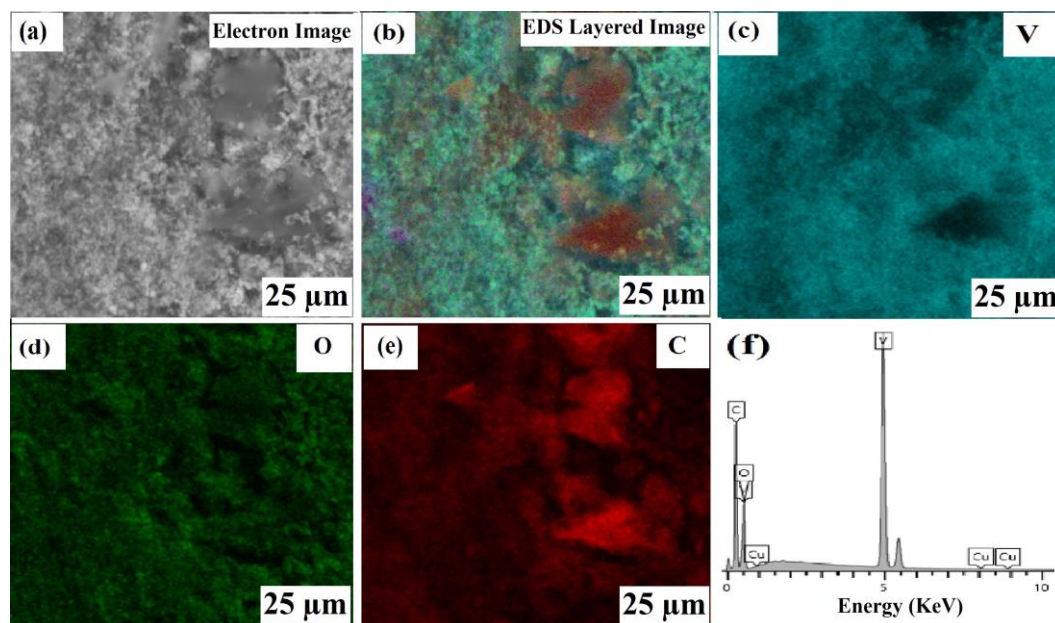


Figure 3.34. Elemental mapping images and EDX spectrum of V_2O_5/GO composite.

3.4.5. TEM Studies

To have a better understanding of the morphology, the as-prepared V_2O_5 nanoparticles were analysed by TEM analysis as shown in **Figure 3.35**. The high and low magnification images are presented in **Figure 3.35(a, b)**. The well-defined spherical particles were observed with average diameter in the ranges 5 to 7 nm. As the nanoparticles were prepared at an elevated temperature due to which it starts to get agglomerate as shown in the low magnification image. On the other hand, in both the composite, it clearly observed the V_2O_5 particles are homogeneously distributed and grown on GO and rGO sheets as in **Figure 3.35(c, d)**. The particle size is about 5 to 7 nm, which is approximately similar to that of a pure V_2O_5 sample.

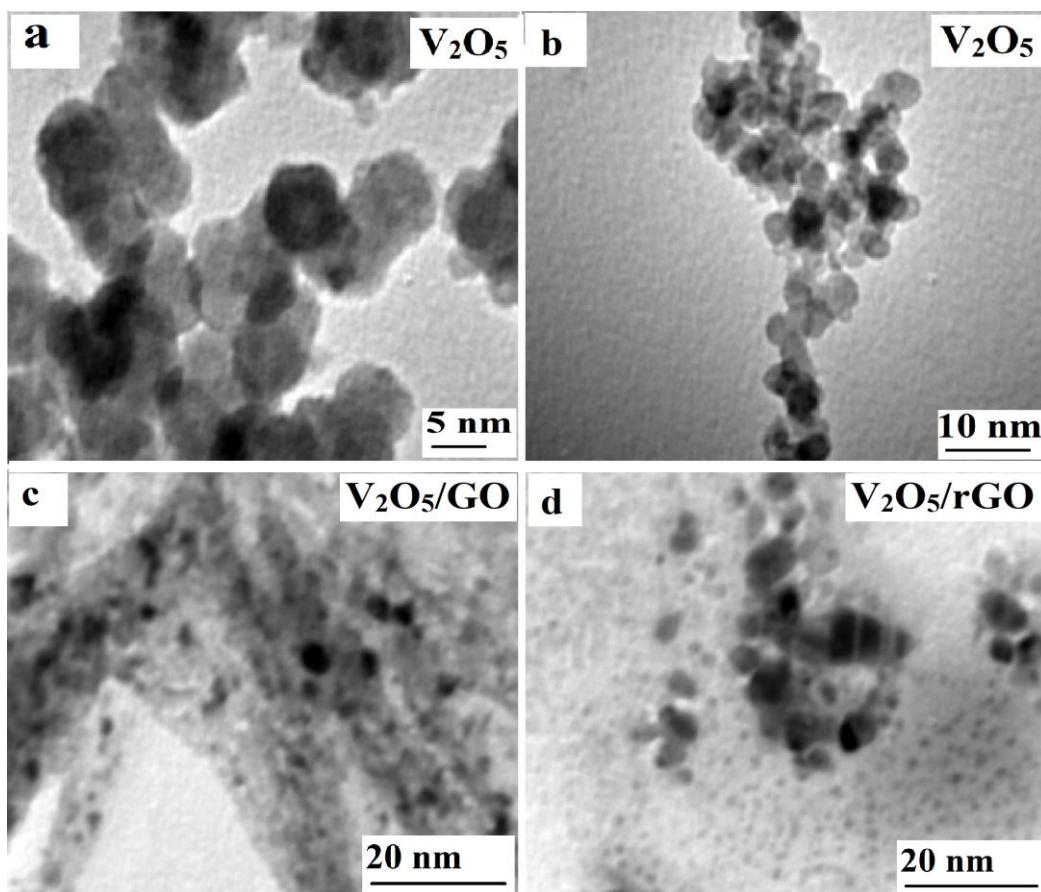


Figure 3.35. TEM images of nanostructures (a, b) V₂O₅ nanoparticles, (c) V₂O₅/GO composite, (d) V₂O₅/rGO composite.

3.4.1. Electrochemical Investigation of Nanocomposites for Three Electrode Configuration

3.4.1.1. CV and GCD Investigations

The comparative electrochemical behaviour of colloiddally synthesized V₂O₅, V₂O₅/GO, and V₂O₅/rGO nanomaterials were studied by CV in a three-electrode setup with potential window of -0.2 to +0.6 V in 2 M KOH aqueous electrolyte. The area under the CV curve of pristine and V₂O₅/GO is less than the V₂O₅/rGO which indicate the more storage capacity of this composite, indicating its superior energy storage capacity²⁹⁷ as seen in **Figure 3.36(a)**. This enhancement in performance can be primarily attributed to the inclusion of rGO, which substantially enhances the overall conductivity of the composite due to its low-resistance properties.²⁹⁸ The CV curves demonstrated pair of redox peaks for V₂O₅/rGO nanocomposite, reflects the capacitive nature of the material and indicates the Faradaic reactions. With enhancement in the scan rate, the behaviour of the redox peaks remains symmetric, confirmed the

exceptional reversibility of the electrode material.²⁹⁸ In EDLCs, the redox reactions result in relatively low current peaks, while Faradaic reactions showed high current peaks in battery-type materials.²⁹⁹ Consequently, the V₂O₅/rGO suggests a battery-type capacitive behaviour, primarily driven by Faradaic reactions occurring at the electrode-electrolyte interface. There are no distortions observed in the CV profiles that indicates the efficiency of V₂O₅/rGO in facilitating electron transport with minimal equivalent series resistance. However, it is worth mentioning that a slight shift in the redox peaks is observed as the scan rates increase, which could be attributed to internal resistance within the system.²⁹⁸⁻²⁹⁹ However, the CV profiles of V₂O₅, V₂O₅/GO and V₂O₅/rGO materials were conducted at various scan rates which demonstrate the similar battery-type behaviour as observed for V₂O₅/rGO nanocomposite shown in **Figure 3.36(b, c, d)**, respectively.

Galvanostatic charge-discharge analysis was performed for V₂O₅, V₂O₅/GO, and V₂O₅/rGO nanomaterials to test the electrochemical behaviour as shown in **Figure 3.36(e, f, g)**. The behaviour of the discharge profiles shows the battery-type nature of the materials which supports the CV results. The highest specific capacitance value calculated for V₂O₅/rGO is 1190 F g⁻¹ while for pristine V₂O₅ and V₂O₅/GO are 696.63 and 1083.34 F g⁻¹ at current density of 1 A g⁻¹, respectively. These values suggest the high-rate capability of the V₂O₅/rGO nanocomposite. Moreover, the V₂O₅/rGO electrode material demonstrated an enhanced specific capacitance because of the synergy between the rGO sheets and V₂O₅ nanoparticles.³⁰⁰ Firstly, rGO sheets help in improving the conductivity of the electrode as well as double-layer capacitance. Secondly, V₂O₅ nanoparticles are uniformly distributed over rGO sheets which utilize effectively their pseudocapacitance.²⁹⁸ Thirdly, rGO sheets also prevented the V₂O₅ from disintegration but also buffer the strain appeared due to the volume expansion during the charge-discharge analysis.³⁰¹ Finally, the quick electron transfer was assisted by the strong attraction between the materials, which improved the electrochemical performance.³⁰² The specific capacitance values decrease with the increase in current density and attributed to the diffusion effect which ultimately limits the movements of the electrolyte ions. Consequently, cause the incomplete usage of the electrode material.³⁰³ When the V₂O₅/rGO tested at over a range of current densities from 1 to 10 A g⁻¹, it outperformed than that of pristine V₂O₅ and V₂O₅/rGO materials. For instance, at 1 A g⁻¹ the obtained capacitance value is 1190 F g⁻¹ while at 10 A g⁻¹ is 483.62 F g⁻¹

¹, respectively. **Table 3.6** summarised the specific capacitance values calculated at various current densities.

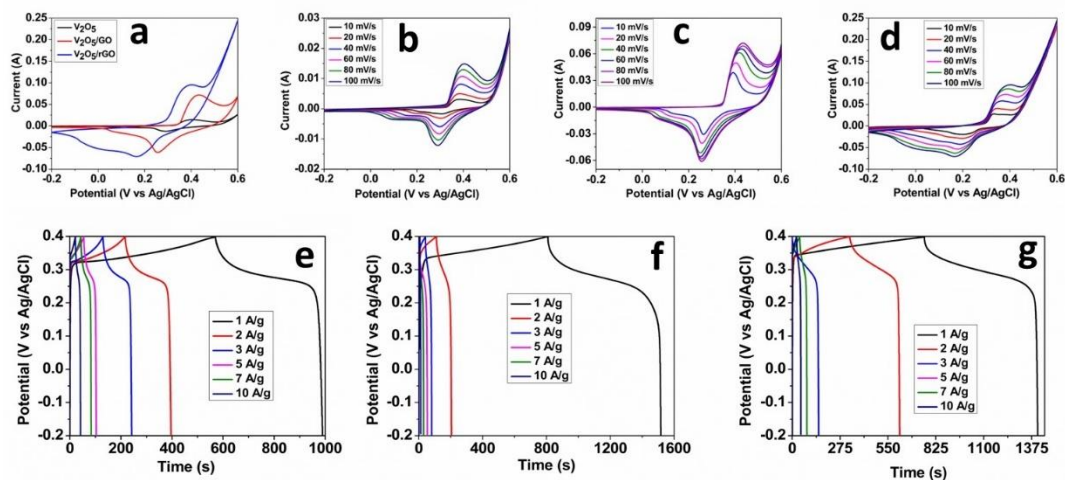


Figure 3.36. a) CV profiles a) V_2O_5 nanoparticles, b) V_2O_5 /GO nanocomposite, c) V_2O_5 /rGO nanocomposite, and GCD profiles of d) V_2O_5 nanoparticles, e) V_2O_5 /GO nanocomposite, f) V_2O_5 /rGO nanocomposite.

Table 3.6 Specific capacitance values of nanomaterials calculated from GCD in $F g^{-1}$.

Current density ($A g^{-1}$)	1	2	3	5	7	10
V_2O_5	696.63	603.32	570	466.71	400	316.53
V_2O_5 /GO	1083.3 4	973	705	583.53	490	464.24
V_2O_5 /rGO	1190	963.41	780	525	501	483.62

Conclusions

In summary, a direct hydrothermal protocol was adopted for the synthesis of nickel-based hydroxide/oxide nanocomposites grown on reduced graphene oxide (rGO). The materials were employed as a high-performance active layer for advanced supercapacitors. Ni(OH)₂/rGO and NiO/rGO nanocomposites demonstrated a high specific capacitance of 1255.12 and 636.84 F g⁻¹ at 10 mV s⁻¹ obtained from CV curves while 1092.5 and 1070 F g⁻¹ estimated from GCD at 1 A g⁻¹, respectively. Subsequently, symmetric devices with a broad potential window of 1.4 V for both materials were also fabricated. Symmetric devices delivered the maximum specific capacitance of 115.71 and 80.28 F g⁻¹ at 1 A g⁻¹ with an energy density of 31.5 Wh Kg⁻¹ and 22 Wh kg⁻¹ at power density of 1.4 kW kg⁻¹ which indicates the high-rate capability of the devices. The devices have maximum capacity retention of 81% and 93%, when tested for 1000 discharge cycles at 3 A g⁻¹ showing high cycle stability. The superlative performance of nanocomposites can be attributed to the synergistic effects they exhibit, demonstrating that they are appealing electrode materials for supercapacitor applications.

In the second part, we present a successful synthesis of heteroatom (N, S) co-doped TiO₂ decorated with Ag nanoparticles using a direct combustion approach. These materials serve as a high-performance active layer for advanced battery-type supercapacitors. Among all the investigated materials, the N,S co-doped TiO₂ nanoparticles and Ag/N,S co-doped TiO₂ nanocomposite exhibited impressive specific capacitances of 360 and 480 F g⁻¹ at a current density of 1 A g⁻¹. Moreover, we employed Ag/N,S co-doped TiO₂ nanocomposite as symmetric supercapacitor in a wide potential window of -1 to 1 V. The symmetric device demonstrated a specific capacitance of 183 F g⁻¹ at 3 A g⁻¹ with an energy density of 105 Wh kg⁻¹ at a power density of 6 kW kg⁻¹. One of the most promising aspects of this study is the high cyclic stability of the device, with the highest capacity retention of 80% when tested for 3000 discharge cycles at 3 A g⁻¹. The improved electrochemical performance of Ag nanoparticle decorated N,S co-doped TiO₂ structure confirms the synergistic behavior of each component in the composite. These results indicate the remarkable durability of the device. Additionally, the materials used in this work are environmentally friendly, making them attractive candidates for battery-type supercapacitors.

In the third part, surfactant-free and scalable methodology for the synthesis of spherical nanoparticles of Ni(OH)₂, NiO, and Ni(OH)₂-MnO₂ hybrid material employing the polar, aprotic solvent, Dimethylformamide (DMF) has been developed. An extension of the methodology to include a surfactant-coated metal oxide nanomaterial (MnO₂) has also been presented for comparison. Of the investigated electrode materials in a three-electrode configuration, NiO and α -Ni(OH)₂-MnO₂ exhibit the highest specific capacitance of 1450 F g⁻¹ and 1604.75 F g⁻¹ at a current density of 1 A g⁻¹, respectively. To evaluate the electrochemical performance of the materials synthesized using this methodology for electrochemical capacitor applications, symmetric devices with a wide operating potential window of 1 V, were fabricated. The NiO and α -Ni(OH)₂-MnO₂ based symmetric devices delivered maximum specific capacitances of 340 F g⁻¹ and 502 F g⁻¹ at a current density of 1 A g⁻¹ and 47.21 Wh kg⁻¹ and 69.72 Wh kg⁻¹ at a power density of 1 kW kg⁻¹, clearly demonstrating the high-rate capability of the symmetric devices. Devices based on NiO and α -Ni(OH)₂-MnO₂ also possess a high cycle stability with maximum capacity retentions of 65% and 72% respectively after 5000 charge-discharge cycles at 3 A g⁻¹.

In the final part, the successful synthesis of V₂O₅ nanoparticles, V₂O₅/GO, and V₂O₅/rGO was achieved through a newly developed colloidal method, meticulously controlling the reaction parameters with a single molecular precursor. The resulting V₂O₅ and its composites were assessed for their potential in battery-type supercapacitors. In three-electrode configurations, all materials demonstrated outstanding specific capacitance performance, with V₂O₅/rGO exhibiting the highest value at 1190 F g⁻¹ under a current density of 1 A g⁻¹. These findings suggested the high-rate capability of the fabricated electrodes. Notably, the environmentally friendly nature of the materials used in this study positions them as attractive candidates for battery-type supercapacitors.

Future Perspectives

In recent years, storage technologies have attracted significant interest of numerous scientists and engineers from various disciplines such as chemistry, physics, electrochemistry, material science, and engineering. These experts have employed a wide range of characterization techniques to make substantial advancements in understanding the diverse physical and chemical phenomena related to energy storage. While considerable progress has been made in the development of electrochemical energy storage materials. Additionally, the supercapacitors are still in the early stages of their evolution. The diverse variety of materials have highlighted the potential for further innovation in this area. Therefore, by carefully investigating the materials, it is possible to achieve energy and power densities that surpass the capabilities of both lithium-ion batteries and traditional electric double-layer capacitors (EDLCs). The ongoing developments in supercapacitor systems required intense research efforts focused on understanding the electrochemical processes that contribute to improve the electrode properties. Additionally, state-of-the-art architectures will be crucial for the creation of high-performance energy storage devices. Notably, few ways have been investigated, until now, which make this field more enticing and promising for future. The impact of these advancements is expected to extend well into the coming years.

List of Publications Added from this Thesis

1. **Hussain, M. N.;** Inayat, A.; Ansir, R.; Naveed, A.; Abbas, S. M.; Haider, A.; Shah, S. M., Probing the Synergy of Ni(OH)₂/NiO Nanoparticles Supported on rGO for Battery-Type Supercapacitors. *Energy Technol.* **2024**, *12* (2), 2300854.
2. **Hussain, M. N.;** Naveed, A.; Inayat, A.; Bilal, M.; Haider, A.; Shah, S. M., Investigating the Impact of Ag Nanoparticles on N and S Co-Doped TiO₂ for Battery-Type Supercapacitor Application. *ChemistrySelect* **2023**, *8* (48), e202303224.
3. **Hussain, M. N.;** Naveed, A.; Inayat, A.; Shah, S.; Ihsun, M.; Haider, A.; Abbas, S.; Hickey S., Versatile Synthesis of Metal Oxide Nanoparticles Using Polar, Aprotic Solvents to Fabricate High-Performance Electrode Materials for Advanced Supercapacitors. *Angew. Chem*, 2024, (under review).
4. **Hussain, M. N.;** Naveed, A.; Shah, S.; Ihsun, M.; Haider, A.; Hickey, S., Colloidally Synthesized V₂O₅ Based Nanocomposites Electrode Materials for High-Performance Electrochemical Supercapacitors. 2024, (submission in process).

Other Publications

1. **Hussain, M. N.;** Shah, S. M.; Shabir, G.; Bhatti, A. S.; Badshah, A.; Bahadur, A.; Saboor, A.; Iqbal, S.; Khan, K., Iron and nickel doped tin (IV) oxide nanosheets: synthesis, characterization and applications in hybrid solar cells. *Physica E Low Dimens. Syst. Nanostruct.* **2019**, *108*, 307-316.
2. Ahmad, M.; Inayat, A.; **Hussain, M. N.;** Khan, A.; Alam, M.; Sultan, M.; Abbas, S. M., Graphene supported In₂S₃ nanostructure as electrode material for lithium sulfur batteries and supercapacitors. *Mater. Today Sustain.* **2024**, *25*, 100631.
3. Ansir, R.; Shah, S. M.; Ullah, N.; **Hussain, M. N.**, Performance of pyrocatechol violet and carminic acid sensitized ZnO/CdS nanostructured photoactive materials for dye sensitized solar cell. *Solid State Electron.* **2020**, *172*, 107886.
4. Ullah, N.; Shah, S. M.; Hussain, H.; Ansir, R.; **Hussain, M. N.**, Pyrocatechol violet sensitized Ho-TiO₂/ZnO nanostructured material: as photoanode for dye sensitized solar cells. *Mater. Res. Express.* **2020**, *7* (3), 035003.

5. Jabeen, U.; Shah, S. M.; **Hussain, M. N.**; Ali, A.; Khan, S. U., Synthesis, characterization, band gap tuning and applications of Cd-doped ZnS nanoparticles in hybrid solar cells. *J. Photochem. Photobiol.* **2016**, *325*, 29-38.
6. Bahadur, A.; Saeed, A.; Shoaib, M.; Iqbal, S.; Bashir, M. I.; Waqas, M.; **Hussain, M. N.**; Abbas, N., Eco-friendly synthesis of magnetite (Fe₃O₄) nanoparticles with tunable size: dielectric, magnetic, thermal and optical studies. *Mater. Chem. Phys.* **2017**, *198*, 229-235.
7. Farooq, Z.; Ali, R.; Ahmad, A. u.; Yaseen, M.; Mahmood, M. H.; Fahad, M.; **Hussain, M. N.**; Rehan, I.; Khan, M. Z.; Ramiza, Electron number density conservation model combined with a self-absorption correction methodology for analysis of nanostructure plasma using laser-induced breakdown spectroscopy. *Appl. Opt.* **2020**, *59* (8), 2559-2568.
8. Farooq, Z.; Ali, R.; Qurashi, U. S.; Mahmood, M. H.; Yaseen, M.; Qayyum, M. A.; **Hussain, M. N.**; Shah, S. M.; Jan, T., Spectroscopic studies of laser produced plasma of doped nano-structured material by laser induced breakdown spectroscopy. *Phys. Plasmas.* **2018**, *25* (9).

References

1. Al-Sharafi, A.; Sahin, A. Z.; Ayar, T.; Yilbas, B. S., Techno-economic analysis and optimization of solar and wind energy systems for power generation and hydrogen production in Saudi Arabia. *Renewable Sustainable Energy Rev.* **2017**, *69*, 33-49.
2. Olabi, A.; Onumaegbu, C.; Wilberforce, T.; Ramadan, M.; Abdelkareem, M. A.; Al-Alami, A. H., Critical review of energy storage systems. *Energy* **2021**, *214*, 118987.
3. Ruth, M. F.; Zinaman, O. R.; Antkowiak, M.; Boardman, R. D.; Cherry, R. S.; Bazilian, M. D., Nuclear-renewable hybrid energy systems: Opportunities, interconnections, and needs. *Energy Convers. Manag.* **2014**, *78*, 684-694.
4. Fasihi, M.; Weiss, R.; Savolainen, J.; Breyer, C., Global potential of green ammonia based on hybrid PV-wind power plants. *Appl. Energy* **2021**, *294*, 116170.
5. Gan, Z.; Yin, J.; Xu, X.; Cheng, Y.; Yu, T., Nanostructure and advanced energy storage: elaborate material designs lead to high-rate pseudocapacitive ion storage. *ACS nano* **2022**, *16* (4), 5131-5152.
6. Tie, S. F.; Tan, C. W., A review of energy sources and energy management system in electric vehicles. *Renewable Sustainable Energy Rev.* **2013**, *20*, 82-102.
7. Sun, X.; Li, Z.; Wang, X.; Li, C., Technology development of electric vehicles: A review. *Energies* **2019**, *13* (1), 90.
8. Hadjipaschalis, I.; Poullikkas, A.; Efthimiou, V., Overview of current and future energy storage technologies for electric power applications. *Renewable Sustainable Energy Rev.* **2009**, *13* (6-7), 1513-1522.
9. Li, W.; Garg, A.; Xiao, M.; Peng, X.; Le Phung, M. L.; Tran, V. M.; Gao, L., Intelligent optimization methodology of battery pack for electric vehicles: A multidisciplinary perspective. *Int. J. Energy Res.* **2020**, *44* (12), 9686-9706.
10. Lu, Z.; Chang, Z.; Zhu, W.; Sun, X., Beta-phased Ni(OH)₂ nanowall film with reversible capacitance higher than theoretical Faradic capacitance. *Chem. Commun* **2011**, *47* (34), 9651-9653.

11. May, G. J.; Davidson, A.; Monahov, B., Lead batteries for utility energy storage: A review. *J. Energy Storage* **2018**, *15*, 145-157.
12. Li, Z.; Khajepour, A.; Song, J., A comprehensive review of the key technologies for pure electric vehicles. *Energy* **2019**, *182*, 824-839.
13. Bocklisch, T., Hybrid energy storage approach for renewable energy applications. *J. Energy Storage* **2016**, *8*, 311-319.
14. Qi, N.; Yin, Y.; Dai, K.; Wu, C.; Wang, X.; You, Z., Comprehensive optimized hybrid energy storage system for long-life solar-powered wireless sensor network nodes. *Appl. Energy* **2021**, *290*, 116780.
15. Xu, H.; Shen, M., The control of lithium-ion batteries and supercapacitors in hybrid energy storage systems for electric vehicles: a review. *Int. J. Energy Res.* **2021**, *45* (15), 20524-20544.
16. Lashof, D. A.; Ahuja, D. R., Relative contributions of greenhouse gas emissions to global warming. *Nature* **1990**, *344* (6266), 529-531.
17. Chu, S.; Majumdar, A., Opportunities and challenges for a sustainable energy future. *nature* **2012**, *488* (7411), 294-303.
18. Nocera, D. G., Living healthy on a dying planet. *Chemical Society Reviews* **2009**, *38* (1), 13-15.
19. Hagfeldt, A.; Boschloo, G.; Sun, L.; Kloo, L.; Pettersson, H., Dye-sensitized solar cells. *Chem. Rev.* **2010**, *110* (11), 6595-6663.
20. Dillon, A., Carbon nanotubes for photoconversion and electrical energy storage. *Chem. Rev.* **2010**, *110* (11), 6856-6872.
21. Kondratenko, E. V.; Mul, G.; Baltrusaitis, J.; Larrazábal, G. O.; Pérez-Ramírez, J., Status and perspectives of CO₂ conversion into fuels and chemicals by catalytic, photocatalytic and electrocatalytic processes. *Energy Environ. Sci.* **2013**, *6* (11), 3112-3135.
22. Christopher, K.; Dimitrios, R., A review on exergy comparison of hydrogen production methods from renewable energy sources. *Energy Environ. Sci.* **2012**, *5* (5), 6640-6651.
23. Cook, T. R.; Dogutan, D. K.; Reece, S. Y.; Surendranath, Y.; Teets, T. S.; Nocera, D. G., Solar energy supply and storage for the legacy and nonlegacy worlds. *Chem. Rev.* **2010**, *110* (11), 6474-6502.

24. Yang, Z.; Zhang, J.; Kintner-Meyer, M. C.; Lu, X.; Choi, D.; Lemmon, J. P.; Liu, J., Electrochemical energy storage for green grid. *Chem. Rev.* **2011**, *111* (5), 3577-3613.
25. Miller, J. R.; Simon, P., Electrochemical capacitors for energy management. *science* **2008**, *321* (5889), 651-652.
26. Wang, H.; Dai, H., Strongly coupled inorganic–nano-carbon hybrid materials for energy storage. *Chem. Soc. Rev.* **2013**, *42* (7), 3088-3113.
27. Winter, M.; Brodd, R. J., What are batteries, fuel cells, and supercapacitors?(vol 104, pg 4245, 2003). *Chem. Rev.* **2005**, *105* (3), 1021-1021.
28. Zhang, L. L.; Zhao, X., Carbon-based materials as supercapacitor electrodes. *Chem. Soc. Rev.* **2009**, *38* (9), 2520-2531.
29. Rolison, D. R.; Long, J. W.; Lytle, J. C.; Fischer, A. E.; Rhodes, C. P.; McEvoy, T. M.; Bourg, M. E.; Lubers, A. M., Multifunctional 3D nanoarchitectures for energy storage and conversion. *Chem. Soc. Rev.* **2009**, *38* (1), 226-252.
30. Dunn, B.; Kamath, H.; Tarascon, J.-M., Electrical energy storage for the grid: a battery of choices. *Science* **2011**, *334* (6058), 928-935.
31. Zhang, Q.; Uchaker, E.; Candelaria, S. L.; Cao, G., Nanomaterials for energy conversion and storage. *Chem. Soc. Rev.* **2013**, *42* (7), 3127-3171.
32. Goodenough, J. B., Evolution of strategies for modern rechargeable batteries. *Acc. Chem. Res.* **2013**, *46* (5), 1053-1061.
33. Armand, M.; Tarascon, J.-M., Building better batteries. *nature* **2008**, *451* (7179), 652-657.
34. Shao, Y.; El-Kady, M. F.; Sun, J.; Li, Y.; Zhang, Q.; Zhu, M.; Wang, H.; Dunn, B.; Kaner, R. B., Design and mechanisms of asymmetric supercapacitors. *Chem. Rev.* **2018**, *118* (18), 9233-9280.
35. Arico, A. S.; Bruce, P.; Scrosati, B.; Tarascon, J.-M.; Van Schalkwijk, W., Nanostructured materials for advanced energy conversion and storage devices. *Mater. Sustain. Energy.* **2011**, 148-159.
36. Choi, N. S.; Chen, Z.; Freunberger, S. A.; Ji, X.; Sun, Y. K.; Amine, K.; Yushin, G.; Nazar, L. F.; Cho, J.; Bruce, P. G., Challenges facing lithium batteries and electrical double-layer capacitors. *Angew. Chem., Int. Ed.* **2012**, *51* (40), 9994-10024.
37. Wang, G.; Zhang, L.; Zhang, J., A review of electrode materials for electrochemical supercapacitors. *Chem. Soc. Rev.* **2012**, *41* (2), 797-828.

38. Zhai, Y.; Dou, Y.; Zhao, D.; Fulvio, P. F.; Mayes, R. T.; Dai, S., Carbon materials for chemical capacitive energy storage. *Adv. Mater.* **2011**, *23* (42), 4828-4850.
39. Kötz, R.; Carlen, M., Principles and applications of electrochemical capacitors. *Electrochim. Acta* **2000**, *45* (15-16), 2483-2498.
40. Béguin, F.; Presser, V.; Balducci, A.; Frackowiak, E., Carbons and electrolytes for advanced supercapacitors. *Adv. Mater.* **2014**, *26* (14), 2219-2251.
41. Conway, B. E., Transition from “supercapacitor” to “battery” behavior in electrochemical energy storage. *J. Electrochem. Soc.* **1991**, *138* (6), 1539.
42. Burke, A., Ultracapacitors: why, how, and where is the technology. *J. Power Sources* **2000**, *91* (1), 37-50.
43. Chu, A.; Braatz, P., Comparison of commercial supercapacitors and high-power lithium-ion batteries for power-assist applications in hybrid electric vehicles: I. Initial characterization. *J. Power Sources* **2002**, *112* (1), 236-246.
44. Augustyn, V.; Simon, P.; Dunn, B., Pseudocapacitive oxide materials for high-rate electrochemical energy storage. *Energy Environ. Sci.* **2014**, *7* (5), 1597-1614.
45. Forghani, M.; Donne, S. W., Method comparison for deconvoluting capacitive and pseudo-capacitive contributions to electrochemical capacitor electrode behavior. *J. Electrochem. Soc.* **2018**, *165* (3), A664.
46. Frackowiak, E.; Beguin, F., Carbon materials for the electrochemical storage of energy in capacitors. *Carbon* **2001**, *39* (6), 937-950.
47. Pandolfo, A. G.; Hollenkamp, A. F., Carbon properties and their role in supercapacitors. *J. Power Sources* **2006**, *157* (1), 11-27.
48. Frackowiak, E.; Beguin, F., Electrochemical storage of energy in carbon nanotubes and nanostructured carbons. *Carbon* **2002**, *40* (10), 1775-1787.
49. Su, D. S.; Schlögl, R., Nanostructured carbon and carbon nanocomposites for electrochemical energy storage applications. *ChemSusChem* **2010**, *3* (2), 136-168.
50. Simon, P.; Gogotsi, Y., Capacitive energy storage in nanostructured carbon–electrolyte systems. *Acc. Chem. Res.* **2013**, *46* (5), 1094-1103.
51. Raymundo-Piñero, E.; Leroux, F.; Béguin, F., A high-performance carbon for supercapacitors obtained by carbonization of a seaweed biopolymer. *Adv. Mater.* **2006**, *18* (14), 1877-1882.

52. Jost, K.; Perez, C. R.; McDonough, J. K.; Presser, V.; Heon, M.; Dion, G.; Gogotsi, Y., Carbon coated textiles for flexible energy storage. *Energy Environ. Sci.* **2011**, *4* (12), 5060-5067.
53. Gamby, J.; Taberna, P.; Simon, P.; Fauvarque, J.; Chesneau, M., Studies and characterisations of various activated carbons used for carbon/carbon supercapacitors. *J. Power Sources* **2001**, *101* (1), 109-116.
54. Zhi, M.; Xiang, C.; Li, J.; Li, M.; Wu, N., Nanostructured carbon–metal oxide composite electrodes for supercapacitors: a review. *Nanoscale* **2013**, *5* (1), 72-88.
55. Hu, S.; Rajamani, R.; Yu, X., Flexible solid-state paper based carbon nanotube supercapacitor. *Appl. Phys. Lett.* **2012**, *100* (10), 104103.
56. Kaempgen, M.; Chan, C. K.; Ma, J.; Cui, Y.; Gruner, G., Printable thin film supercapacitors using single-walled carbon nanotubes. *Nano Lett.* **2009**, *9* (5), 1872-1876.
57. Lota, G.; Fic, K.; Frackowiak, E., Carbon nanotubes and their composites in electrochemical applications. *Energy Environ. Sci.* **2011**, *4* (5), 1592-1605.
58. Yang, X.; Cheng, C.; Wang, Y.; Qiu, L.; Li, D., Liquid-mediated dense integration of graphene materials for compact capacitive energy storage. *science* **2013**, *341* (6145), 534-537.
59. An, K. H.; Kim, W. S.; Park, Y. S.; Moon, J. M.; Bae, D. J.; Lim, S. C.; Lee, Y. S.; Lee, Y. H., Electrochemical properties of high-power supercapacitors using single-walled carbon nanotube electrodes. *Adv. Funct. Mater.* **2001**, *11* (5), 387-392.
60. Niu, Z.; Zhou, W.; Chen, J.; Feng, G.; Li, H.; Ma, W.; Li, J.; Dong, H.; Ren, Y.; Zhao, D., Compact-designed supercapacitors using free-standing single-walled carbon nanotube films. *Energy Environ. Sci.* **2011**, *4* (4), 1440-1446.
61. Hu, L.; Pasta, M.; La Mantia, F.; Cui, L.; Jeong, S.; Deshazer, H. D.; Choi, J. W.; Han, S. M.; Cui, Y., Stretchable, porous, and conductive energy textiles. *Nano Lett.* **2010**, *10* (2), 708-714.
62. Yu, C.; Masarapu, C.; Rong, J.; Wei, B.; Jiang, H., Stretchable supercapacitors based on buckled single-walled carbon-nanotube macrofilms. *Adv. Mater.* **2009**, *21* (47), 4793-4797.
63. Raccichini, R.; Varzi, A.; Passerini, S.; Scrosati, B., The role of graphene for electrochemical energy storage. *Nat. Mater.* **2015**, *14* (3), 271-279.

64. Stoller, M. D.; Park, S.; Zhu, Y.; An, J.; Ruoff, R. S., Graphene-based ultracapacitors. *Nano Lett.* **2008**, *8* (10), 3498-3502.
65. Miller, J. R.; Outlaw, R.; Holloway, B., Graphene double-layer capacitor with ac line-filtering performance. *Science* **2010**, *329* (5999), 1637-1639.
66. El-Kady, M. F.; Strong, V.; Dubin, S.; Kaner, R. B., Laser scribing of high-performance and flexible graphene-based electrochemical capacitors. *Science* **2012**, *335* (6074), 1326-1330.
67. Brezesinski, T.; Wang, J.; Polleux, J.; Dunn, B.; Tolbert, S. H., Templated nanocrystal-based porous TiO₂ films for next-generation electrochemical capacitors. *J. Am. Chem. Soc.* **2009**, *131* (5), 1802-1809.
68. Zhu, J.; Yang, D.; Yin, Z.; Yan, Q.; Zhang, H., Graphene and graphene-based materials for energy storage applications. *Small* **2014**, *10* (17), 3480-3498.
69. Zhu, Y.; Murali, S.; Stoller, M. D.; Ganesh, K. J.; Cai, W.; Ferreira, P. J.; Pirkle, A.; Wallace, R. M.; Cychosz, K. A.; Thommes, M., Carbon-based supercapacitors produced by activation of graphene. *science* **2011**, *332* (6037), 1537-1541.
70. Yoo, J. J.; Balakrishnan, K.; Huang, J.; Meunier, V.; Sumpter, B. G.; Srivastava, A.; Conway, M.; Mohana Reddy, A. L.; Yu, J.; Vajtai, R., Ultrathin planar graphene supercapacitors. *Nano Lett.* **2011**, *11* (4), 1423-1427.
71. Stoller, M. D.; Magnuson, C. W.; Zhu, Y.; Murali, S.; Suk, J. W.; Piner, R.; Ruoff, R. S., Interfacial capacitance of single layer graphene. *Energy Environ. Sci.* **2011**, *4* (11), 4685-4689.
72. Liu, F.; Song, S.; Xue, D.; Zhang, H., Folded structured graphene paper for high performance electrode materials. *Adv. Mater.* **2012**, *24* (8), 1089-1094.
73. Shao, Y.; El-Kady, M. F.; Lin, C. W.; Zhu, G.; Marsh, K. L.; Hwang, J. Y.; Zhang, Q.; Li, Y.; Wang, H.; Kaner, R. B., 3D freeze-casting of cellular graphene films for ultrahigh-power-density supercapacitors. *Adv. Mater.* **2016**, *28* (31), 6719-6726.
74. El-Kady, M. F.; Kaner, R. B., Scalable fabrication of high-power graphene micro-supercapacitors for flexible and on-chip energy storage. *Nat. Commun.* **2013**, *4* (1), 1-9.
75. Li, J.; Shao, Y.; Shi, Q.; Hou, C.; Zhang, Q.; Li, Y.; Kaner, R. B.; Wang, H., Calligraphy-inspired brush written foldable supercapacitors. *Nano energy* **2017**, *38*, 428-437.

76. Su, X.; Ye, J.; Zhu, Y., Advances in in-situ characterizations of electrode materials for better supercapacitors. *J. Energy Chem.* **2021**, *54*, 242-253.
77. Bolt, G., Analysis of the validity of the Gouy-Chapman theory of the electric double layer. *J. Colloid Interface Sci.* **1955**, *10* (2), 206-218.
78. Wang, H.; Pilon, L., Accurate simulations of electric double layer capacitance of ultramicroelectrodes. *J. Phys. Chem. C* **2011**, *115* (33), 16711-16719.
79. Oldham, K. B., A Gouy–Chapman–Stern model of the double layer at a (metal)/(ionic liquid) interface. *J. Electroanal. Chem.* **2008**, *613* (2), 131-138.
80. Zhao, X.; Sánchez, B. M.; Dobson, P. J.; Grant, P. S., The role of nanomaterials in redox-based supercapacitors for next generation energy storage devices. *Nanoscale* **2011**, *3* (3), 839-855.
81. Rauda, I. E.; Augustyn, V.; Dunn, B.; Tolbert, S. H., Enhancing pseudocapacitive charge storage in polymer templated mesoporous materials. *Acc. Chem. Res.* **2013**, *46* (5), 1113-1124.
82. Brousse, T.; Bélanger, D.; Long, J. W., To be or not to be pseudocapacitive? *J. Electrochem. Soc.* **2015**, *162* (5), A5185.
83. Conway, B. E.; Birss, V.; Wojtowicz, J., The role and utilization of pseudocapacitance for energy storage by supercapacitors. *J. Power Sources* **1997**, *66* (1-2), 1-14.
84. Bi, R.-R.; Wu, X.-L.; Cao, F.-F.; Jiang, L.-Y.; Guo, Y.-G.; Wan, L.-J., Highly dispersed RuO₂ nanoparticles on carbon nanotubes: facile synthesis and enhanced supercapacitance performance. *J. Phys. Chem. C* **2010**, *114* (6), 2448-2451.
85. Yuan, C.; Zhang, X.; Su, L.; Gao, B.; Shen, L., Facile synthesis and self-assembly of hierarchical porous NiO nano/micro spherical superstructures for high performance supercapacitors. *J. Mater. Chem.* **2009**, *19* (32), 5772-5777.
86. Hu, C.-C.; Chang, K.-H.; Lin, M.-C.; Wu, Y.-T., Design and tailoring of the nanotubular arrayed architecture of hydrous RuO₂ for next generation supercapacitors. *Nano Lett.* **2006**, *6* (12), 2690-2695.
87. Makino, S.; Ban, T.; Sugimoto, W., Towards implantable bio-supercapacitors: pseudocapacitance of ruthenium oxide nanoparticles and nanosheets in acids, buffered solutions, and bioelectrolytes. *J. Electrochem. Soc.* **2015**, *162* (5), A5001.

88. Lee, H. Y.; Goodenough, J. B., Supercapacitor behavior with KCl electrolyte. *J. Solid State Chem.* **1999**, *144* (1), 220-223.
89. Lang, X.; Hirata, A.; Fujita, T.; Chen, M., Nanoporous metal/oxide hybrid electrodes for electrochemical supercapacitors. *Nat. Nanotechnol.* **2011**, *6* (4), 232-236.
90. Toupin, M.; Brousse, T.; Bélanger, D., Charge storage mechanism of MnO₂ electrode used in aqueous electrochemical capacitor. *Chem. Mater.* **2004**, *16* (16), 3184-3190.
91. Arbizzani, C.; Mastragostino, M.; Meneghello, L., Polymer-based redox supercapacitors: A comparative study. *Electrochim. Acta* **1996**, *41* (1), 21-26.
92. Mastragostino, M.; Arbizzani, C.; Soavi, F., Polymer-based supercapacitors. *J. Power Sources* **2001**, *97*, 812-815.
93. Ryu, K. S.; Kim, K. M.; Park, N.-G.; Park, Y. J.; Chang, S. H., Symmetric redox supercapacitor with conducting polyaniline electrodes. *J. Power Sources* **2002**, *103* (2), 305-309.
94. Kong, L.; Zhang, C.; Zhang, S.; Wang, J.; Cai, R.; Lv, C.; Qiao, W.; Ling, L.; Long, D., High-power and high-energy asymmetric supercapacitors based on Li⁺-intercalation into a T-Nb₂O₅/graphene pseudocapacitive electrode. *J. Mater. Chem.* **2014**, *2* (42), 17962-17970.
95. Kong, L.; Zhang, C.; Wang, J.; Qiao, W.; Ling, L.; Long, D., Free-standing T-Nb₂O₅/graphene composite papers with ultrahigh gravimetric/volumetric capacitance for Li-ion intercalation pseudocapacitor. *Acs Nano* **2015**, *9* (11), 11200-11208.
96. Kim, J. W.; Augustyn, V.; Dunn, B., The effect of crystallinity on the rapid pseudocapacitive response of Nb₂O₅. *Adv. Energy Mater.* **2012**, *2* (1), 141-148.
97. Augustyn, V.; Come, J.; Lowe, M. A.; Kim, J. W.; Taberna, P.-L.; Tolbert, S. H.; Abruña, H. D.; Simon, P.; Dunn, B., High-rate electrochemical energy storage through Li⁺ intercalation pseudocapacitance. *Nat. Mater.* **2013**, *12* (6), 518-522.
98. Come, J.; Augustyn, V.; Kim, J. W.; Rozier, P.; Taberna, P.-L.; Gogotsi, P.; Long, J. W.; Dunn, B.; Simon, P., Electrochemical kinetics of nanostructured Nb₂O₅ electrodes. *J. Electrochem. Soc.* **2014**, *161* (5), A718.

99. Sudha, V.; Sangaranarayanan, M., Underpotential deposition of metals: structural and thermodynamic considerations. *J. Phys. Chem. B* **2002**, *106* (10), 2699-2707.
100. El-Kady, M. F.; Shao, Y.; Kaner, R. B., Graphene for batteries, supercapacitors and beyond. *Nat. Rev. Mater.* **2016**, *1* (7), 1-14.
101. Wang, J.; Polleux, J.; Lim, J.; Dunn, B., Pseudocapacitive contributions to electrochemical energy storage in TiO₂ (anatase) nanoparticles. *J. Phys. Chem. C* **2007**, *111* (40), 14925-14931.
102. Lindström, H.; Södergren, S.; Solbrand, A.; Rensmo, H.; Hjelm, J.; Hagfeldt, A.; Lindquist, S.-E., Li⁺ ion insertion in TiO₂ (anatase). 2. Voltammetry on nanoporous films. *J. Phys. Chem. B* **1997**, *101* (39), 7717-7722.
103. Sathiya, M.; Prakash, A.; Ramesha, K.; Tarascon, J. M.; Shukla, A. K., V₂O₅-anchored carbon nanotubes for enhanced electrochemical energy storage. *J. Am. Chem. Soc.* **2011**, *133* (40), 16291-16299.
104. Brezesinski, T.; Wang, J.; Polleux, J.; Dunn, B.; Tolbert, S. H., Templated nanocrystal-based porous TiO₂ films for next-generation electrochemical capacitors. *J. Am. Chem. Soc.* **2009**, *131* (5), 1802-1809.
105. Wang, J.; Polleux, J.; Lim, J.; Dunn, B., Pseudocapacitive contributions to electrochemical energy storage in TiO₂ (anatase) nanoparticles. *J. Phys. Chem. C* **2007**, *111* (40), 14925-14931.
106. Abbas, Q.; Ratajczak, P.; Babuchowska, P.; Le Comte, A.; Bélanger, D.; Brousse, T.; Béguin, F., Strategies to improve the performance of carbon/carbon capacitors in salt aqueous electrolytes. *J. Electrochem. Soc.* **2015**, *162* (5), A5148.
107. Demarconnay, L.; Raymundo-Piñero, E.; Béguin, F., A symmetric carbon/carbon supercapacitor operating at 1.6 V by using a neutral aqueous solution. *Electrochem. Commun.* **2010**, *12* (10), 1275-1278.
108. Bichat, M.; Raymundo-Piñero, E.; Béguin, F., High voltage supercapacitor built with seaweed carbons in neutral aqueous electrolyte. *Carbon* **2010**, *48* (15), 4351-4361.
109. Gao, Q.; Demarconnay, L.; Raymundo-Piñero, E.; Béguin, F., Exploring the large voltage range of carbon/carbon supercapacitors in aqueous lithium sulfate electrolyte. *Energy Environ. Sci.* **2012**, *5* (11), 9611-9617.

110. Fic, K.; Lota, G.; Meller, M.; Frackowiak, E., Novel insight into neutral medium as electrolyte for high-voltage supercapacitors. *Energy Environ. Sci.* **2012**, *5* (2), 5842-5850.
111. Lin, T.; Chen, I.-W.; Liu, F.; Yang, C.; Bi, H.; Xu, F.; Huang, F., Nitrogen-doped mesoporous carbon of extraordinary capacitance for electrochemical energy storage. *Science* **2015**, *350* (6267), 1508-1513.
112. Pohlmann, S.; Ramirez-Castro, C.; Balducci, A., The influence of conductive salt ion selection on EDLC electrolyte characteristics and carbon-electrolyte interaction. *J. Electrochem. Soc.* **2015**, *162* (5), A5020.
113. Khomenko, V.; Raymundo-Piñero, E.; Béguin, F., High-energy density graphite/AC capacitor in organic electrolyte. *J. Power Sources* **2008**, *177* (2), 643-651.
114. Péan, C.; Daffos, B.; Merlet, C.; Rotenberg, B.; Taberna, P.-L.; Simon, P.; Salanne, M., Single electrode capacitances of porous carbons in neat ionic liquid electrolyte at 100 C: a combined experimental and modeling approach. *J. Electrochem. Soc.* **2015**, *162* (5), A5091.
115. Sillars, F. B.; Fletcher, S. I.; Mirzaeian, M.; Hall, P. J., Variation of electrochemical capacitor performance with room temperature ionic liquid electrolyte viscosity and ion size. *Phys. Chem. Chem.* **2012**, *14* (17), 6094-6100.
116. Zhong, C.; Deng, Y.; Hu, W.; Qiao, J.; Zhang, L.; Zhang, J., A review of electrolyte materials and compositions for electrochemical supercapacitors. *Chem. Soc. Rev.* **2015**, *44* (21), 7484-7539.
117. Winter, M.; Brodd, R., What Are Batteries, Fuel Cells, and Supercapacitors? *Chem. Rev.* **2005**, *105*, 1021-1021.
118. Yu, G.; Hu, L.; Liu, N.; Wang, H.; Vosgueritchian, M.; Yang, Y.; Cui, Y.; Bao, Z., Enhancing the supercapacitor performance of graphene/MnO₂ nanostructured electrodes by conductive wrapping. *Nano Lett.* **2011**, *11* (10), 4438-4442.
119. Lu, Q.; Chen, J. G.; Xiao, J. Q., Nanostructured electrodes for high-performance pseudocapacitors. *Angew. Chem., Int. Ed.* **2013**, *52* (7), 1882-1889.
120. Yu, Z.; Tetard, L.; Zhai, L.; Thomas, J., Supercapacitor electrode materials: nanostructures from 0 to 3 dimensions. *Energy Environ. Sci.* **2015**, *8* (3), 702-730.

121. Lu, X.; Wang, C.; Favier, F.; Pinna, N., Electrospun nanomaterials for supercapacitor electrodes: designed architectures and electrochemical performance. *Adv. Energy Mater.* **2017**, 7 (2), 1601301.
122. Xu, Y.; Wang, X.; An, C.; Wang, Y.; Jiao, L.; Yuan, H., Facile synthesis route of porous MnCo_2O_4 and CoMn_2O_4 nanowires and their excellent electrochemical properties in supercapacitors. *J. Mater. Chem.* **2014**, 2 (39), 16480-16488.
123. Gao, H.; Li, Y.; Zhao, H.; Xiang, J.; Cao, Y., A general fabrication approach on spinel MCo_2O_4 (M= Co, Mn, Fe, Mg and Zn) submicron prisms as advanced positive materials for supercapacitor. *Electrochim. Acta* **2018**, 262, 241-251.
124. Raj, S.; Kar, P.; Roy, P., Facile synthesis of flower-like morphology $\text{Cu}_{0.27}\text{Co}_{2.73}\text{O}_4$ for a high-performance supercapattery with extraordinary cycling stability. *Chem comm* **2018**, 54 (87), 12400-12403.
125. An, C.; Wang, Y.; Huang, Y.; Xu, Y.; Jiao, L.; Yuan, H., Porous NiCo_2O_4 nanostructures for high performance supercapacitors via a microemulsion technique. *Nano Energy* **2014**, 10, 125-134.
126. Kim, I.-H.; Kim, K.-B., Electrochemical characterization of hydrous ruthenium oxide thin-film electrodes for electrochemical capacitor applications. *J. Electrochem. Soc.* **2006**, 153 (2), A383.
127. Jia, Q.; Song, S.; Wu, X.; Cho, J.; Foltyn, S.; Findikoglu, A.; Smith, J., Epitaxial growth of highly conductive RuO_2 thin films on (100) Si. *Appl. Phys. Lett.* **1996**, 68 (8), 1069-1071.
128. Zheng, J.; Cygan, P.; Jow, T., Hydrous ruthenium oxide as an electrode material for electrochemical capacitors. *J. Electrochem. Soc.* **1995**, 142 (8), 2699.
129. Wu, N.-L.; Kuo, S.-L.; Lee, M.-H., Preparation and optimization of RuO_2 -impregnated SnO_2 xerogel supercapacitor. *J. Power Sources* **2002**, 104 (1), 62-65.
130. Ramani, M.; Haran, B. S.; White, R. E.; Popov, B. N., Synthesis and characterization of hydrous ruthenium oxide-carbon supercapacitors. *J. Electrochem. Soc.* **2001**, 148 (4), A374.
131. Ferro, S.; De Battisti, A., Electrocatalysis and chlorine evolution reaction at ruthenium dioxide deposited on conductive diamond. *J. Phys. Chem. B* **2002**, 106 (9), 2249-2254.

132. Su, Y.-f.; Feng, W.; Bao, L.-y.; Yang, Z.-h., RuO₂/activated carbon composites as a positive electrode in an alkaline electrochemical capacitor. *New Carbon Mater.* **2007**, *22* (1), 53-57.
133. Seo, M.-K.; Saouab, A.; Park, S.-J., Effect of annealing temperature on electrochemical characteristics of ruthenium oxide/multi-walled carbon nanotube composites. *Mater. Sci. Eng. B* **2010**, *167* (1), 65-69.
134. Zheng, Y.-Z.; Ding, H.-Y.; Zhang, M.-L., Hydrous–ruthenium–oxide thin film electrodes prepared by cathodic electrodeposition for supercapacitors. *Thin Solid Films* **2008**, *516* (21), 7381-7385.
135. Kim, Y.-T.; Tadai, K.; Mitani, T., Highly dispersed ruthenium oxide nanoparticles on carboxylated carbon nanotubes for supercapacitor electrode materials. *J. Mater. Chem.* **2005**, *15* (46), 4914-4921.
136. Yu, G.-Y.; Chen, W.-X.; Zheng, Y.-F.; Zhao, J.; Li, X.; Xu, Z.-D., Synthesis of Ru/carbon nanocomposites by polyol process for electrochemical supercapacitor electrodes. *Mater. Lett.* **2006**, *60* (20), 2453-2456.
137. Sugimoto, W.; Yokoshima, K.; Murakami, Y.; Takasu, Y., Charge storage mechanism of nanostructured anhydrous and hydrous ruthenium-based oxides. *Electrochim. Acta* **2006**, *52* (4), 1742-1748.
138. Wen, J.; Ruan, X.; Zhou, Z., Preparation and electrochemical performance of novel ruthenium–manganese oxide electrode materials for electrochemical capacitors. *J. Phys. Chem. Solids* **2009**, *70* (5), 816-820.
139. Foelske, A.; Barbieri, O.; Hahn, M.; Kötz, R., An X-ray photoelectron spectroscopy study of hydrous ruthenium oxide powders with various water contents for supercapacitors. *Electrochem. Solid-State Lett.* **2006**, *9* (6), A268.
140. Kim, H.; Popov, B. N., Characterization of hydrous ruthenium oxide/carbon nanocomposite supercapacitors prepared by a colloidal method. *J. Power Sources* **2002**, *104* (1), 52-61.
141. Subramanian, V.; Hall, S. C.; Smith, P. H.; Rambabu, B., Mesoporous anhydrous RuO₂ as a supercapacitor electrode material. *Solid State Ion.* **2004**, *175* (1-4), 511-515.
142. Takasu, Y.; Nakamura, T.; Ohkawauchi, H.; Murakami, Y., Dip-Coated Ru-V Oxide Electrodes for Electrochemical Capacitors. *J. Electrochem. Soc.* **1997**, *144* (8), 2601.

143. Yuan, C.-Z.; Gao, B.; Zhang, X.-G., Electrochemical capacitance of NiO/RuO₂. 35V0. 65O₂ asymmetric electrochemical capacitor. *J. Power sources* **2007**, *173* (1), 606-612.
144. Hwang, J. Y.; El-Kady, M. F.; Wang, Y.; Wang, L.; Shao, Y.; Marsh, K.; Ko, J. M.; Kaner, R. B., Direct preparation and processing of graphene/RuO₂ nanocomposite electrodes for high-performance capacitive energy storage. *Nano Energy* **2015**, *18*, 57-70.
145. Dupont, M. F.; Donne, S. W., Separating the faradaic and non-faradaic contributions to the total capacitance for different manganese dioxide phases. *J. Electrochem. Soc.* **2015**, *162* (5), A5096.
146. Ou, T.-M.; Hsu, C.-T.; Hu, C.-C., Synthesis and characterization of sodium-doped MnO₂ for the aqueous asymmetric supercapacitor application. *J. Electrochem. Soc.* **2015**, *162* (5), A5124.
147. Wei, W.; Cui, X.; Chen, W.; Ivey, D. G., Manganese oxide-based materials as electrochemical supercapacitor electrodes. *Chem. Soc. Rev.* **2011**, *40* (3), 1697-1721.
148. Toupin, M.; Brousse, T.; Bélanger, D., Influence of microstructure on the charge storage properties of chemically synthesized manganese dioxide. *Chem. Mater.* **2002**, *14* (9), 3946-3952.
149. Yang, X.-h.; Wang, Y.-g.; Xiong, H.-m.; Xia, Y.-y., Interfacial synthesis of porous MnO₂ and its application in electrochemical capacitor. *Electrochim. Acta* **2007**, *53* (2), 752-757.
150. Ragupathy, P.; Park, D. H.; Campet, G.; Vasan, H.; Hwang, S.-J.; Choy, J.-H.; Munichandraiah, N., Remarkable capacity retention of nanostructured manganese oxide upon cycling as an electrode material for supercapacitor. *J. Phys. Chem. C* **2009**, *113* (15), 6303-6309.
151. Pang, S.-C.; Anderson, M. A., Novel electrode materials for electrochemical capacitors: Part II. Material characterization of sol-gel-derived and electrodeposited manganese dioxide thin films. *J. Mater. Sci. Res.* **2000**, *15* (10), 2096-2106.
152. Broughton, J.; Brett, M., Electrochemical capacitance in manganese thin films with chevron microstructure. *Electrochem. Solid-State Lett.* **2002**, *5* (12), A279.

153. Wu, M.-S., Electrochemical capacitance from manganese oxide nanowire structure synthesized by cyclic voltammetric electrodeposition. *Appl. Phys. Lett.* **2005**, *87* (15), 153102.
154. Brousse, T.; Toupin, M.; Dugas, R.; Athouel, L.; Crosnier, O.; Belanger, D., Crystalline MnO₂ as possible alternatives to amorphous compounds in electrochemical supercapacitors. *J. Electrochem. Soc.* **2006**, *153* (12), A2171.
155. Ghodbane, O.; Pascal, J.-L.; Favier, F., Microstructural effects on charge-storage properties in MnO₂-based electrochemical supercapacitors. *ACS Appl. Mater. Interfaces.* **2009**, *1* (5), 1130-1139.
156. Li, Y.; Xie, H., Mechanochemical-synthesized Al-doped manganese dioxides for electrochemical supercapacitors. *Ionics* **2010**, *16* (1), 21-25.
157. Fischer, A. E.; Pettigrew, K. A.; Rolison, D. R.; Stroud, R. M.; Long, J. W., Incorporation of homogeneous, nanoscale MnO₂ within ultraporous carbon structures via self-limiting electroless deposition: implications for electrochemical capacitors. *Nano Lett.* **2007**, *7* (2), 281-286.
158. Wang, G.-X.; Zhang, B.-L.; Yu, Z.-L.; Qu, M.-Z., Manganese oxide/MWNTs composite electrodes for supercapacitors. *Solid State Ion.* **2005**, *176* (11-12), 1169-1174.
159. Fan, Z.; Chen, J.; Wang, M.; Cui, K.; Zhou, H.; Kuang, Y., Preparation and characterization of manganese oxide/CNT composites as supercapacitive materials. *Diam. Relat. Mater.* **2006**, *15* (9), 1478-1483.
160. Subramanian, V.; Zhu, H.; Wei, B., Synthesis and electrochemical characterizations of amorphous manganese oxide and single walled carbon nanotube composites as supercapacitor electrode materials. *Electrochem. commun.* **2006**, *8* (5), 827-832.
161. Lee, C. Y.; Tsai, H. M.; Chuang, H. J.; Li, S. Y.; Lin, P.; Tseng, T. Y., Characteristics and electrochemical performance of supercapacitors with manganese oxide-carbon nanotube nanocomposite electrodes. *J. Electrochem. Soc.* **2005**, *152* (4), A716.
162. Long, J. W.; Rhodes, C. P.; Young, A. L.; Rolison, D. R., Ultrathin, protective coatings of poly (o-phenylenediamine) as electrochemical proton gates: making mesoporous MnO₂ nanoarchitectures stable in acid electrolytes. *Nano Lett.* **2003**, *3* (8), 1155-1161.

163. McEvoy, T. M.; Long, J. W.; Smith, T. J.; Stevenson, K. J., Nanoscale conductivity mapping of hybrid nanoarchitectures: Ultrathin poly (o-phenylenediamine) on mesoporous manganese oxide ambigels. *Langmuir* **2006**, 22 (10), 4462-4466.
164. Liu, R.; Lee, S. B., MnO₂/poly (3, 4-ethylenedioxythiophene) coaxial nanowires by one-step coelectrodeposition for electrochemical energy storage. *J. Am. Chem. Soc.* **2008**, 130 (10), 2942-2943.
165. Wan, C.; Azumi, K.; Konno, H., Hydrated Mn (IV) oxide-exfoliated graphite composites for electrochemical capacitor. *Electrochim. Acta* **2007**, 52 (9), 3061-3066.
166. Yan, J.; Fan, Z.; Wei, T.; Qie, Z.; Wang, S.; Zhang, M., Preparation and electrochemical characteristics of manganese dioxide/graphite nanoplatelet composites. *Mater. Sci. Eng. B* **2008**, 151 (2), 174-178.
167. Wan, C.; Azumi, K.; Konno, H., Effect of synthesis routes on the performance of hydrated Mn (IV) oxide-exfoliated graphite composites for electrochemical capacitors. *J. Appl. Electrochem.* **2007**, 37 (9), 1055-1061.
168. Gao, H.; Xiao, F.; Ching, C. B.; Duan, H., High-performance asymmetric supercapacitor based on graphene hydrogel and nanostructured MnO₂. *ACS Appl. Mater. Interfaces.* **2012**, 4 (5), 2801-2810.
169. Huang, J.; Wang, K.; Wei, Z., Conducting polymer nanowire arrays with enhanced electrochemical performance. *J. Mater. Chem.* **2010**, 20 (6), 1117-1121.
170. Zhang, Y.; Feng, H.; Wu, X.; Wang, L.; Zhang, A.; Xia, T.; Dong, H.; Li, X.; Zhang, L., Progress of electrochemical capacitor electrode materials: A review. *Int. J. Hydrog. Energy* **2009**, 34 (11), 4889-4899.
171. Zhang, Y.; Xia, X.; Tu, J.; Mai, Y.; Shi, S.; Wang, X.; Gu, C., Self-assembled synthesis of hierarchically porous NiO film and its application for electrochemical capacitors. *J. Power Sources* **2012**, 199, 413-417.
172. Xia, X.; Tu, J.; Mai, Y.; Chen, R.; Wang, X.; Gu, C.; Zhao, X., Graphene sheet/porous NiO hybrid film for supercapacitor applications. *Eur. J. Chem.* **2011**, 17 (39), 10898-10905.
173. Zhao, G.; Jiang, L.; He, Y.; Li, J.; Dong, H.; Wang, X.; Hu, W., Sulfonated graphene for persistent aromatic pollutant management. *Adv. Mater.* **2011**, 23 (34), 3959-3963.

174. Srinivasan, V.; Weidner, J. W., An electrochemical route for making porous nickel oxide electrochemical capacitors. *J. Electrochem. Soc.* **1997**, *144* (8), L210.
175. Srinivasan, V.; Weidner, J. W., Studies on the capacitance of nickel oxide films: effect of heating temperature and electrolyte concentration. *J. Electrochem. Soc.* **2000**, *147* (3), 880.
176. Meher, S. K.; Justin, P.; Ranga Rao, G., Microwave-mediated synthesis for improved morphology and pseudocapacitance performance of nickel oxide. *ACS Appl. Mater. Interfaces.* **2011**, *3* (6), 2063-2073.
177. Tian, Z.-R.; Tong, W.; Wang, J.-Y.; Duan, N.-G.; Krishnan, V. V.; Suib, S. L., Manganese oxide mesoporous structures: mixed-valent semiconducting catalysts. *Science* **1997**, *276* (5314), 926-930.
178. Dai, M.; Song, L.; LaBelle, J. T.; Vogt, B. D., Ordered mesoporous carbon composite films containing cobalt oxide and vanadia for electrochemical applications. *Chem. Mater.* **2011**, *23* (11), 2869-2878.
179. Zhu, J.; Cao, L.; Wu, Y.; Gong, Y.; Liu, Z.; Hoster, H. E.; Zhang, Y.; Zhang, S.; Yang, S.; Yan, Q., Building 3D structures of vanadium pentoxide nanosheets and application as electrodes in supercapacitors. *Nano Lett.* **2013**, *13* (11), 5408-5413.
180. Saravanakumar, B.; Purushothaman, K. K.; Muralidharan, G., Interconnected V₂O₅ nanoporous network for high-performance supercapacitors. *ACS Appl. Mater. Interfaces.* **2012**, *4* (9), 4484-4490.
181. Perera, S. D.; Patel, B.; Nijem, N.; Roodenko, K.; Seitz, O.; Ferraris, J. P.; Chabal, Y. J.; Balkus Jr, K. J., Vanadium oxide nanowire-carbon nanotube binder-free flexible electrodes for supercapacitors. *Adv. Energy Mater.* **2011**, *1* (5), 936-945.
182. Qu, Q.; Zhu, Y.; Gao, X.; Wu, Y., Core-shell structure of polypyrrole grown on V₂O₅ nanoribbon as high performance anode material for supercapacitors. *Adv. Energy Mater.* **2012**, *2* (8), 950-955.
183. Ghosh, A.; Ra, E. J.; Jin, M.; Jeong, H. K.; Kim, T. H.; Biswas, C.; Lee, Y. H., High pseudocapacitance from ultrathin V₂O₅ films electrodeposited on self-standing carbon-nanofiber paper. *Adv. Funct. Mater.* **2011**, *21* (13), 2541-2547.

184. Kong, X.; Liu, X.; He, Y.; Zhang, D.; Wang, X.; Li, Y., Hydrothermal synthesis of β -nickel hydroxide microspheres with flakelike nanostructures and their electrochemical properties. *Mater. Chem. Phys.* **2007**, *106* (2-3), 375-378.
185. Bastakoti, B. P.; Huang, H.-S.; Chen, L.-C.; Wu, K. C.-W.; Yamauchi, Y., Block copolymer assisted synthesis of porous α -Ni(OH)₂ microflowers with high surface areas as electrochemical pseudocapacitor materials. *Chem. Commun.* **2012**, *48* (73), 9150-9152.
186. Wang, H.; Liang, Y.; Mirfakhrai, T.; Chen, Z.; Casalongue, H. S.; Dai, H., Advanced asymmetrical supercapacitors based on graphene hybrid materials. *Nano Res.* **2011**, *4* (8), 729-736.
187. Li, B.; Ai, M.; Xu, Z., Mesoporous β -Ni(OH)₂: synthesis and enhanced electrochemical performance. *Chem. Commun.* **2010**, *46* (34), 6267-6269.
188. Guo, S.; Dong, S., Graphene nanosheet: synthesis, molecular engineering, thin film, hybrids, and energy and analytical applications. *Chem. Soc. Rev.* **2011**, *40* (5), 2644-2672.
189. Wang, S.; Pei, B.; Zhao, X.; Dryfe, R. A., Highly porous graphene on carbon cloth as advanced electrodes for flexible all-solid-state supercapacitors. *Nano Energy* **2013**, *2* (4), 530-536.
190. Yang, S.; Wu, X.; Chen, C.; Dong, H.; Hu, W.; Wang, X., Spherical α -Ni(OH)₂ nanoarchitecture grown on graphene as advanced electrochemical pseudocapacitor materials. *Chem. Commun.* **2012**, *48* (22), 2773-2775.
191. Zhang, J.; Liu, S.; Pan, G.; Li, G.; Gao, X., A 3D hierarchical porous α -Ni(OH)₂/graphite nanosheet composite as an electrode material for supercapacitors. *J. Mater. Chem.* **2014**, *2* (5), 1524-1529.
192. Novoselov, K. S.; Geim, A. K.; Morozov, S. V.; Jiang, D.-e.; Zhang, Y.; Dubonos, S. V.; Grigorieva, I. V.; Firsov, A. A., Electric field effect in atomically thin carbon films. *science* **2004**, *306* (5696), 666-669.
193. Cai, J.; Ruffieux, P.; Jaafar, R.; Bieri, M.; Braun, T.; Blankenburg, S.; Muoth, M.; Seitsonen, A. P.; Saleh, M.; Feng, X., Atomically precise bottom-up fabrication of graphene nanoribbons. *Nature* **2010**, *466* (7305), 470-473.
194. Tung, V. C.; Allen, M. J.; Yang, Y.; Kaner, R. B., High-throughput solution processing of large-scale graphene. *Nat. Nanotechnol* **2009**, *4* (1), 25-29.

195. Choucair, M.; Thordarson, P.; Stride, J. A., Gram-scale production of graphene based on solvothermal synthesis and sonication. *Nat. Nanotechnol* **2009**, *4* (1), 30-33.
196. Emtsev, K. V.; Bostwick, A.; Horn, K.; Jobst, J.; Kellogg, G. L.; Ley, L.; McChesney, J. L.; Ohta, T.; Reshanov, S. A.; Röhrl, J., Towards wafer-size graphene layers by atmospheric pressure graphitization of silicon carbide. *Nat. Mater.* **2009**, *8* (3), 203-207.
197. Kim, K. S.; Zhao, Y.; Jang, H.; Lee, S. Y.; Kim, J. M.; Kim, K. S.; Ahn, J.-H.; Kim, P.; Choi, J.-Y.; Hong, B. H., Large-scale pattern growth of graphene films for stretchable transparent electrodes. *nature* **2009**, *457* (7230), 706-710.
198. Yang, X.; Dou, X.; Rouhanipour, A.; Zhi, L.; Räder, H. J.; Müllen, K., Two-dimensional graphene nanoribbons. *J. Am. Chem. Soc.* **2008**, *130* (13), 4216-4217.
199. Taghioskoui, M., Trends in graphene research. *Mater. Today* **2009**, *12* (10), 34-37.
200. Chen, J.; Duan, M.; Chen, G., Continuous mechanical exfoliation of graphene sheets via three-roll mill. *J. Mater. Chem.* **2012**, *22* (37), 19625-19628.
201. Li, D.; Müller, M. B.; Gilje, S.; Kaner, R. B.; Wallace, G. G., Processable aqueous dispersions of graphene nanosheets. *Nat. Nanotechnol* **2008**, *3* (2), 101-105.
202. Park, S.; Ruoff, R. S., Chemical methods for the production of graphenes. *Nat. Nanotechnol* **2009**, *4* (4), 217-224.
203. Shen, J.; Hu, Y.; Shi, M.; Lu, X.; Qin, C.; Li, C.; Ye, M., Fast and facile preparation of graphene oxide and reduced graphene oxide nanoplatelets. *Chem. Mater.* **2009**, *21* (15), 3514-3520.
204. Lei, Z.; Lu, L.; Zhao, X., The electrocapacitive properties of graphene oxide reduced by urea. *Energy Environ. Sci.* **2012**, *5* (4), 6391-6399.
205. Huang, H.-C.; Huang, C.-W.; Hsieh, C.-T.; Kuo, P.-L.; Ting, J.-M.; Teng, H., Photocatalytically reduced graphite oxide electrode for electrochemical capacitors. *J. Phys. Chem. C* **2011**, *115* (42), 20689-20695.
206. Xia, J.; Chen, F.; Li, J.; Tao, N., Measurement of the quantum capacitance of graphene. *Nat. Nanotechnol* **2009**, *4* (8), 505-509.
207. Lv, W.; Tang, D.-M.; He, Y.-B.; You, C.-H.; Shi, Z.-Q.; Chen, X.-C.; Chen, C.-M.; Hou, P.-X.; Liu, C.; Yang, Q.-H., Low-temperature exfoliated graphenes:

- vacuum-promoted exfoliation and electrochemical energy storage. *ACS nano* **2009**, *3* (11), 3730-3736.
208. Zhu, Y.; Stoller, M. D.; Cai, W.; Velamakanni, A.; Piner, R. D.; Chen, D.; Ruoff, R. S., Exfoliation of graphite oxide in propylene carbonate and thermal reduction of the resulting graphene oxide platelets. *ACS nano* **2010**, *4* (2), 1227-1233.
209. Vivekchand, S.; Rout, C. S.; Subrahmanyam, K.; Govindaraj, A.; Rao, C. N. R., Graphene-based electrochemical supercapacitors. *J. Chem. Sci.* **2008**, *120* (1), 9-13.
210. Yang, X.; Zhu, J.; Qiu, L.; Li, D., Bioinspired effective prevention of restacking in multilayered graphene films: towards the next generation of high-performance supercapacitors. *Adv. Mater.* **2011**, *23* (25), 2833-2838.
211. Liu, C.; Yu, Z.; Neff, D.; Zhamu, A.; Jang, B. Z., Graphene-based supercapacitor with an ultrahigh energy density. *Nano Lett.* **2010**, *10* (12), 4863-4868.
212. Jeong, H. M.; Lee, J. W.; Shin, W. H.; Choi, Y. J.; Shin, H. J.; Kang, J. K.; Choi, J. W., Nitrogen-doped graphene for high-performance ultracapacitors and the importance of nitrogen-doped sites at basal planes. *Nano Lett.* **2011**, *11* (6), 2472-2477.
213. Meng, C.; Liu, C.; Chen, L.; Hu, C.; Fan, S., Highly flexible and all-solid-state paperlike polymer supercapacitors. *Nano Lett.* **2010**, *10* (10), 4025-4031.
214. Xue, M.; Li, F.; Zhu, J.; Song, H.; Zhang, M.; Cao, T., Structure-based enhanced capacitance: in situ growth of highly ordered polyaniline nanorods on reduced graphene oxide patterns. *Adv. Funct. Mater.* **2012**, *22* (6), 1284-1290.
215. Cao, X.; Shi, Y.; Shi, W.; Lu, G.; Huang, X.; Yan, Q.; Zhang, Q.; Zhang, H., Preparation of novel 3D graphene networks for supercapacitor applications. *small* **2011**, *7* (22), 3163-3168.
216. Lv, W.; Sun, F.; Tang, D.-M.; Fang, H.-T.; Liu, C.; Yang, Q.-H.; Cheng, H.-M., A sandwich structure of graphene and nickel oxide with excellent supercapacitive performance. *J. Mater. Chem.* **2011**, *21* (25), 9014-9019.
217. Guo, B.; Gao, Y.; Li, Y.; Liu, K.; Lv, X.; Mi, C.; Liu, L.; Li, M., Battery-Type-Behavior-Retention Ni(OH)₂-rGO Composite for an Ultrahigh-Specific-Capacity Asymmetric Electrochemical Capacitor Electrode. *ACS omega* **2023**, *8* (7), 6289-6301.

218. Pundir, S.; Upadhyay, S.; Priya, R.; Kumar, N.; Chetana, S.; Hossain, I.; Joshi, N. C.; Pandey, O., Synthesis of 1D β -MnO₂ for high-performance supercapacitor application. *J Solid State Electrochem* **2023**, 27 (2), 531-538.
219. Bae, S. Y.; Seo, H. W.; Park, J., Vertically aligned sulfur-doped ZnO nanowires synthesized via chemical vapor deposition. *J. Phys. Chem. B* **2004**, 108 (17), 5206-5210.
220. Chen, Y.; Li, J.; Han, Y.; Yang, X.; Dai, J., The effect of Mg vapor source on the formation of MgO whiskers and sheets. *J. Cryst. Growth*. **2002**, 245 (1-2), 163-170.
221. Wu, J.-M.; Shih, H. C.; Wu, W.-T.; Tseng, Y.-K.; Chen, I.-C., Thermal evaporation growth and the luminescence property of TiO₂ nanowires. *J. Cryst. Growth*. **2005**, 281 (2-4), 384-390.
222. Yadav, A.; Fu, B.; Bonvicini, S. N.; Ly, L. Q.; Jia, Z.; Shi, Y., β -Ga₂O₃ Nanostructures: Chemical Vapor Deposition Growth Using Thermally Dewetted Au Nanoparticles as Catalyst and Characterization. *J. Nanomater.* **2022**, 12 (15), 2589.
223. Wen, X.; Wang, S.; Ding, Y.; Wang, Z. L.; Yang, S., Controlled growth of large-area, uniform, vertically aligned arrays of α -Fe₂O₃ nanobelts and nanowires. *J. Phys. Chem. B* **2005**, 109 (1), 215-220.
224. Zhou, J.; Gong, L.; Deng, S. Z.; Chen, J.; She, J. C.; Xu, N. S.; Yang, R.; Wang, Z. L., Growth and field-emission property of tungsten oxide nanotip arrays. *Appl. Phys. Lett.* **2005**, 87 (22), 223108.
225. Xia, Y.; Yang, P.; Sun, Y.; Wu, Y.; Mayers, B.; Gates, B.; Yin, Y.; Kim, F.; Yan, H., One-dimensional nanostructures: synthesis, characterization, and applications. *Adv. Mater.* **2003**, 15 (5), 353-389.
226. Umar, A.; Hahn, Y., Aligned hexagonal coaxial-shaped ZnO nanocolumns on steel alloy by thermal evaporation. *Appl. Phys. Lett.* **2006**, 88 (17), 173120.
227. Sekar, A.; Kim, S.; Umar, A.; Hahn, Y., Catalyst-free synthesis of ZnO nanowires on Si by oxidation of Zn powders. *J. Cryst. Growth*. **2005**, 277 (1-4), 471-478.
228. Umar, A.; Lee, S.; Lee, Y.; Nahm, K.; Hahn, Y., Star-shaped ZnO nanostructures on silicon by cyclic feeding chemical vapor deposition. *J. Cryst. Growth*. **2005**, 277 (1-4), 479-484.

229. Umar, A.; Kim, S.; Im, Y.; Hahn, Y., Structural and optical properties of ZnO micro-spheres and cages by oxidation of metallic Zn powder. *Superlattices Microstruct.* **2006**, *39* (1-4), 238-246.
230. Zhou, J.; Ding, Y.; Deng, S. Z.; Gong, L.; Xu, N. S.; Wang, Z. L., Three-dimensional tungsten oxide nanowire networks. *Adv. Mater.* **2005**, *17* (17), 2107-2110.
231. Hu, J.; Ma, X.; Shang, N.; Xie, Z.; Wong, N.; Lee, C.; Lee, S., Large-scale rapid oxidation synthesis of SnO₂ nanoribbons. *J. Phys. Chem. B* **2002**, *106* (15), 3823-3826.
232. Zhao, Q.; Xu, X., h. Zhang, Y. Chen, J. Xu and D. Yu. *Appl. Phys. A Mater. Sci. Process* **2004**, *79*, 1721.
233. Park, S.-H., Intraband relaxation time in wurtzite InGaN/GaN quantum-well structures with (10 $\bar{1}$ 0) crystal orientation. *Appl. Phys. Lett.* **2002**, *81* (6), 1149-1149.
234. Zhang, B.; Binh, N.; Segawa, Y.; Wakatsuki, K.; Usami, N., Optical properties of ZnO rods formed by metalorganic chemical vapor deposition. *Appl. Phys. Lett.* **2003**, *83* (8), 1635-1637.
235. Su, J.; Gherasimova, M.; Cui, G.; Tsukamoto, H.; Han, J.; Onuma, T.; Kurimoto, M.; Chichibu, S.; Broadbridge, C.; He, Y., Growth of AlGaIn nanowires by metalorganic chemical vapor deposition. *Appl. Phys. Lett.* **2005**, *87* (18), 183108.
236. Kang, T.-T.; Liu, X.; Zhang, R. Q.; Hu, W. G.; Cong, G.; Zhao, F.-A.; Zhu, Q., InN nanoflowers grown by metal organic chemical vapor deposition. *Appl. Phys. Lett.* **2006**, *89* (7), 071113.
237. Baxter, J. B.; Aydil, E. S., Nanowire-based dye-sensitized solar cells. *Appl. Phys. Lett.* **2005**, *86* (5), 053114.
238. Liu, B.; Zeng, H. C., Hydrothermal synthesis of ZnO nanorods in the diameter regime of 50 nm. *J. Am. Chem. Soc.* **2003**, *125* (15), 4430-4431.
239. Zhang, J.; Liu, Z.; Lin, C.; Lin, J., A simple method to synthesize β -Ga₂O₃ nanorods and their photoluminescence properties. *J. Cryst. Growth.* **2005**, *280* (1-2), 99-106.
240. Cao, M.; Wang, Y.; Guo, C.; Qi, Y.; Hu, C.; Wang, E., A simple route towards CuO nanowires and nanorods. *J. Nanosci. Nanotechnol.* **2004**, *4* (7), 824-828.

241. Zheng, D.; Sun, S.; Fan, W.; Yu, H.; Fan, C.; Cao, G.; Yin, Z.; Song, X., One-step preparation of single-crystalline β -MnO₂ nanotubes. *J. Phys. Chem. B* **2005**, *109* (34), 16439-16443.
242. Zhou, K.; Wang, X.; Sun, X.; Peng, Q.; Li, Y., Enhanced catalytic activity of ceria nanorods from well-defined reactive crystal planes. *J. Catal.* **2005**, *229* (1), 206-212.
243. Yuan, Z.-Y.; Su, B.-L., Titanium oxide nanotubes, nanofibers and nanowires. *Colloids Surf.* **2004**, *241* (1-3), 173-183.
244. Ozin, G. A., Panoscopic materials: synthesis over 'all'length scales. *ChemComm* **2000**, (6), 419-432.
245. Whitesides, G. M.; Grzybowski, B., Self-assembly at all scales. *Science* **2002**, *295* (5564), 2418-2421.
246. Lu, W.; Lieber, C. M., Nanoelectronics from the bottom up. *Nanosci. Technol.* **2010**, 137-146.
247. Burda, C.; Chen, X.; Narayanan, R.; El-Sayed, M. A., Chemistry and properties of nanocrystals of different shapes. *Chem. Rev.* **2005**, *105* (4), 1025-1102.
248. Ozin, G. A., Panoscopic materials: synthesis over 'all'length scales. *ChemComm.* **2000**, (6), 419-432.
249. Paily, R.; DasGupta, A.; DasGupta, N.; Bhattacharya, P.; Misra, P.; Ganguli, T.; Kukreja, L. M.; Balamurugan, A.; Rajagopalan, S.; Tyagi, A., Pulsed laser deposition of TiO₂ for MOS gate dielectric. *Appl. Surf. Sci.* **2002**, *187* (3-4), 297-304.
250. Wang, F.; Liu, X.; Chen, F.; Wan, H.; Lin, Y.; Zhang, N.; Ma, R., Advanced supercapacitors based on α -Ni(OH)₂ nanoplates/graphene composite electrodes with high energy and power density. *ACS Appl. Energy Mater.* **2018**, *1* (4), 1496-1505.
251. Wang, H.; Robinson, J. T.; Li, X.; Dai, H., Solvothermal reduction of chemically exfoliated graphene sheets. *J. Am. Chem. Soc.* **2009**, *131* (29), 9910-9911.
252. Xia, T.; Zhang, X.; Zhao, J.; Li, Q.; Ao, C.; Hu, R.; Zheng, Z.; Zhang, W.; Lu, C.; Deng, Y., Flexible and conductive carbonized cotton fabrics coupled with a nanostructured Ni(OH)₂ coating for high performance aqueous symmetric supercapacitors. *ACS Sustain. Chem. Eng.* **2019**, *7* (5), 5231-5239.

253. Zhang, H.; Zhang, X.; Zhang, D.; Sun, X.; Lin, H.; Wang, C.; Ma, Y., One-step electrophoretic deposition of reduced graphene oxide and Ni(OH)₂ composite films for controlled syntheses supercapacitor electrodes. *J. Phys. Chem. B* **2013**, *117* (6), 1616-1627.
254. Chao, D.; Zhu, C.; Yang, P.; Xia, X.; Liu, J.; Wang, J.; Fan, X.; Savilov, S. V.; Lin, J.; Fan, H. J., Array of nanosheets render ultrafast and high-capacity Na-ion storage by tunable pseudocapacitance. *Nat. Commun.* **2016**, *7* (1), 12122.
255. Chao, D.; Zhu, C.; Yang, P.; Xia, X.; Liu, J.; Wang, J.; Fan, X.; Savilov, S. V.; Lin, J.; Fan, H. J., Array of nanosheets render ultrafast and high-capacity Na-ion storage by tunable pseudocapacitance. *Nat. Commun.* **2016**, *7* (1), 1-8.
256. Zhang, L.; Gong, H., Unravelling the correlation between nickel to copper ratio of binary oxides and their superior supercapacitor performance. *Electrochim. Acta* **2017**, *234*, 82-92.
257. Atika; Dutta, R., Amino Acid Mediated Highly Ordered Carbon Dots as Phase Directing Agent for Synthesizing α -Ni (OH)₂ Decorated with Nitrogen Doped CD as an Electrode for an Efficient Symmetric Supercapacitor. *Energy & Fuels* **2023**.
258. Bello, A.; Barzegar, F.; Momodu, D.; Dangbegnon, J.; Taghizadeh, F.; Manyala, N., Symmetric supercapacitors based on porous 3D interconnected carbon framework. *Electrochimica Acta* **2015**, *151*, 386-392.
259. Wang, Q.; Yan, J.; Wang, Y.; Wei, T.; Zhang, M.; Jing, X.; Fan, Z., Three-dimensional flower-like and hierarchical porous carbon materials as high-rate performance electrodes for supercapacitors. *Carbon* **2014**, *67*, 119-127.
260. Salunkhe, R. R.; Kamachi, Y.; Torad, N. L.; Hwang, S. M.; Sun, Z.; Dou, S. X.; Kim, J. H.; Yamauchi, Y., Fabrication of symmetric supercapacitors based on MOF-derived nanoporous carbons. *J. Mater. Chem.* **2014**, *2* (46), 19848-19854.
261. Jing, M.; Yang, Y.; Zhu, Y.; Hou, H.; Wu, Z.; Ji, X., An asymmetric ultracapacitors utilizing α -Co(OH)₂/Co₃O₄ flakes assisted by electrochemically alternating voltage. *Electrochim. Acta* **2014**, *141*, 234-240.
262. Wang, X.; Liu, W. S.; Lu, X.; Lee, P. S., Dodecyl sulfate-induced fast faradic process in nickel cobalt oxide–reduced graphite oxide composite material and its application for asymmetric supercapacitor device. *J. Mater. Chem.* **2012**, *22* (43), 23114-23119.

263. Wang, Y.; Yang, D.; Lian, J.; Pan, J.; Wei, T.; Sun, Y., Cedar leaf-like CuCo_2O_4 directly grow on nickel foam by a hydrothermal/annealing process as an electrode for a high-performance symmetric supercapacitor. *J. Alloys Compd.* **2018**, *735*, 2046-2052.
264. Ji, J.; Zhang, L. L.; Ji, H.; Li, Y.; Zhao, X.; Bai, X.; Fan, X.; Zhang, F.; Ruoff, R. S., Nanoporous $\text{Ni}(\text{OH})_2$ thin film on 3D ultrathin-graphite foam for asymmetric supercapacitor. *ACS nano* **2013**, *7* (7), 6237-6243.
265. Wang, D.; Guan, B.; Li, Y.; Li, D.; Xu, Z.; Hu, Y.; Wang, Y.; Zhang, H., Morphology-controlled synthesis of hierarchical mesoporous $\alpha\text{-Ni}(\text{OH})_2$ microspheres for high-performance asymmetric supercapacitors. *J. Alloys Compd.* **2018**, *737*, 238-247.
266. Gao, X.; Zhang, H.; Guo, E.; Yao, F.; Wang, Z.; Yue, H., Hybrid two-dimensional nickel oxide-reduced graphene oxide nanosheets for supercapacitor electrodes. *Microchem. J.* **2021**, *164*, 105979.
267. Balachandran, U.; Eror, N., Raman spectra of titanium dioxide. *J. Solid State Chem.* **1982**, *42* (3), 276-282.
268. Ma, Y.; Zhang, J.; Tian, B.; Chen, F.; Wang, L., Synthesis and characterization of thermally stable Sm, N co-doped TiO_2 with highly visible light activity. *J. Hazard. Mater.* **2010**, *182* (1-3), 386-393.
269. Xin, B.; Ren, Z.; Wang, P.; Liu, J.; Jing, L.; Fu, H., Study on the mechanisms of photoinduced carriers separation and recombination for $\text{Fe}^{3+}\text{-TiO}_2$ photocatalysts. *Appl. Surf. Sci.* **2007**, *253* (9), 4390-4395.
270. Chiarello, G. L.; Aguirre, M. H.; Selli, E., Hydrogen production by photocatalytic steam reforming of methanol on noble metal-modified TiO_2 . *J. Catal.* **2010**, *273* (2), 182-190.
271. Sivaranjani, K.; Gopinath, C. S., Porosity driven photocatalytic activity of wormhole mesoporous $\text{TiO}_{2-x}\text{N}_x$ in direct sunlight. *J. Mater. Chem.* **2011**, *21* (8), 2639-2647.
272. Lim, S.; Huang, N.; Lim, H.; Mazhar, c., Aerosol assisted chemical vapour deposited (AACVD) of TiO_2 thin film as compact layer for dye-sensitised solar cell. *Ceram. Int.* **2014**, *40* (6), 8045-8052.
273. Su, C.; Liu, L.; Zhang, M.; Zhang, Y.; Shao, C., Fabrication of Ag/TiO_2 nanoheterostructures with visible light photocatalytic function via a solvothermal approach. *CrystEngComm* **2012**, *14* (11), 3989-3999.

274. Subramanian, V.; Wolf, E. E.; Kamat, P. V., Catalysis with TiO₂/gold nanocomposites. Effect of metal particle size on the Fermi level equilibration. *J. Am. Chem. Soc.* **2004**, *126* (15), 4943-4950.
275. Lim, S. P.; Pandikumar, A.; Huang, N. M.; Lim, H. N., Silver/titania nanocomposite-modified photoelectrodes for photoelectrocatalytic methanol oxidation. *Int. J. Hydrog.* **2014**, *39* (27), 14720-14729.
276. Al Kiey, S. A.; Abdelhamid, H. N., Metal-organic frameworks (MOFs)-derived Co₃O₄@ N-doped carbon as an electrode materials for supercapacitor. *J. Energy Storage* **2022**, *55*, 105449.
277. Ma, Y.; Bai, Y.; Liang, B.; Yang, R.; Jiang, X.; Zheng, S.; Zhang, C.; Hu, C., Doping-induced morphology modulation for boosting the capacity and stability of nanocrystals assembled Ni_{1-x}Co_xSe₂. *Appl. Surf. Sci.* **2022**, *579*, 152156.
278. Liu, Y.; Fu, N.; Zhang, G.; Xu, M.; Lu, W.; Zhou, L.; Huang, H., Design of Hierarchical Ni□ Co@ Ni□ Co Layered Double Hydroxide Core–Shell Structured Nanotube Array for High-Performance Flexible All-Solid-State Battery-Type Supercapacitors. *Advanced Functional Materials* **2017**, *27* (8), 1605307.
279. Yang, S.; Lin, Y.; Song, X.; Zhang, P.; Gao, L., Covalently coupled ultrafine H-TiO₂ nanocrystals/nitrogen-doped graphene hybrid materials for high-performance supercapacitor. *ACS applied materials & interfaces* **2015**, *7* (32), 17884-17892.
280. Pandit, B.; Pande, S. A.; Sankapal, B. R., Facile SILAR processed Bi₂S₃: PbS solid solution on MWCNTs for high-performance electrochemical supercapacitor. *Chin. J. Chem.* **2019**, *37* (12), 1279-1286.
281. Pazhamalai, P.; Krishnamoorthy, K.; Mariappan, V. K.; Kim, S.-J., Blue TiO₂ nanosheets as a high-performance electrode material for supercapacitors. *J. Colloid Interface Sci.* **2019**, *536*, 62-70.
282. Chen, J.; Xu, J.; Zhou, S.; Zhao, N.; Wong, C.-P., Amorphous nanostructured FeOOH and Co–Ni double hydroxides for high-performance aqueous asymmetric supercapacitors. *Nano Energy* **2016**, *21*, 145-153.
283. Chen, H.; Hu, L.; Yan, Y.; Che, R.; Chen, M.; Wu, L., One-step fabrication of ultrathin porous nickel hydroxide-manganese dioxide hybrid nanosheets for supercapacitor electrodes with excellent capacitive performance. *Adv. Energy Mater.* **2013**, *3* (12), 1636-1646.

284. Zhu, G.; He, Z.; Chen, J.; Zhao, J.; Feng, X.; Ma, Y.; Fan, Q.; Wang, L.; Huang, W., Highly conductive three-dimensional MnO₂-carbon nanotube-graphene-Ni hybrid foam as a binder-free supercapacitor electrode. *Nanoscale* **2014**, *6* (2), 1079-1085.
285. Shao, M.; Ning, F.; Zhao, J.; Wei, M.; Evans, D. G.; Duan, X., Hierarchical layered double hydroxide microspheres with largely enhanced performance for ethanol electrooxidation. *Adv. Funct. Mater.* **2013**, *23* (28), 3513-3518.
286. Khan, M. D.; Akhtar, J.; Malik, M. A.; Akhtar, M.; Revaprasadu, N., Phase-pure fabrication and shape evolution studies of SnS nanosheets. *New J Chem* **2015**, *39* (12), 9569-9574.
287. Deka, R.; Rajak, R.; Kumar, V.; Mobin, S. M., Effect of Electrolytic Cations on a 3D Cd-MOF for Supercapacitive Electrodes. *Inorg. Chem.* **2023**, *62* (7), 3084-3094.
288. Bashir, A.; Inayat, A.; Bashir, R.; Jamil, S.; Abbas, S. M.; Sultan, M.; Iqbal, A.; Akhter, Z., Design of porous Ni and rare earth metal (Ce, Ho, and Eu) Co-doped TiO₂ nanoarchitectures for energy conversion and storage applications. *New J Chem* **2023**, *47* (7), 3560-3571.
289. Wang, D.; Ni, W.; Pang, H.; Lu, Q.; Huang, Z.; Zhao, J., Preparation of mesoporous NiO with a bimodal pore size distribution and application in electrochemical capacitors. *Electrochim. Acta* **2010**, *55* (22), 6830-6835.
290. Masarapu, C.; Zeng, H. F.; Hung, K. H.; Wei, B., Effect of temperature on the capacitance of carbon nanotube supercapacitors. *ACS nano* **2009**, *3* (8), 2199-2206.
291. Choi, J. W.; McDonough, J.; Jeong, S.; Yoo, J. S.; Chan, C. K.; Cui, Y., Stepwise nanopore evolution in one-dimensional nanostructures. *Nano letters* **2010**, *10* (4), 1409-1413.
292. Chen, Z.; Augustyn, V.; Wen, J.; Zhang, Y.; Shen, M.; Dunn, B.; Lu, Y., High-performance supercapacitors based on intertwined CNT/V₂O₅ nanowire nanocomposites. *Adv Mater* **2011**, *23* (6), 791-795.
293. Cao, C.-Y.; Guo, W.; Cui, Z.-M.; Song, W.-G.; Cai, W., Microwave-assisted gas/liquid interfacial synthesis of flowerlike NiO hollow nanosphere precursors and their application as supercapacitor electrodes. *J. Mater. Chem.* **2011**, *21* (9), 3204-3209.

294. Jiang, H.; Li, C.; Sun, T.; Ma, J., High-performance supercapacitor material based on Ni(OH)₂ nanowire-MnO₂ nanoflakes core-shell nanostructures. *Chem comm* **2012**, *48* (20), 2606-2608.
295. Nunes, W. G.; Freitas, B. G.; Beraldo, R. M.; Filho, R. M.; Da Silva, L. M.; Zanin, H., A rational experimental approach to identify correctly the working voltage window of aqueous-based supercapacitors. *Sci. Rep.* **2020**, *10* (1), 19195.
296. Zhou, C.; Zhang, Y.; Li, Y.; Liu, J., Construction of high-capacitance 3D CoO@ polypyrrole nanowire array electrode for aqueous asymmetric supercapacitor. *Nano letters* **2013**, *13* (5), 2078-2085.
297. Zhu, H.; Wang, X.; Yang, F.; Yang, X., Promising carbons for supercapacitors derived from fungi. *Adv Mater* **2011**, *23* (24), 2745-2748.
298. Yan, J.; Fan, Z.; Sun, W.; Ning, G.; Wei, T.; Zhang, Q.; Zhang, R.; Zhi, L.; Wei, F., Advanced asymmetric supercapacitors based on Ni(OH)₂/graphene and porous graphene electrodes with high energy density. *Adv. Funct. Mater.* **2012**, *22* (12), 2632-2641.
299. Li, H.; Yu, M.; Wang, F.; Liu, P.; Liang, Y.; Xiao, J.; Wang, C.; Tong, Y.; Yang, G., Amorphous nickel hydroxide nanospheres with ultrahigh capacitance and energy density as electrochemical pseudocapacitor materials. *Nat. Commun* **2013**, *4* (1), 1894.
300. Li, M.; Sun, G.; Yin, P.; Ruan, C.; Ai, K., Controlling the formation of rodlike V₂O₅ nanocrystals on reduced graphene oxide for high-performance supercapacitors. *ACS Appl Mater Interfaces* **2013**, *5* (21), 11462-11470.
301. Park, S.; Ruoff, R. S., Chemical methods for the production of graphenes. *Nat. Nanotechnol.* **2009**, *4* (4), 217-224.
302. Fan, Z.; Yan, J.; Wei, T.; Zhi, L.; Ning, G.; Li, T.; Wei, F., Asymmetric supercapacitors based on graphene/MnO₂ and activated carbon nanofiber electrodes with high power and energy density. *Adv. Funct. Mater.* **2011**, *21* (12), 2366-2375.
303. Pan, A.; Zhang, J.-G.; Nie, Z.; Cao, G.; Arey, B. W.; Li, G.; Liang, S.-q.; Liu, J., Facile synthesized nanorod structured vanadium pentoxide for high-rate lithium batteries. *J. Mater. Chem.* **2010**, *20* (41), 9193-9199.

